A Measurement of the $\mathbf{W^+W^-}$ Production Cross Section in $\mathbf{p\bar{p}}$ Collisions at $\sqrt{\mathrm{s}} = 1.96$ TeV in the Dilepton Channel and Limits on Anomalous WWZ/γ Couplings.

Dustin McGivern

University College London

Submitted to the University of London in fulfilment of the requirements for the award of the degree of Doctor of Philosophy.

Abstract

Measurements of the production cross section of W^+W^- pairs in $\mathrm{p\bar{p}}$ collisions at 1.96 TeV and limits on trilinear gauge boson coupling (TGC) parameters are presented. The data were recorded with the CDF experiment at Tevatron during the 2001 and 2002 data taking periods in which a total integrated luminosity of 184 pb^{-1} was collected.

The data sample was filtered for events with two leptonic W boson decays where the charged leptons can be either electrons or muons. 17 events are observed against an expected background of $5.0^{+2.2}_{-0.8}$ events. The resulting cross-section is found to be $\sigma(\mathrm{p\bar{p}} \rightarrow \mathrm{W^+W^-}) = 14.5^{+5.8}_{-5.1}(\mathrm{stat})^{+1.8}_{-3.0}(\mathrm{syst}) \pm 0.9(\mathrm{lum})$ pb and agrees well with the Standard Model expectation.

Limits on the TGC parameters $\Delta\kappa$ and λ are set under both the equal coupling scheme, that assumes the W boson couples identically to the Z and γ, and the HISZ coupling scheme, that requires the couplings to respect $\mathrm{SU(2)_L \times U(1)_Y}$ gauge symmetry. In both cases this is achieved by using a likelihood fit to the lepton-P_T distribution of the 17 candidate events. The resulting limits are found to be:

$$-0.4 < \Delta\kappa < +0.6 \ (\lambda = 0); \quad -0.3 < \lambda < +0.4 \ (\Delta\kappa = 0)$$

for the EQUAL couplings and

$$-0.7 < \Delta\kappa < +0.9 \ (\lambda = 0); \quad -0.4 < \lambda < +0.4 \ (\Delta\kappa = 0)$$

for the HISZ couplings.

Acknowledgements

I would like to thank everyone that helped me in the course of my PhD. Particularly my supervisor, David Waters, without whom this thesis would simply not exist. Thanks also go to the rest of the diboson group at CDF: Susana Cabrera, Yimei Huang, Mark Kruse, Sunny Chuang, Sebastian Carron, Al Goshaw, Beate Heineman, Mike Kirby, Naho Tanimoto and Helen Hayward for their contributions, suggestions and all the things they taught me about CDF and particle physics. Thanks to Rob Snihur and Pasha Murat for all their help with the offline calibrations. Thanks also to Farrukh for being a friend when I first arrived in fermiland.

Thanks to Cheryl for her constant love, support and understanding. Even through all the missed phone calls and my complaints about writing-up, you've been absolutely amazing. Thanks also to my family for all their love and support over the years. I couldn't have got anywhere without you, thank you. I love you all loads.

A big thanks goes to all other grad students at Fermilab for being about the best group of friends I could have wished for. Thanks to "Sensible" Simon Waschke for never letting me forget the whole world of fun that exists outside of physics, thanks to Tamsin for organising all those nights out and being such a great friend; if I could adopt a sister it would be you. Thanks to Martin G for all the music and gigs. Thanks to Aidan and Helen, I never would have made it through the day without those tea breaks. Anant, my snowboarding buddy, thanks for all those times you drove to Devils Head and I had the extra hour in bed. Thanks to Martin T for making me laugh so hard I almost died on a daily basis and to D0Si for making up the other half of what has to be the best double act ever. Thanks to Chris for all those stories, it might take you forever to get a word out but its always worth the wait, thanks to Kyle for the Creme-Soda and video games and to Phil for driving a pick-up truck. Thanks to Emily for never pointing out how much sooner she finished her thesis than I finished mine. Thanks Lucio, Thilo, Nicola, Matt, Tats, Sinead, James, Paul, Marylin, Amber, Lydia and anyone I might have missed out, you made my time at Fermilab truly fantastic. I miss having all of you around and I love you all loads.

A massive thanks to the rest of the UCL HEP group; particularly Angela for all those conversations about politics and random bits of CDF code and Mark Lancaster for the threats and bribes to get me to actually finish this thesis.

I'd like to thank my old pals Yee, Nice John and Leo for being such fantastic mates during my PhD and to wish Wisdom and Umer good luck in writing up. I can't believe I'm going to have to call you lot Doctors!

A few other people deserve a mention: PPARC for the funding to do the PhD in the first place, mdixon for trying to keep me up to date with a dazzling array of physics results, those emails were a daily delight and all the staff at Seine Coffee on Clark Street for my morning *latte*, with an extra shot, without which I almost certainly would not have survived the I-90 every day for two years.

Finally, thanks to Chicago for all the sun, fun and snow and to London and UCL for being simply the best place in the whole universe.

Contents

List of Figures

List of Tables

Chapter 1

The Standard Model of Particle Physics

The Standard Model (SM) of particle physics provides a description of the structure and interactions of matter at the smallest scales that have so far been explored. It is a combination of theoretical constructs and experimentally measured quantities that taken together provide a description of the particles that comprise all known matter and the forces through which they interact. The following chapter provides an outline of this model and its workings.

It should be noted that the SM is not accepted as an accurate description of how the universe operates at its most fundamental level; it represents only our best current knowledge. Whilst this may be as good as is ever needed for all practical purposes, it is in many ways theoretically unsatisfactory. Its most notable absentee is gravity, assumed to be so weak that it is negligible at presently accessible experimental energies. Moreover, the organised table of properties of the 12 different fundamental particles (three families of quarks and leptons) hints at some sub-structure in much the same way that the periodic table hinted at atomic sub-structure.

1.1 The Fundamental Particles

The particle constituents of the Standard Model are classified as belonging to different groups depending on their properties. The first and most physically distinct classification, is that of matter particles and force particles. The matter particles are all spin-half and are therefore fermions and can be further separated into two groups: the leptons and the quarks. The force particles are all spin 1 particles and are therefore bosons.

1.1.1 The Leptons

The leptons can, yet again, be further sub-divided into three generations. Each generation differing from the last by an increased particle mass with all nearly all other properties remaining the same. Their properties are summarised in Table 1.1.

	particle	spin	Q(e)	Mass (MeV/c^2)	Anti-Particle
1st generation	e^-	1/2	-1	0.510998901 $\pm$ 0.000000044	e^+
	$\bar{\nu}_e$	1/2	0	< 0.003	ν_e
2nd generation	μ^-	1/2	-1	105.6583692 $\pm$ 0.0000094	μ^+
	$\bar{\nu}_\mu$	1/2	0	< 0.19	ν_μ
3rd generation	τ^-	1/2	-1	1776.99$\pm$0.29	τ^+
	$\bar{\nu}_\tau$	1/2	0	< 18.2	ν_τ

Table 1.1: Properties of the leptons

One property of great interest in recent times is the mass of the neutrinos. Originally formulated as massless particles within the Standard Model to account for their apparent single helicity state, recent evidence of neutrino oscillations [1] indicates this is a flawed assumption. The oscillation of a neutrino from one weak eigenstate into another, from electron neutrino into tau neutrino for example, requires the presence of a different, and therefore non-zero, mass for each of those eigenstates.

1.1.2 The Quarks

The quarks are organised in a similar way, six particles in three generations. Their masses and other properties are summarised in Table 1.2.

	particle	spin	Q(e)	Mass (MeV/c^2)	AP
1st generation	u	1/2	+2/3	1.5 - 4.0	$\bar{u}$
	d	1/2	-1/3	4 - 8	$\bar{d}$
2nd generation	c	1/2	+2/3	1150 - 1350	$\bar{c}$
	s	1/2	-1/3	80 - 130	$\bar{s}$
3rd generation	t	1/2	+2/3	174300±5100	$\bar{t}$
	b	1/2	-1/3	4100 - 4400	$\bar{b}$

Table 1.2: Properties of the quarks

1.1.3 The Bosons

The forces between the matter particles of the Standard Model are described in terms of the exchange of a boson. Particles with non-zero electric charge will interact with each other by exchanging a photon, the boson associated with the electromagnetic force. Particles that possess a non-zero weak-isospin are able to interact through the weak nuclear force by exchanging either a W^+, W^- or a Z^0 boson and particles that possess a color charge will interact through the strong nuclear force by exchanging one of the 8 gluons. The properties of these exchange bosons are detailed in full in Table 1.3. One of the central features of the Standard Model description of the weak bosons is their ability to interact with themselves. Since the W^+ and W^- themselves carry weak-isospin they are able to interact with each other and with the Z^0 (the Z^0 has zero weak-isospin so it cannot couple to itself, neither can the γ). This self coupling, a result of a non-abelian gauge symmetry, is one of the theoretical features of the Standard Model that is explored experimentally in this thesis.

Boson	Force	Spin	Q(e)	Mass (GeV/c^2)	Range(fm)
γ	Electromagnetic	1	0	$< 6 \times 10^{-23}$	∞
W	Charged Weak	1	± 1	80.425 ± 0.038	$\approx 10^{-3}$
Z	Neutral Weak	1	0	91.1876 ± 0.0021	$\approx 10^{-3}$
g	Strong	1	0	0	< 1
Graviton	Gravity	2	0	0	∞

Table 1.3: Properties of the bosons

1.2 The Fundamental Forces

Electroweak Theory

The quantum theory of the electromagnetic force is known as Quantum Electrodynamics (QED). In QED, the electromagnetic force is governed by a $U_Q(1)$ gauge symmetry such that all interactions are based upon the exchange of a photon(γ) and always conserve electric charge, Q. Similarly the weak nuclear force is described through the exchange of a weak boson between left-handed particles and conserves weak isospin, T.

Glashow, Weinberg and Salam [2] showed that the electromagnetic and weak nuclear interactions can be described by a single unified quantum field theory based on a gauge group $\mathrm{SU_L(2)} \times \mathrm{U_Y(1)}$ symmetry, where L represents the left-handed weak isospin and Y represents hypercharge. This single unified description is called the electroweak theory. After this unification the U(1) generator is modified to account for right-handed interactions by replacing Q with hypercharge, Y, defined through

$$Q = T_3 + \frac{Y}{2}$$

where T_3 is the third component of the weak isospin. The result is a theory that is then based upon the exchange of electroweak bosons (γ, W and Z) such that both weak isospin and hypercharge are always conserved.

At this point, despite the aesthetic qualities of the theory, reality causes problems. The resulting weak bosons (W and Z) do not quite connect with experimental results. The W and Z have both been measured to be very massive particles, but including terms in the Lagrangian to describe these masses destroys the $\mathrm{SU_L}(2) \times \mathrm{U_Y}(1)$ symmetry of the theory. The most accepted solution to this problem is known as the Higgs mechanism. The Higgs mechanism introduces an additional term into the Lagrangian that represents two scalar fields along with an associated potential energy and then rearranges the Lagrangian such that the $\mathrm{SU_L}(2) \times \mathrm{U_Y}(1)$ symmetry is broken, or hidden. That which is left behind is a Lagrangian describing the electroweak interaction in terms of three massive weak bosons ($\mathrm{W}^{\pm}$ and Z^0) and a massless photon (γ) plus an additional spin zero particle known as the Higgs Boson. The theory gives no accurate prediction for the mass of this Higgs boson itself and it has to date avoided experimental detection.

Quantum Chromodynamics

The strong nuclear force is described by Quantum Chromodynamics, again a quantum field theory, but this time based upon the gauge group $\mathrm{SU_c}(3)$. The interactions take place through the exchange of a gluon such that color charge is always conserved. Whilst all of the forces have coupling constants that run with energy, non-abelian forces such as the weak and strong force, have a coupling constant that decreases with energy. In the case of the strong force this means that at large momentum transfers or very small distances the quarks can be considered to be free, a phenomena known as asymptotic freedom. As the separation between quarks grows, the strength of the force increases until it becomes energetically more favourable for the potential energy in the color field to convert into quark-antiquark pairs. This gives rise to the property of quark confinement that restricts quarks to bound states of pairs and triplets.

The Standard Model

Taking the $\mathrm{SU_L}(2) \times \mathrm{U_Y}(1)$ electroweak theory and combining it with the $\mathrm{SU_c}(3)$ gauge group of QCD provides a description of all interactions of all known particles. This is referred to as the Standard Model of particle physics.

Chapter 2

WW Production And Trilinear Gauge Boson Couplings

Measurements of many particle interactions allow for a test of the Standard Model description of the interaction of vector bosons with the fermions. WW production is one of the few that allows a test of the SM description of the interactions of the bosons with themselves (known as Trilinear Gauge Boson Couplings or TGCs), and as such, measurements of this process represent a vital test of the Standard Model's ability to accurately describe nature. In this chapter a discussion of the theoretical description of TGCs, both in the Standard Model and beyond, and WW production at the Tevatron, is given.

2.1 TGCs In And Beyond The Standard Model

The electroweak Standard Model contains only two possibilities for the direct interactions of the three electroweak gauge bosons: a W^+ and a W^- coupling to a Z^0, and a coupling to a γ. These are shown in Figure 2.1.

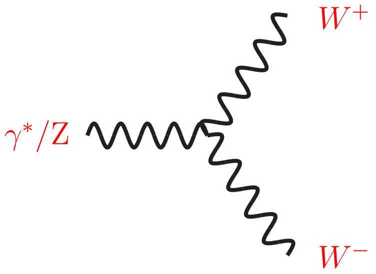

Figure 2.1: Electroweak trilinear gauge boson couplings

Within the Standard Model there are also interactions involving four bosons ($W^+W^-W^+W^-$, $W^+W^-Z^0Z^0$, $W^+W^-\gamma\gamma$ and $W^+W^-Z^0\gamma$) known as quartic couplings and also many different combinations of gluon interactions in the QCD sector, but only electroweak TGCs will be discussed in this thesis.

2.1.1 Anomalous Couplings And The Generalised Lagrangian

As mentioned earlier, one of the reasons WW production is so important is that it allows a test of the Standard Model description of the TGCs by searching for any deviation in the coupling values from the Standard Model prediction, i.e. an anomalous coupling. For example, a composite Z or W would mean that at the energy scale at which the composites becomes visible, the simple TGCs of the Standard Model would need to be replaced by couplings to the constituent particles. Alternatively a new heavy Z like boson would mean an additional diagram in the s-channel contribution of the WW cross-section which might disrupt the delicate gauge cancellation of the Standard Model (discussed later in section 2.2.1).

A generalised Lagrangian is required in order to identify such deviations without forming and testing every single imaginable new model. The generalised Lagrangian simply parameterises any such deviation to allow predictions for what effect any kind of non-SM TGC would have on the kinematics of WW events and to what extent it will alter the cross-section, without requiring any knowledge of the underlying theory.

The most general effective Lagrangian describing the WWV coupling (V $= \gamma$ or Z) is as follows [3]:

$$\begin{aligned} L_{WWV}/g_{WWV} &= i\boldsymbol{g}_1^V(W^\dagger_{\mu\nu}W^\mu V^\nu - W^\dagger_\mu V_\nu W^{\mu\nu}) \\ &+i\boldsymbol{\kappa_V}W^\dagger_\mu W_\nu V^{\mu\nu} \\ &+\frac{i\boldsymbol{\lambda_V}}{M_W^2}W^\dagger_{\lambda\mu}W^\mu_\nu V^{\nu\mu} \\ &-\boldsymbol{g_4^V}W^\dagger_\mu W_\nu(\partial^\mu V^\nu + \partial^\nu V^\mu) \\ &+\boldsymbol{g_5^V}\epsilon^{\mu\nu\rho\sigma}(W^\dagger_\mu \overleftrightarrow{\partial_\rho} W_\nu)V_\sigma \\ &+i\tilde{\boldsymbol{\kappa}}_{\boldsymbol{V}}W^\dagger_\mu W_\nu \tilde{V}^{\mu\nu} \\ &+\frac{i\tilde{\boldsymbol{\lambda}}_{\boldsymbol{V}}}{M_W^2}W^\dagger_{\lambda\mu}W^\mu_\nu \tilde{V}^{\nu\lambda} \end{aligned} \tag{2.1}$$

Where W^μ denotes the W^- field, V the Z^0/γ fields and

$$\begin{aligned} W_{\mu\nu} &= \partial_\mu W_\nu - \partial_\nu W_\mu \\ V_{\mu\nu} &= \partial_\mu V_\nu - \partial_\nu V_\mu \\ \tilde{V}^{\mu\nu} &= \frac{1}{2}\epsilon_{\mu\nu\rho\sigma}V^{\rho\sigma} \\ (A\overleftrightarrow{\partial_\mu}B) &= A(\partial_\mu B) - (\partial_\mu A)B \end{aligned}$$

The coupling constants describing the strength of the WWV coupling, g_{WWV}, are

$$g_{WWZ} = -e\ cot(\theta_W), \quad g_{WW\gamma} = -e$$

Where θ_W is the weak mixing angle and e the elementary "charge" of the electron. The parameterisation of any deviation from the Standard Model is achieved by the inclusion of the individual coupling constants for each term; the symbols in bold in Equation 2.1. Many of these coupling constants can be directly related to physical properties of the bosons, for example g_1^γ determines the charge of the W^+, C_W, in units of the positron charge:

$$C_W = cg_1^\gamma. \tag{2.2}$$

κ_γ and λ_γ are related to the magnetic dipole moment of the W^+ by

$$\mu_W = \frac{e}{2M_W}(1 + \kappa_\gamma + \lambda_\gamma), \tag{2.3}$$

and the electric quadrupole moment as

$$Q_W = \frac{-e}{M_W}(\kappa_\gamma - \lambda_\gamma). \tag{2.4}$$

Also, $\tilde{\kappa}_\gamma$ and $\tilde{\lambda}_\gamma$ are related to the electric dipole moment d_W by

$$d_W = \frac{e}{2M_W}(\tilde{\kappa}_\gamma + \tilde{\lambda}_\gamma) \tag{2.5}$$

and the magnetic quadrupole moment $\tilde{Q}_W$ as

$$\tilde{Q}_W = \frac{-e}{M_W}(\tilde{\kappa}_\gamma - \tilde{\lambda}_\gamma) \tag{2.6}$$

The Standard Model Lagrangian, shown in Equation 2.7, is recovered from this generalised description by setting κ_γ, κ_Z, g_1^γ and g_1^Z to 1 and all others to 0:

$$L_{WWV}/ig_{WWV} = (W^\dagger_{\mu\nu}W^\mu V^\nu - W^\dagger_\mu V_\nu W^{\mu\nu}) + W^\dagger_\mu W_\nu V^{\mu\nu}. \tag{2.7}$$

2.1.2 Refining The Search For Anomalous Couplings

Investigating all possible deviations as described by the generalised Lagrangian means testing a very large parameter space. It is usual in these studies to make simplifying assumptions to restrict the number of free parameters. Dismissing the terms that violate C, P and CP conservation (see Table 2.1) leaves a Lagrangian that is much more restricted, and more realistic, but still more general than the Standard Model. In addition, respecting electromagnetic gauge invariance requires that $g_1^\gamma = 1$, leaving just five free parameters: κ_γ , κ_Z , and g_1^Z, λ_γ and λ_Z which are typically reported in terms of their deviations from their Standard Model values: $\Delta\kappa_\gamma = \kappa_\gamma - 1$, $\Delta\kappa_Z = \kappa_Z - 1$, $\Delta g_1^Z = g_1^Z - 1$, λ_γ and λ_Z.

coupling	SM value	C-conserving	P-conserving	CP-conserving
$g_1^\gamma\ g_1^Z$	1	$\surd$	$\surd$	$\surd$
$\kappa_\gamma\ \kappa_Z$	1	$\surd$	$\surd$	$\surd$
$\lambda_\gamma\ \lambda_Z$	0	$\surd$	$\surd$	$\surd$
$g_4^\gamma\ g_4^Z$	0	$\times$	$\surd$	$\times$
$g_5^\gamma\ g_5^Z$	0	$\times$	$\times$	$\surd$
$\tilde{\kappa}_\gamma\ \tilde{\kappa}_Z$	0	$\surd$	$\times$	$\times$
$\tilde{\lambda}_\gamma\ \tilde{\lambda}_Z$	0	$\surd$	$\times$	$\times$

Table 2.1: Symmetry properties of the couplings

To further simplify matters, additional assumptions can be made to reduce the number of free parameters. Two schemes are commonly used for this purpose;

the Equal Couplings Scheme and the HISZ [4] coupling scheme (named after its authors). The Equal couplings scheme assumes that the Z and the γ both couple identically to the W giving:

$$\begin{aligned} \Delta g_1^Z &= 0.0 && (2.8) \\ \Delta\kappa^Z &= \Delta\kappa_\gamma && (2.9) \\ \lambda_Z &= \lambda_\gamma && (2.10) \end{aligned}$$

In the HISZ scheme, the couplings are required to respect $SU(2)\times U(1)$ symmetry, thereby giving the relationships:

$$\begin{aligned} \Delta g_1^Z &= \frac{1}{2\cos^2\theta_W}\Delta\kappa_\gamma && (2.11) \\ \Delta\kappa^Z &= \frac{1}{2}(1-\tan^2\theta_w)\Delta\kappa_\gamma && (2.12) \\ \lambda_Z &= \lambda_\gamma && (2.13) \end{aligned}$$

In practice these coupling parameters depend upon the energy scale of the interaction. It has been shown [3] that the λ and κ dependent parts of the helicity amplitude rise with $\hat{s}/M_W^2$ (the Δg dependent parts rise only with $\sqrt{\hat{s}}/M_W$) and if left unchecked will violate tree-level unitarity. This behaviour must be controlled somehow if the couplings are to have any sensible meaning. A consistent picture of WW production including anomalous couplings, requires therefore, that these constants are in fact form factors that vanish in the $\hat{s}\to\infty$ limit. They might, for example take the form:

$$\lambda(\hat{s}) = \frac{\lambda}{(1+\hat{s}/\Lambda^2)^2}$$

Where Λ is some cut-off scale that controls the high-energy behaviour, i.e. it is the energy scale at which the new physics becomes important. Experimental limits on the coupling values are therefore often reported for a particular choice of Λ.

2.2 W Pair Production

From the two allowed TGCs in the Standard Model, it can be seen that the final states that result from any such interaction are limited to W^+W^-, $W^\pm Z^0$ and $W\gamma$. Although this thesis will only be concerned with the W^+W^- final state, the best understanding of TGCs will be obtained from the information extracted from all the final states.

Given the rarity of the 'massive' diboson channels, W^+W^-, Z^0Z^0 and $W^\pm Z^0$ they are an excellent place to look for any non-Standard Model contribution to the TGCs, since even the smallest deviations in the TGCs will result in significantly altered cross-sections. Only WW is sensitive to deviations in both TGCs, though it should be noted that separating out the different contributions from the two TGCs is not easy.

A further reason that makes understanding W pair production so essential lies in its importance as a background to many other Standard Model measurements, for example $t\bar{t} \to l\bar{l}j\bar{j}$, and also searches beyond the Standard Model that result in similar final states. It will also be vital to understand the W pair signal if the Higgs boson is to be discovered in the higher mass region of $150 < M_H < 180$ where Higgs production is dominated by the diagram in Figure 2.2. In this region where the Higgs mass is above the W pair threshold and below the Z pair threshold then the branching ratio for $H \to WW$ is nearly 100% (see Reference [5] and Figure 2.3) but the Higgs signal will only be of the same size as Standard Model WW production and top pair production (see Figure 2.4).

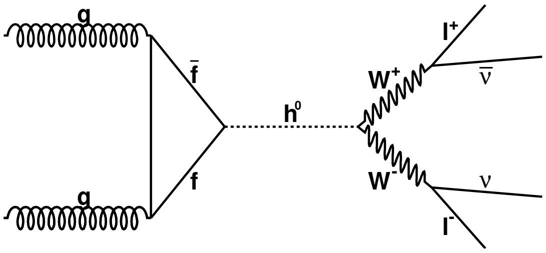

Figure 2.2: Leading order Higgs production from gluon fusion

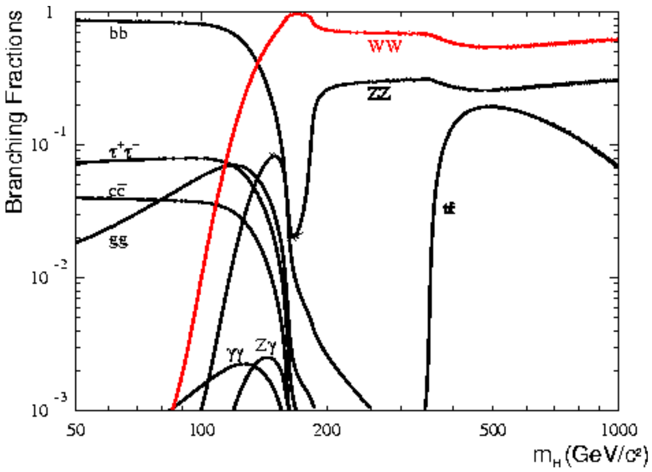

Figure 2.3: Higgs branching ratios as a function of Higgs mass

2.2.1 W Pairs At The Tevatron

The tree level WW production Feynman diagrams for the Tevatron are shown in Figure 2.5. The t and u-channel diagrams contribute around 90% of the leading order cross-section at the Tevatron and are fully described by the coupling of the quarks to the W boson, which are already well known. The s-channel diagram contributes the remaining 10% of the cross-section and is the only diagram which

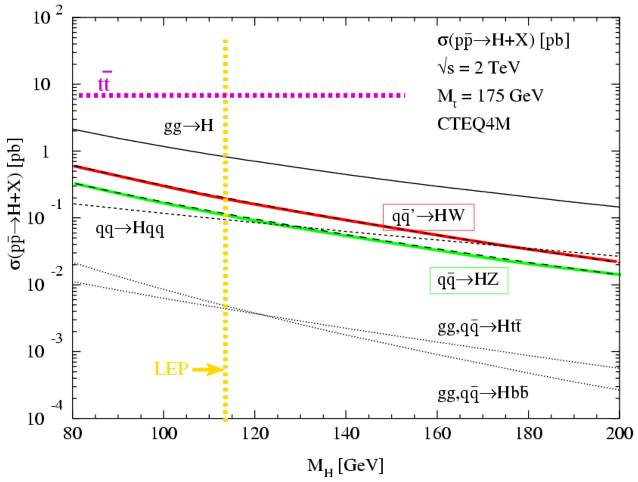

Figure 2.4: Higgs production cross-sections as a function of Higgs mass

involves TGCs. The presence of the s-channel diagram is vital, however, in maintaining partial wave unitarity. The cross-section of the t and u-channel diagrams is linear in $\hat{s}$ and so for sufficiently large energies would violate unitarity. Only when the cross-section is calculated in the presence of the s-channel diagram, with both TGCs included, does the squaring of the amplitude result in cross terms that restore unitarity. This is known as a "delicate" gauge cancellation and, as discussed earlier, has important consequences for any scenario that involves the presence of non-Standard Model TGCs.

However, cross-sections for W pair production at the Tevatron cannot be computed analytically from these diagrams due to the composite nature of the proton. Instead the cross-section from the parton subprocess is calculated and then summed over all possible participating partons and the parton momentum distribution by a Monte Carlo program. For the Monte Carlo program to complete such a calculation it requires a description of the momentum distribution of the partons inside the baryon. This is known as a Parton Distribution Function

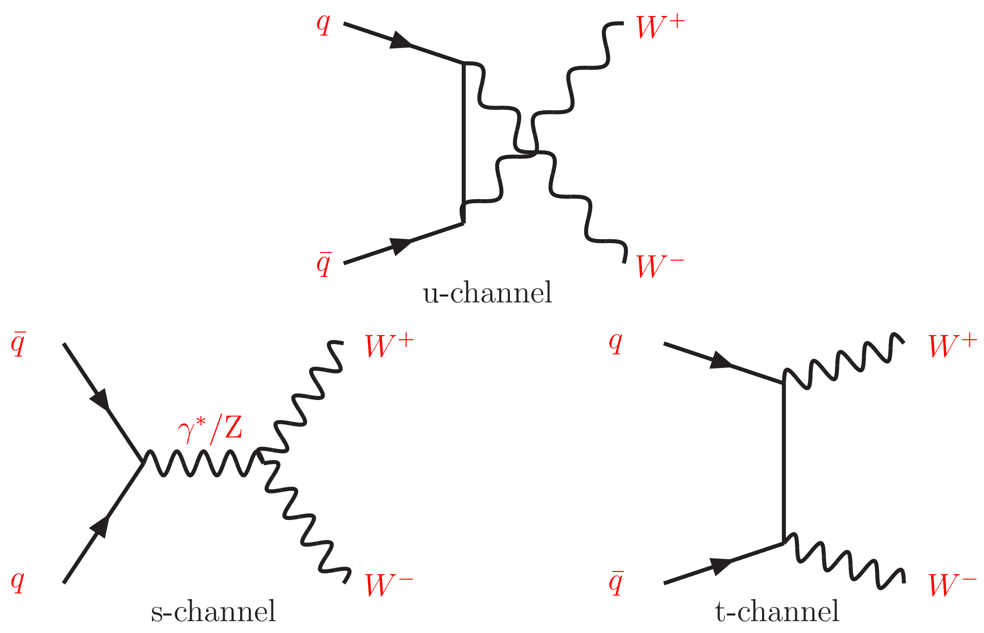

Figure 2.5: Tree-level WW production at the Tevatron

(PDF) and describes the probability that a particular parton within the baryon has fraction x of the total baryon momentum.

PYTHIA [6] and HERWIG [7] represent well established tree level, or leading order(LO), Monte Carlos that can provide such a calculation of the cross-section including a model of the outgoing parton showering and hadronisation. In addition, some new Monte Carlo generators, such as MCFM [8], can provide cross-section calculations at next-to-leading order accuracy.

MCFM: Monte Carlo for FeMtobarn processes

The MCFM program aims to give a unified description of all processes involving final states with heavy quarks, leptons and missing energy at next-to-leading-order QCD accuracy. There are three major contributions to each amplitude, the lowest order Born contributions (Figure 2.5), the virtual (loop) corrections and the real corrections associated with additional soft or collinear radiation, examples of which are shown in Figure 2.6. MCFM has an additional contribution from singly resonant diagrams that arise from the final state of four leptons that would be overlooked in a calculation with a final state of two bosons. The program includes the following processes:

- $p\bar{p} \rightarrow W/Z, W + Z, WW, ZZ, W/Z + H, H, W + g(\rightarrow b\bar{b})$
- $p\bar{p} \rightarrow W + 2jets, W/Z + 1jet, Z/\gamma + b\bar{b}, Z/\gamma + 2jets$

The lepton/hadronic decays of the bosons are included as sub-processes with the full spin correlations for the bosons and the full width of the W bosons. Many of the NLO matrix elements are obtained from calculations of the $e^+e^- \rightarrow 4$ jets process.

Theoretical Cross-Sections

The MCFM prediction for the total WW production cross-section at $\sqrt{s} = 2$ TeV is 12.4 ± 0.8 pb using the CTEQ6 LHAPDF [10]. The error on this cross-section value is discussed in section 7.4.3

2.2.2 Experimental Considerations

W pair events must be identified by reconstructing the decay products of the two W's, i.e. experimental signatures associated with the high-P_T charged leptons, neutrinos and jets (from hadronic decays to quarks). W pair decays can therefore be put into three "channels" depending on the topology of the final state; the leptonic channel ($WW \rightarrow l\bar{\nu}\bar{l}\nu$), the semi-leptonic channel ($WW \rightarrow q\bar{q}l\nu$) and the hadronic channel ($WW \rightarrow q\bar{q}q\bar{q}$). The cross-section for the three channels differs due to the branching ratios of the W decays to leptons and quarks and is

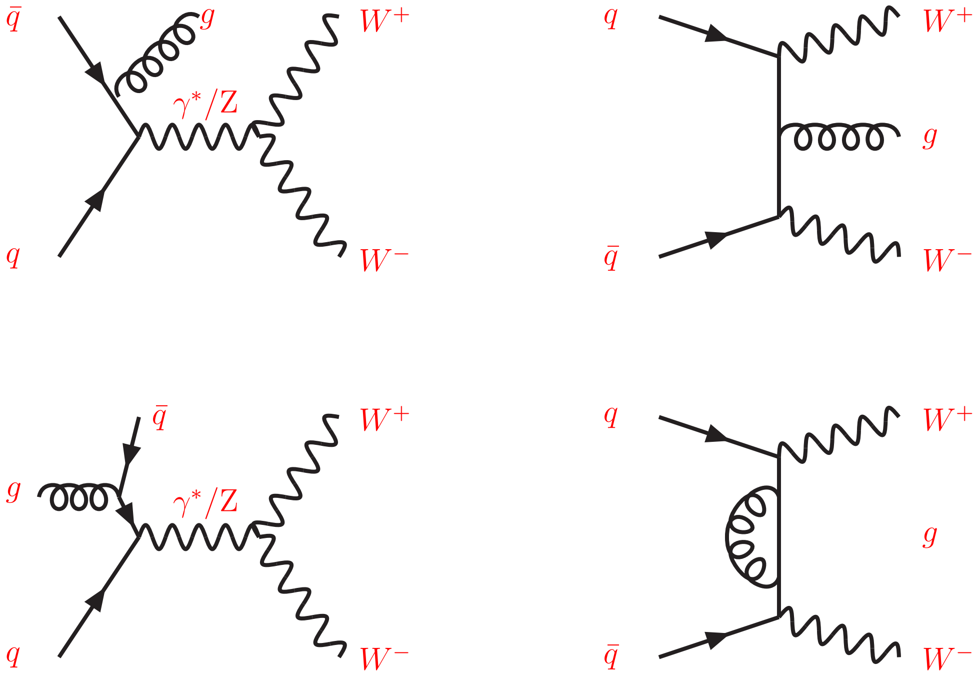

Figure 2.6: Examples of the 36 NLO WW production diagrams at the Tevatron.

shown in Table 2.2. The hadronic channel has the advantage of being the only one with fully measured kinematics since neutrinos aren't measured. However it is difficult to match the jets to the W's and the backgrounds are huge (QCD multijet production has a much higher cross-section). The semi-leptonic channel has one significant advantage in allowing each W to be identified unambiguously but again suffers from very large backgrounds ($\sigma(W \to e\nu + \geq 1\text{jet}) \approx 500$ pb), also making it less suitable for a cross-section measurement. This leaves only the purely leptonic channel which, though suffering from poorly known kinematics due to the presence of two neutrinos, offers a very clean and distinctive WW signal with comparatively low backgrounds. For this reason the leptonic channel is chosen for the measurements in this thesis.

Channel	Relative Cross-Section
$qqqq$	47%
$ql\nu$	42%
$l = e, \mu$	30%
$l\bar{\nu}\bar{l}\nu$	11%
$l = e, \mu$	5%

Table 2.2: Portion of Total WW Cross-Section in each decay channel.

2.3 Current Knowledge

The following sections outline the current best limits on the anomalous couplings derived from theory and the best measurements of the cross-section of $WW \rightarrow l\bar{\nu}\bar{l}\nu$ and associated limits on anomalous couplings from experimental data.

2.3.1 Theoretical Limits: Λ And Unitarity

A result of the form factor dependence of the anomalous couplings is that for a given choice of Λ, a low-energy limit on the anomalous couplings is required to ensure tree-level unitarity is satisfied [11]. This limit on the possible values of the anomalous couplings as a function of Λ is given by the expression [12]

$$\Lambda \leq \left[\frac{6.88}{(\kappa - 1)^2 + 2\lambda^2}\right]^{\frac{1}{4}}$$

And the resulting limits for some likely choices of Λ are shown in Figure 2.7. Care must be taken when choosing the value of Λ to be used in comparisons with data to ensure that these unitarity limits are weaker than the expected experimental limits.

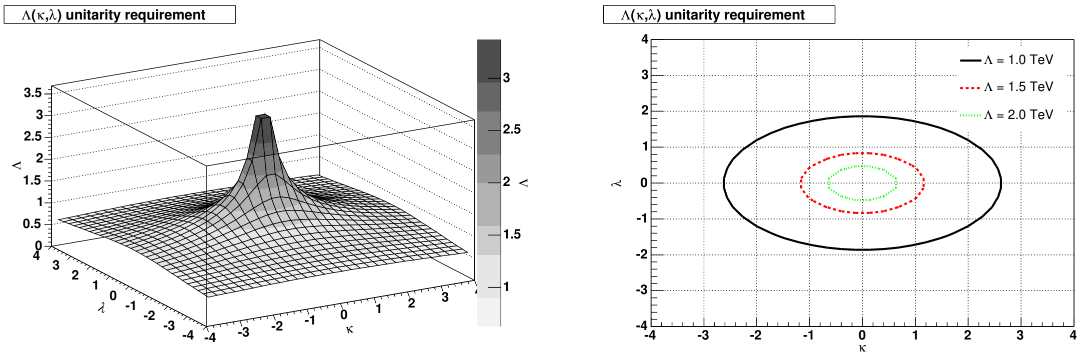

Figure 2.7: Tree-level unitarity limits on anomalous couplings due to choice of Λ. For a given choice of Λ the area outside of the curve is excluded to ensure unitarity is respected.

2.3.2 DØ Measurements

DØ has searched for several diboson final states in a variety of decay channels.

Run 1

In 97pb^{-1} of Run I data [13], 5 candidate events for $WW \rightarrow l\bar{l}\nu\bar{\nu}$ were found against an expected background of 3.1 ± 0.4 events and an expected signal of 1.9 ± 0.1 events. This results in an upper limit on the WW production cross-section of 37.1 pb. The resulting anomalous coupling limits with $\Lambda = 1.5$ TeV and the Equal couplings Scheme were: $-0.62 < \Delta\kappa < 0.77$ $(\lambda = 0)$ and $-0.53 < \lambda < 0.56$ $(\Delta\kappa = 0)$.

DØ also reported 1D coupling limits [14] from $W\gamma$ production in Run 1 data using a binned maximum likelihood fit to the E_T^γ spectrum. The published limits were $-0.93 < \Delta\kappa_\gamma < 0.94$ and $-0.31 < \lambda_\gamma < 0.29$ at the 95% confidence level, assuming $\Lambda = 1.5$ TeV.

Run 2

Preliminary results from DØ Run 2 data have recently been published [15]. In 224-252 pb^{-1} of data[1] 25 candidates for $WW \rightarrow l\bar{l}\nu\bar{\nu}$ were found against an expected background of 8.1 ± 1.7 events. A measured cross-section of $\sigma(p\bar{p} \rightarrow W^+W^-) = 13.8^{+4.3}_{-3.8}(stat)^{+1.2}_{-0.9}(syst) \pm 0.9(lum)$ was obtained, corresponding to a 5.2 standard deviation observation.

2.3.3 CDF Measurements

$WW \rightarrow l\bar{l}\nu\bar{\nu}$

CDF also found 5 events in $108 pb^{-1}$ of Run I data [16] consistent with $WW \rightarrow l\bar{l}\nu\bar{\nu}$, against an expected background of 1.2 ± 0.3 events. The measured cross-section was found to be $\sigma(p\bar{p} \rightarrow W^+W^-) = 10.2^{+6.3}_{-5.1}(stat) \pm 1.6(syst)$ pb. Using these 5 events with $\Lambda = 2.0$ TeV and equal couplings the 95%CL limits on the anomalous couplings were $-1.1 < \Delta\kappa < 1.3$ $(\lambda = 0)$ and $-0.9 < \lambda < 0.9$ $(\Delta\kappa = 0)$.

$W\gamma$ Anomalous Coupling Limits

CDF also reported anomalous coupling limits from the E_T^γ spectrum in $W\gamma$ events [17] with values of $-1.8 < \Delta\kappa < 2.0$ and $-0.7 < \lambda < 0.6$.

2.3.4 LEP 2 Measurements

The most recent LEP2 results [18] are shown in Table 2.3. The limits are extracted from a fit to the total W pair production cross-section plus additional fits to the angular distributions of the W bosons and their decay products. Direct

[1] depending on lepton category

comparisons between LEP and the Tevatron are difficult since the Tevatron limits correspond to a higher $\sqrt{s}$ than the LEP2 limits. The LEP experiments also have no need to use a form factor dependence in their couplings. Another important difference is that the Tevatron has the ability to probe the TGCs using $W\gamma$ final state in addition to W pair production, giving the possibility of separating out the contributions from the $WW\gamma$ and the WWZ vertices experimentally. Even though Tevatron and LEP2 limits are therefore largely complimentary rather than directly competitive, it is clear that it will be challenging for the Tevatron to reach the same sensitivity as LEP2.

$-0.105 < \Delta\kappa_\gamma < 0.069$
$-0.059 < \lambda_\gamma < 0.026$
$-0.051 < \Delta g_1^Z < 0.034$

Table 2.3: LEP2 anomalous coupling limits

Chapter 3

The CDF Detector at the Tevatron

The data used in this analysis was collected by the Collider Detector at Fermilab (CDF) which is a generic multi-purpose particle detector situated at the Fermi National Accelerator Laboratory (Fermilab) collecting data from proton anti-proton collisions produced by the Tevatron particle accelerator.

3.1 The Tevatron

The Tevatron is the highest energy particle collider so far constructed anywhere in the world, bringing together beams of protons and anti-protons in collisions where the total center of mass energy is 1.96 TeV.

3.1.1 The Tevatron Accelerator Chain

The Tevatron itself is actually the last step in a long sequence of machines (see Figure 3.1) that firstly produce both the protons and the antiprotons and then

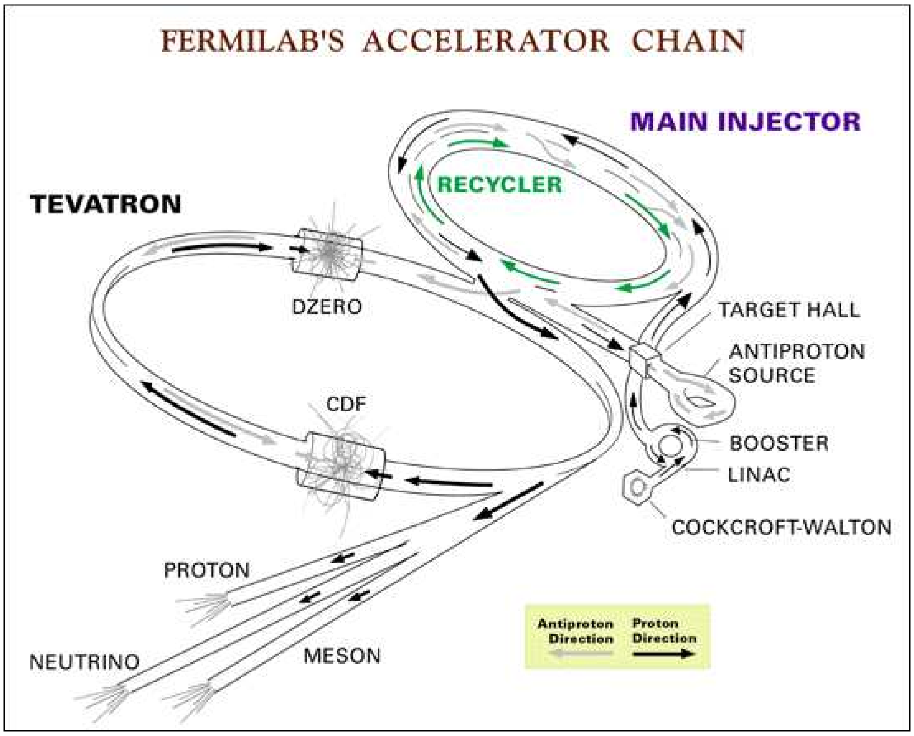

Figure 3.1: The Fermilab accelerator chain

accelerate them up to the required energies.

Producing protons

The production of the proton beam begins by producing H^- ions by ionising hydrogen gas in the presence of a caesium surface inside a Cockroft-Walton pre-accelerator.

The Cockroft-Walton accelerator takes the H^- ions to 750 keV and then feeds them into the LINAC. The LINAC is 150 m long, and consists of a line of Radio-Frequency electric field cavities that accelerate the H^- ions in steps. The ions are shielded from the reversed electric fields that exist between the accelerating sections to prevent them from begin decelerated. By the end of the LINAC the ions have reached an energy of 400 MeV, at which point they are passed through a carbon filter that strips off the two electrons to leave a pure proton beam. This proton beam then enters the BOOSTER, a 75 m radius proton synchrotron that is located 6m below the surface. The protons are circulated around the BOOSTER until they reach 8 GeV, at which point they are collected into bunches. Some of these bunches will be used in the Tevatron and others for the production of anti-protons.

Producing anti-protons

From the BOOSTER the bunches are transfered into the MAIN INJECTOR, a 3 km circumference synchrotron that accelerates the protons up to 150 GeV. From here some bunches are then passed directly into the Tevatron ready for collisions and other bunches are selected and diverted into a nickel target. The various products of this collision, which include anti-protons, are focused into a beam by a cylindrical lithium lens and an azimuthal magnetic field (generated by passing a pulsed current through the lens). This beam is then passed through a pulsed dipole magnet that acts as a charge-mass spectrometer, selecting out the anti-protons and directing them into the DEBUNCHER.

The DEBUNCHER is an accumulator ring that uses stochastic cooling to reduce the momentum spread of the anti-protons. This process also increases their spatial spread, producing a continuous beam of anti-protons which then have to be passed to the ACCUMULATOR where they are stacked back into bunches. These anti-proton bunches are then passed back into the MAIN INJECTOR and are accelerated up to 150 GeV before being fed, along with the protons, into the Tevatron.

Colliding matter and anti-matter

The Tevatron has a 1 km radius and sits 10 m below the surface. Its superconducting magnets bend the proton and anti-proton beams into intertwined helical orbits, with the protons travelling clock-wise and the anti-protons counterclock-wise.

Once 36 bunches of protons and 36 bunches of anti-protons have been loaded into the Tevatron, defined as a store, the two beams are accelerated up to an energy of 0.98 TeV. Once this energy has been obtained, the beams are brought into collision and focused into two interaction regions, referred to as B0 and D0, by a series of quadrupole magnets such that the bunches will collide once every 396 ns

There is much current work underway to commission the RECYCLER RING, which is housed inside the main injector tunnel. Originally designed to collect the unused anti-protons at the end of the store and then recycle them, it is now intended that it will be used instead to store new anti-protons to allow higher anti-proton intensities in each store. The ongoing electron cooling project will also be housed in the RECYCLER and will help to push the Tevatron performance higher by reducing the momentum spread of the $\bar{p}$ beam even further than is possible with the stochastic cooling system currently in place.

3.1.2 The Tevatron Performance

Luminosity

The performance of any accelerator is measured by its luminosity, a measure of the particle flux that the machine produces. For the case of a synchrotron the luminosity is approximated by

$$\mathcal{L} = \frac{N_p N_{\bar{p}} N_B f}{4\pi\sigma_{xy}} \tag{3.1}$$

where $N_p (N_{\bar{p}})$ is the number of protons (anti-protons) in each bunch, N_B is the number of bunches, f is the orbital frequency and σ_{xy} is the RMS size of the beam in the transverse plane at the interaction point. The conventional units are cm^{-2}s^{-1}. The integrated luminosity delivered by the machine (L) is measured by

$$L = \int \mathcal{L} dt$$

and the number of events of a particular type of interaction is given by

$$N = \sigma L$$

where σ is the cross-section of that process; a measure of how probable that process is.

However, the terms in Equation 3.1 cannot be measured with sufficient precision. Since the integrated luminosity is central in predicting the event yields used in analysis a more accurate method is required. This problem is solved by a specific detector built to monitor the Tevatron luminosity. The Cerenkov Luminosity Counter [19] (CLC) consists of two modules located in a small hole in the high η region of the forward calorimetry. Each module contains an array of 2 cm long counters filled with Isobutane gas. A fast photomultiplier tube is connected to the end of each counter to collect the Cerenkov light produced by charged particles irradiating the gas. The number of hits in the CLC is then used to calculate the luminosity with

$$\mathcal{L} = \frac{f_{BC} < N_H >_\alpha}{\sigma_{p\bar{p}} \epsilon_\alpha < N_H^1 >_\alpha}$$

where f_{BC} is the bunch crossing frequency, $\sigma_{p\bar{p}}$ is the inelastic $p\bar{p}$ cross section, ϵ_α is the CLC acceptance for selection criteria α, $< N_H >_\alpha$ is the number of hits in the CLC for the bunch crossing and $< N_H^1 >_\alpha$ is the number of hits in the CLC for one $p\bar{p}$ interaction.

Data Collected

The current data taking period of the Tevatron and its experiments is referred to as Run 2, which began taking data in earnest in late 2001. The operational parameters of the Tevatron during the data taking periods used in this analysis are summarised in Table 3.1. So far in Run 2 around 550 pb^{-1} of data has been collected by CDF. Projections of the Tevatron future performance are subject to constant revision as more progress is made with the various ongoing accelerator projects and upgrades, but current estimates are of around 6 ± 3 fb^{-1} by 2010.

Parameter	value
$\sqrt{s}$	1.96 TeV
N Bunches	36
Bunch spacing	396 ns
Average Luminosity	$3 \times 10^{31}\text{cm}^{-2}\text{s}^{-1}$
Highest Luminosity	$4.06 \times 10^{31}\text{cm}^{-2}\text{s}^{-1}$

Table 3.1: Tevatron operating parameters during March 2002 to September 2003 data taking.

Data used in this analysis

The data used in this analysis corresponds to the data collected during the 2002 and 2003 data taking periods (see Figure 3.2). This data corresponds to a luminosity of $L = 184$ pb^{-1}.

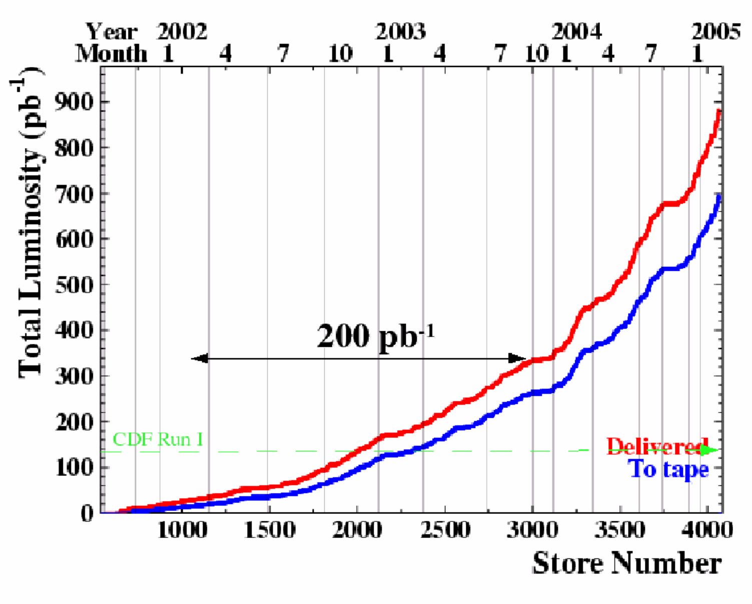

Figure 3.2: The CDF Run 2 dataset

3.2 CDF

CDF [20] is a multi-purpose particle detector. It has the typical layered, cylindrically symmetric design for a symmetric colliding beam accelerator, that attempts to completely surround the interaction point. Thereby allowing the study of a large variety of final states produced in $p\bar{p}$ collisions. The detector is shown schematically in Figure 3.3, and is comprised of a central barrel region and two end-caps (referred to as plugs). At the centre sits the tracking systems which are contained in a superconducting solenoid 3 m in diameter, 4.8 m in length and generating a 1.4 T magnetic field. The solenoid is surrounded by electromagnetic (EM) and then Hadronic calorimetry. The final part of the detector is a system of drift cell chambers that comprise the muon detectors.

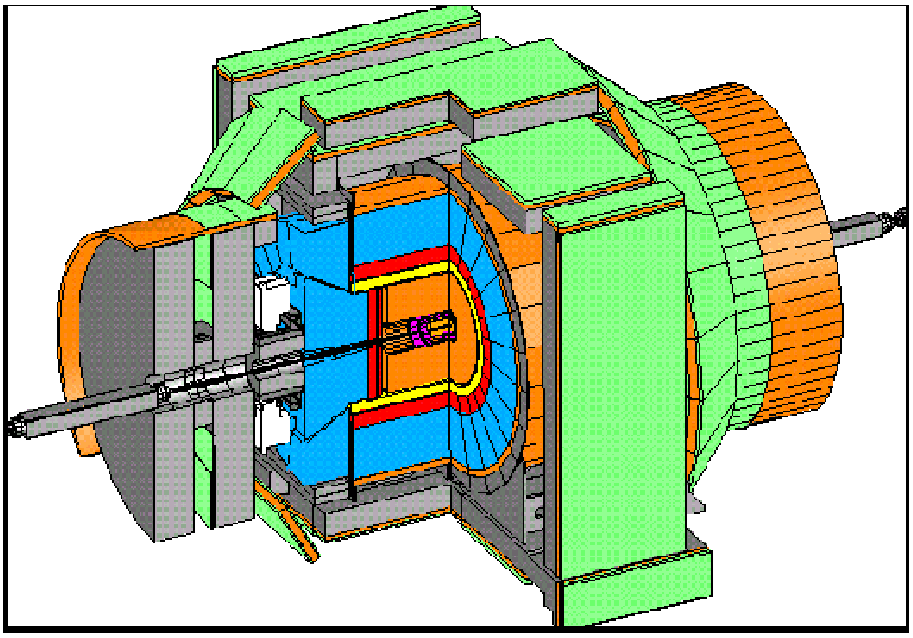

Figure 3.3: The CDF detector

CDF history

The first data run of CDF began in late 1985 and lasted for around 10 years until 1995. In that time CDF collected 108 pb^{-1} of data and discovered the top quark. Along with the Tevatron, CDF shutdown for a series of major upgrades that were completed from 1996 to 2001. This involved a variety of improvements including an entirely new tracking system, plug calorimeters and upgraded muon systems. These improvements increased the acceptance to a larger η and give better b-tagging capabilities. A new Trigger and DAQ were also installed; designed to handle the increased Tevatron luminosity and bunch spacing of 396ns expected after the upgrades

CDF Coordinate System

Discussions of the CDF detector use a right handed Cartesian system, whose origin is at the nominal centre of CDF. The z co-ordinate points along the proton direction and x in the transverse plane pointing horizontally and y vertically as shown in Figure 3.4. A cylindrical co-ordinate system is also used on occasion, with a z-axis again along the proton direction and r and ϕ in the plane orthogonal to this direction. This is also shown in Figure 3.4.

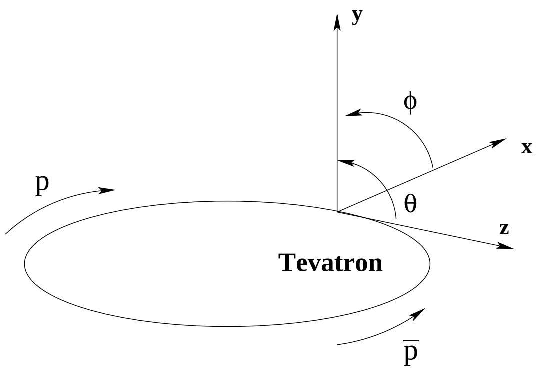

Figure 3.4: The CDF co-ordinate system

An additional angular measure frequently used is pseudo-rapidity, defined by

$$\eta = -ln(tan\frac{\theta}{2})$$

3.2.1 Tracking

The tracking system at CDF comprises of two subsystems, the closest to the interaction point (IP) is the silicon inner tracker, providing coverage up to $|\eta| \leq 2$. Outside of this is the Central Outer Tracker (COT), covering only the central region, $|\eta| \leq 1$.

The Silicon Inner Tracker

The silicon tracker [21] is split into three subsystems: Layer00, The Silicon Vertex Detector(SVX) and The Intermediate Silicon Layer(ISL). All three systems are shown in Figure 3.5. Each of these systems is comprised of many *strips*; single channels of active silicon. The size of the active sensing part of the strip is called its pitch. The strips are then deposited, along with the readout processor, on a wafer to make a *half-ladder*. Two half ladders are then joined together to form a *ladder*; the smallest fully functioning unit of the silicon system. Ladders mounted side by side at equal radius are refereed to as *layers*, those mounted at the same z and varying radius, and are known as *wedges*.

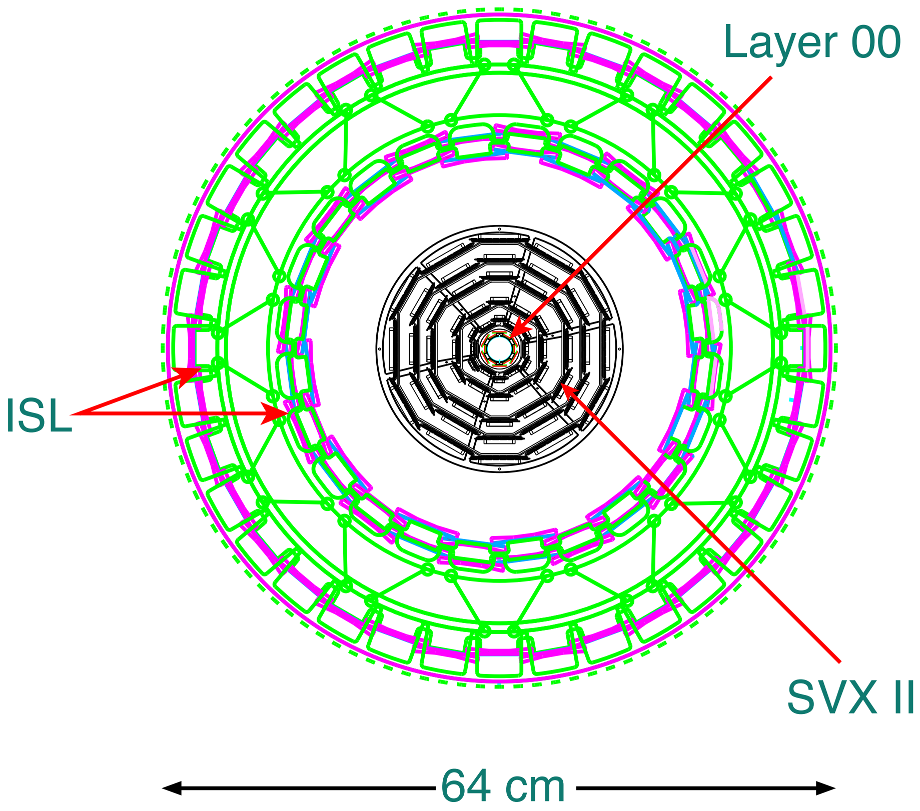

Figure 3.5: End view of the silicon tracker system

Layer00 is the closest detector to the beam pipe at a radius of 1.35 cm. It has complete ϕ coverage and z coverage of ± 78.4 mm from z=0. Constructed from single sided radiation-hard silicon, it attempts to provide the best possible measurement of a track's impact parameter. Layer 00 has a readout pitch of 50μm and a spatial hit resolution of $\approx 15\mu$m.

Outside of this, beginning at a radius of 1.6cm, sits the Silicon Vertex Detector (SVX), which is the bulk of the silicon system. The SVX comprises three barrels that are connected end to end. Each barrel consists of 12 wedges and each wedge has 5 layers of double sided silicon. One side of each strip is axial (giving $r - \phi$ measurement) and the other stereo (giving r-z measurement) to provide complete 3D tracking information. Axial strips have a pitch of 60 to 65 μm and a position resolution of ≈ 20 μm.

Outside of this is placed the Intermediate Silicon Layer (ISL) which has three layers at radii of 20, 22 and 28 cm from the beam and a strip pitch of 112 μm. The central layer covers $|\eta| < 1$ and the outer two layers cover $1 < |\eta| < 2$ giving an extended lever arm for enhanced forward tracking.

Information from the SVX and the ISL can be combined to reconstruct 3D tracks without any input from the COT, known as stand-alone tracking, allowing the system to provide efficiency measurements of the COT performance and also tracking measurements that extend further into the forward region where the COT has no coverage. ISL and SVX information combined gives an impact parameter resolution of 40μm (where 30μm is contributed by the beam line) and a z_0 resolution of 70μm.

The Central Outer Tracker

The second component of the CDF tracking system, the Central Outer Tracker (COT) [22], is a large open cell drift chamber arranged in 8 superlayers surrounding the silicon at a radii of 40 to 132 cm (See Figure 3.6). Each superlayer is made

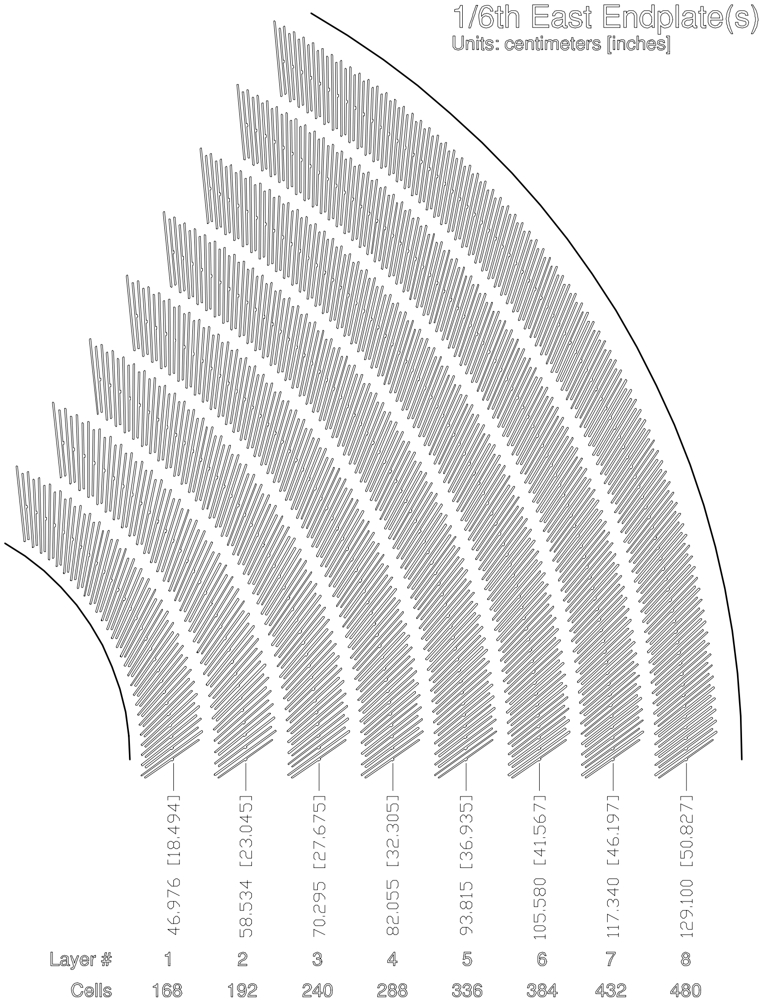

Figure 3.6: The COT superlayers. Cells are tilted at 37° so the radial component of the electric field cancels the magnetic force from the solenoid thereby keeping the drift path to the wires linear and azimuthal

of 12 layers of sense wires alternated with potential wires in a plane, as shown in Figure 3.7. The space between the wires is filled with Argon and Ethane in a 50:50 mix to give a drift velocity of about 100μm/ns, designed with the high luminosity running of Tevatron Run 2 in mind, it ensures that for the given cell size the first hit will arrive before the next bunch crossing. The superlayers alternate between stereo (again for z measurement) and axial (for $r-\phi$), starting

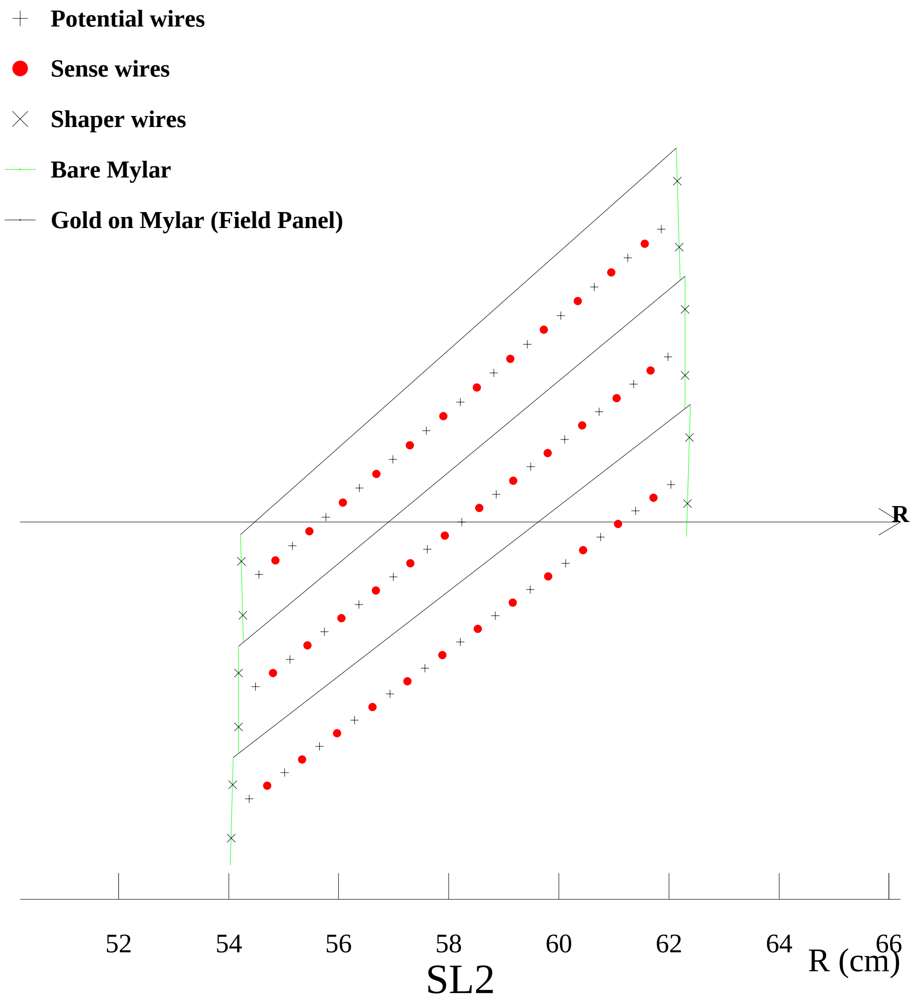

Figure 3.7: Three cells of SL2

with stereo. The stereo wires have a 2° tilt with respect to the z plane. The drift time resolution is better than 2 ns giving a position resolution of 150 μm and a resulting momentum resolution of

$$\sigma_{P_T}(\frac{1}{P_T^2}) = 0.15\%$$

where the momentum is measured in GeV/c.

3.2.2 Calorimeter

Outside the tracking system and solenoid is the calorimetry. The calorimeter is constructed as two physically distinct systems: The central calorimeter ($|\eta| < 1$) and the plug calorimeter ($1.1 < |\eta| < 3.64$). Each of these is subdivided longitudinally into hadronic (CHA [25] in the central and PHA in the plug) and electromagnetic (CEM [23] and PEM [24]) sections. An extra subdetector, called the wall hadronic calorimeter(WHA [25]), covers the gap between the central and plug sections, which is shown in the schematic of the plug calorimeter in Figure 3.8.

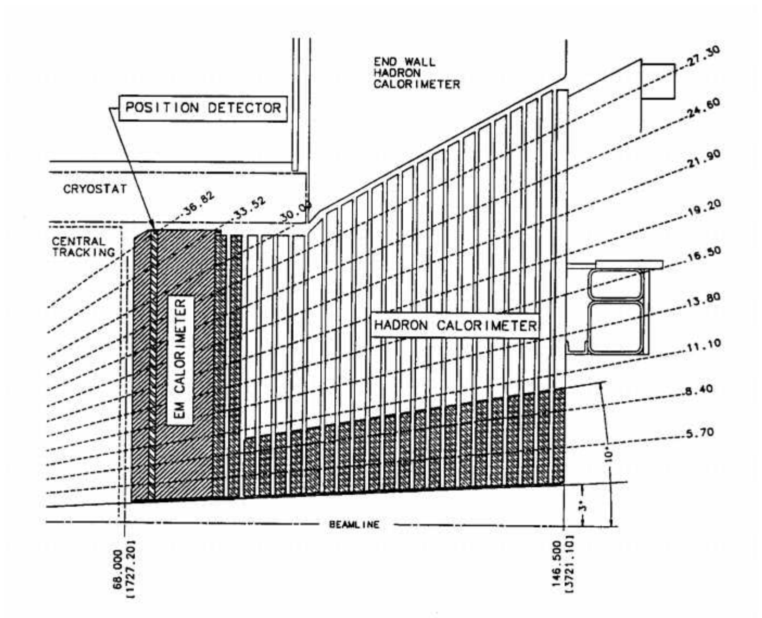

Figure 3.8: Forward calorimeter schematic

Central calorimeter sections are split into two halves at $\eta = 0$, each half containing 24 wedges in ϕ, each wedge split into towers in η where each tower covers 0.1 in η and $15°$ in ϕ. Figure 3.9 shows a view of one of the CEM wedges.

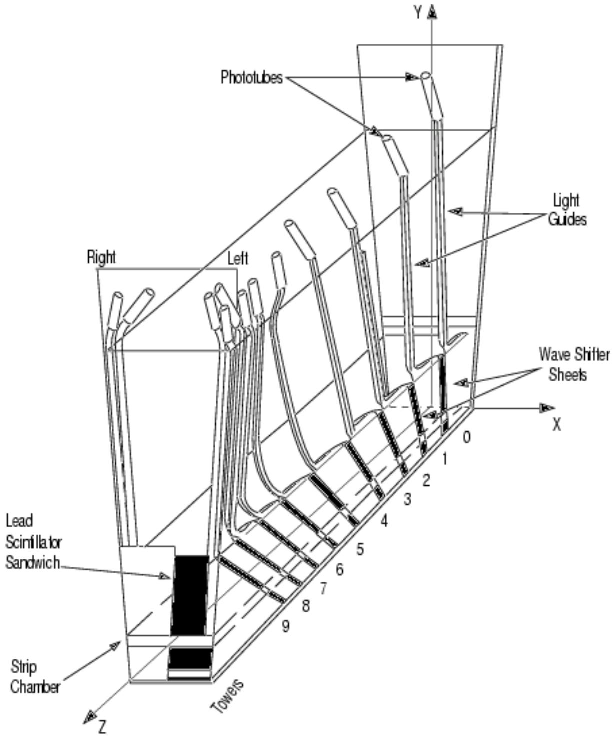

Figure 3.9: CEM wedge

In addition there are two proportional chambers embedded in each tower of the CEM at about 6 radiation lengths near the expected electromagnetic shower maximum (labelled CES [23]). The two chambers are located between $0 < |\eta| < 0.613$ and $0.623 < |\eta| < 1.1$ respectively. Each of these chambers has wires in the $r - \phi$ view and strips in z to record a 3D view of the shower, allowing a precise determination of the incident particles trajectory. This information allows for track-tower matching and has a position resolution of 2 mm at 50 GeV. A similar shower max detector(PES [24]) is located in the plug calorimeter, again at about 6 radiation lengths in the PEM. It is constructed in 45° sectors with two layers, labelled U and V, of scintillating strips. The strips are 5 mm wide, 6 mm thick, of varying lengths and are offset from the radial direction by 22.5°. The PES is also separated into two regions in η with the boundary at $|\eta| = 2.60$.

The electromagnetic portion of the calorimeter is made of layers of lead sheets interspersed with polystyrene scintillator and the hadronic portion with the same design but with steel and acrylic scintillator. The details and energy resolution of the calorimeter subsystems are summarised in Table 3.2.

Detector	CEM	CHA	WHA	PEM	PHA
Coverage	$\lvert\eta\rvert < 1.1$	$\lvert\eta\rvert < 0.9$	$0.7 < \lvert\eta\rvert < 1.3$	$1.1 < \lvert\eta\rvert < 3.6$	$1.1 < \lvert\eta\rvert < 3.6$
Material	Lead	Steel	Steel	Lead	Iron
Wedges	24	24	24	12	12
Towers per Wedge	10	8	6	12	10
Radiation Length	$18\chi_o$	$4.7\lambda_o$	$4.5\lambda_o$	$21\chi_o$	$7\lambda_o$
Energy Resolution	$1.7\% \oplus \frac{13.5\%}{\sqrt{E}}$	$\frac{80\%}{\sqrt{E}}$	$\frac{80\%}{\sqrt{E}}$	$1\% \oplus \frac{16\%}{\sqrt{E}}$	$5\% \oplus \frac{80\%}{\sqrt{E}}$

Table 3.2: Details of the calorimeter subsystems

3.2.3 Muon Systems

Muon detectors [26] are placed outside of the calorimeter where no particles other than muons are expected to penetrate. High-P_T muons leave a track in the COT, very little energy in the calorimeter and then short tracks, known as stubs, reconstructed from the hits in muon detectors. The muon chambers are made of layers of single wire drift chambers. The muon system is split into three separate subdetectors: the central muon detector (CMU), the central muon upgrade (CMP) and the Central Muon Extension (CMX). The coverage of the detectors is shown in Figure 3.10 and the detector parameters are shown in Table 3.3.

The CMU consists of 144 modules with 16 rectangular cells in each module, stacked four deep in the radial direction. Each cell is $6.35 \times 2.68 \times 226$ cm and has a 50μm stainless steel wire in the centre. The CMP consists of a second set of rectangluar, single-wire drift tubes where each cell is $2.5 \times 15 \times 640$ cm. CMX cells differ only in length, 180 cm long. The hit resolution of the chambers is around 250μm in the drift direction and 1.2mm in the z direction [27].

	CMU	CMP	CMX	BMU
pseudo-rapidity coverage	$\|\eta\| < 0.6$	$\|\eta\| < 0.6$	$0.6 < \|\eta\| < 1.0$	$1.0 < \|\eta\| < 1.5$
drift tube length	226 cm	640 cm	180 cm	363 cm
drift tube width	6.35 cm	15 cm	15 cm	8.4 cm
max drift time	800 ns	1.4 μs	1.4 μs	800 ns
total drift tubes	2304	1076	2208	1728
scintillation counter thickness	-	2.5 cm	1.5 cm	2.5 cm
scintillation counter width	-	30 cm	30-40 cm	17 cm
scintillation counter lengths	-	320 cm	180 cm	180 cm
total counters	-	269	324	864
pion interaction length	5.5	7.8	6.2	6.2-20
minimum detectable muon P_T	1.4 GeV/c	2.2 GeV/c	1.4 GeV/c	1.4-2.0 GeV/c
multiple scattering resolution	12 cm/p	15 cm/p	13 cm/p	13-25 cm/p

Table 3.3: Design parameters of the muon detectors. Pion interaction lengths and multiple scattering angles are computed at a reference angle of $\theta = 55°$ in CMX and show a range of values for the BMU.

3.2.4 Trigger And DAQ

The final element of the detector is the data acquisition (DAQ) and trigger system, shown schematically in Figure 3.11. This provides the means by which the electrical signals from the detector hardware are collected, managed and converted into usable data.

The overwhelming majority of collisions that occur are of little physical interest, (known as minimum bias events they are events which pass some minimal trigger requirements i.e. any activity in the detector at a small angle from the beam pipe). Trying to select out the interactions that hold some valuable information is the job of the trigger. This is an essential task given it is not possible to write every event to permanent storage (collisions occur at a rate of 2.5 MHz but can only be written to tape at a rate of 75 Hz). This is made more difficult

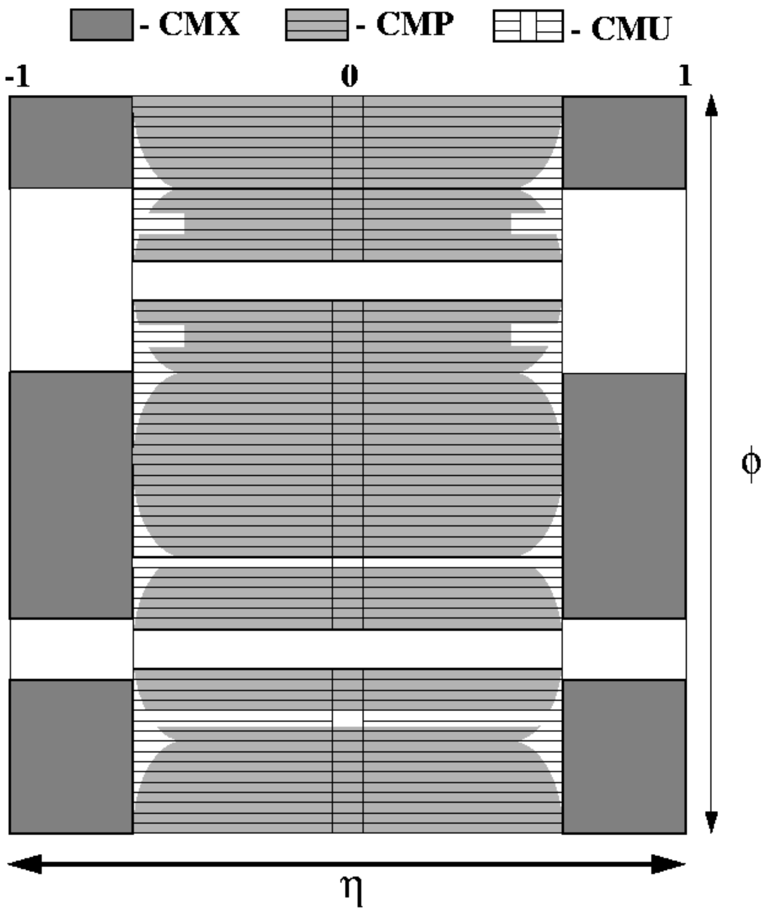

Figure 3.10: The CDF muon system

by the limited time available for deciding whether to keep or to throw away a particular event. This requires both an intelligent and fast decision process.

The trigger is split into three layers of filters. The first, the level 1 trigger, is comprised of custom built electronics (i.e. all hardware) that uses coarse data from the fastest parts of the detector with very little processing to decide if there is anything of interest at all in the event. It contains three parallel synchronous processing streams (one for each of the calorimeter, tracking and muon information) that construct basic physics objects for each event i.e. a crude definition of an electron, jet or muon and the eXtremely Fast Tracker (XFT) also gives reconstructed track information. Each stream then passes these objects to the Global L1 decision unit, which will throw the event out or pass it on to the next filter, the Level 2 trigger, for further processing depending upon the number and quality of the physics objects it receives from the 3 streams. After a Level 1 accept the event is written into one of four Level 2 buffers.

The Level 2 trigger is comprised of several asynchronous subsystems of programmable processors that do some additional processing of the data used at Level 1, thereby refining the information obtained (e.g. basic jet finding algorithm in the L2 cluster finder). Some additional information from other parts of the detector are also added at Level 2 (e.g. the shower-max detectors and SVX) to improve the accuracy with which interesting objects in the event can be identified. While analysing an event in a particular Level 2 buffer, that buffer cannot accept any more L1 accepts, meaning that if all 4 buffers are full the detector incurs deadtime. To minimise this deadtime an L2 buffer must have a latency of less than 80% of the average time between L1 accepts i.e. 20 μs. This latency is achieved through two asynchronous processors each taking 10μs to make its decision.

The final layer of filtering is the Level 3 trigger, which is comprised of 2 systems: the event builder (EVB) and the level 3 farm. The EVB collects the data from each of the detector subsystems and combines them together to form a complete picture of the event at one place for the first time. This whole event is passed to the level 3 farm which consists of 16 subfarms of dual pentium Linux PC's, giving between 14 and 18 processors per subfarm, (plus a converter node that acts as the data input and distribution point for that subfarm). The event is then passed to the level 3 trigger algorithm which is essentially a slimmed down and faster version of the offline reconstruction. This algorithm uses the full detector information and the improved resolution to facilitate tight matching of tracks to muon and calorimeter objects and 3D tracks to make the final decision to write the event to permanent storage.

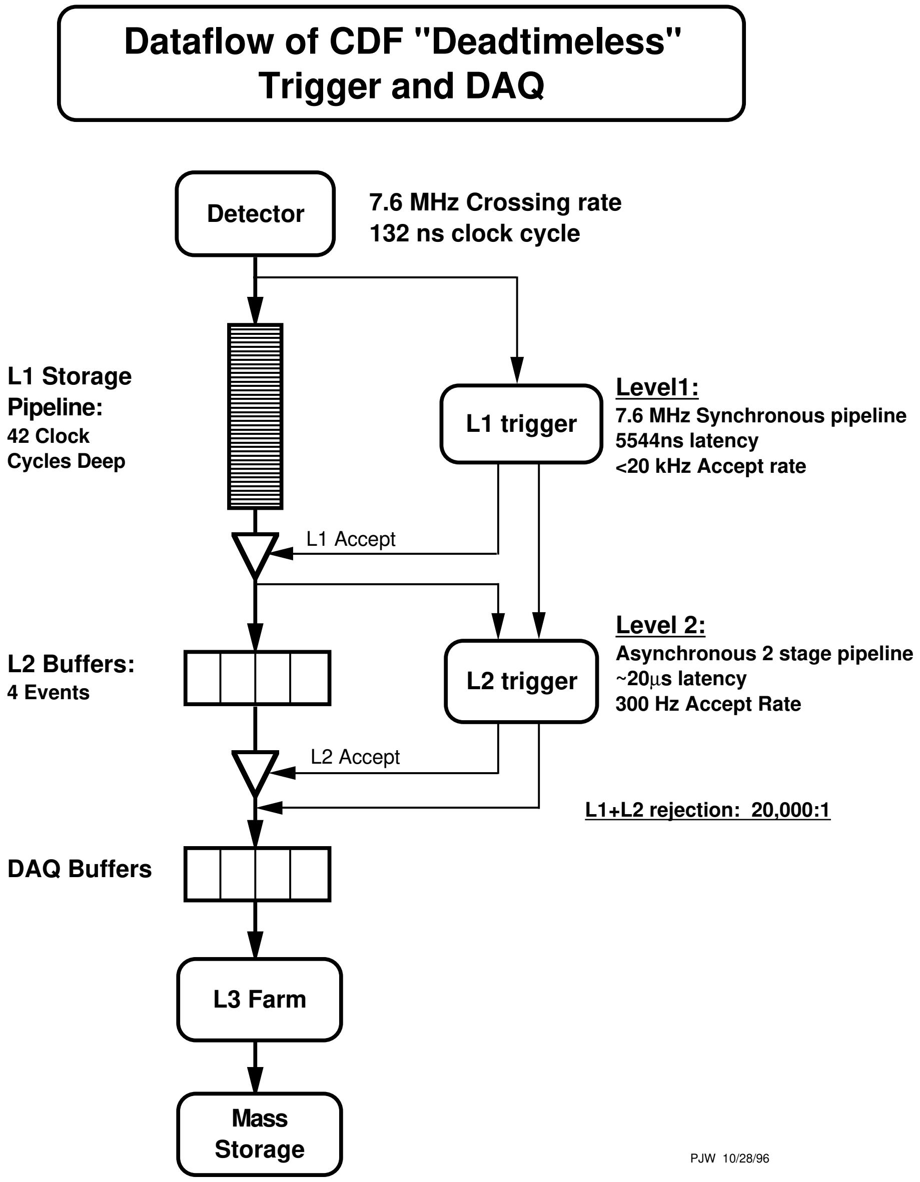

Figure 3.11: The CDF trigger system

Chapter 4

Data Samples and Simulation

Events matching the $WW \rightarrow l\bar{\nu}\bar{l}\nu$ final state are filtered out of the many Tevatron collisions by the previously described three level trigger system. The events are then selected to maximise purity and compared to simulated data that encodes the theoretical predictions.

4.1 The Data Sample

Candidate events are selected from the high-P_T lepton trigger paths in CDF's trigger system.

4.1.1 Online Triggers

The dataset used comprises of a number of different triggers that correspond to different lepton types and detector regions.

High-P_T leptons offer a distinctive and clean signal, with relatively low backgrounds, upon which to base a trigger. The only other signal that could be used would be from the neutrinos, but it is hard to achieve a good signal to background ratio with the $\not\!\!E_T$ measurement available during triggering, due to its poor resolution. Triggering on a lepton requires information from both the tracking, calorimeter and the muon systems in coincidence.

WW events containing electrons are collected from the High-P_T Central Electron Trigger and the Forward Electron Trigger. Muon events are selected from the Central Muon Trigger and the CMX Trigger, all of which are described in the sections that follow.

Trigger requirements are sequential (must pass L1 for consideration at L2, likewise for L3) and so trigger efficiencies are simply the product of L1, L2 and L3 efficiencies.

In order to satisfy the strict timing requirements of the online trigger, simplifications are made in the calculation of certain quantities. Energy measurements in the calorimeter are simplified by using a reduced calorimeter granularity of a 24×24 grid in η and ϕ. These simplified cells are known as trigger towers and span about $15°$ in ϕ and 0.2 in η, covering one or two physical calorimeter towers. The missing energy calculation is simplified by ignoring the longitudinal extent of the proton bunches, $\sigma_z = 20$ cm, and assuming all interactions take place at $z = 0$. The missing energy is then corrected for the real event vertex offline.

The Central Electron Trigger(ELECTRON_CENTRAL_18)

This is a single object trigger that looks for any event that contains an electron candidate in the central region by filtering the events through the following requirements:

- level 1: requires a central EM cluster with $E_T^{EM} \geq$8GeV and for clusters with energy less than 14GeV, E_{HAD}/E_{EM} must be less than 0.125. The trigger tower containing the cluster must have a matched XFT track with

$P_T \geq$ 8GeV/c.

- level 2: requires a central EM cluster with E_T^{EM} ≥16GeV and E_{HAD}/E_{EM} ≤0.125 regardless of cluster energy. An L2 cluster must have a matched XFT track with $P_T \geq$ 8GeV/c.

- level 3: requires a central EM cluster with E_T^{EM} ≥18GeV and E_{HAD}/E_{EM} ≤0.125 for all clusters. The seed tower of the EM cluster must be matched to a fully reconstructed 3D track with $P_T \geq$ 9GeV/c.

The average event rate of this trigger during the data collection period was around 1Hz giving a cross-section of 50nb and the efficiency is measured to be $96.1 \pm 0.2\%$ [28].

The Forward Electron Trigger(MET_PEM)

The tracking coverage is not sufficient to allow for triggers based on calorimetry and tracking to be used in the forward region. To compensate for this, the electron trigger in the forward region looks for $\not\!\!E_T$ in addition to an EM calorimeter object:

- level 1: Forward EM cluster with E_T^{EM} ≥8GeV and E_{HAD}/E_{EM} ≤0.125 for clusters with energy less than 14GeV. The $\not\!\!E_T$ must be more than 15GeV (z=0 assumed)

- level 2: Forward EM cluster with E_T^{EM} ≥20GeV and E_{HAD}/E_{EM} ≤0.125 for all clusters.

- level 3: Forward EM cluster with E_T^{EM} ≥20GeV and E_{HAD}/E_{EM} ≤0.125 for all clusters and $\not\!\!E_T$ greater than 15GeV (z=0)

During the data taking period the average event rate of this trigger was around 0.5Hz giving a cross-section of 25nb. The efficiency of this trigger is estimated in Section 7.2.1.

The Central Muon Trigger (MUON_CMUP18)

The Central muon trigger utilises information from both the CMU and CMP detectors as follows:

- level 1: require a CMU stub with $P_T \geq$6GeV/c matched to a XFT track with $P_T \geq 4.09$ and a stub in the CMP
- level 2: more than one COT track with $P_T \geq$8GeV/c
- level 3: muon track with $P_T \geq$18GeV/c and matched to the CMU stub within $|\Delta X|$ of 10cm and within $|\Delta X|$ of 20cm of the CMP stub.

The efficiency of this trigger is measured to be $88.7 \pm 0.7\%$ [29]

The CMX Trigger (MUON_CMX18)

The final trigger used in this analysis is the CMX trigger:

- level 1: require a CMX stub with $P_T \geq$6GeV/c. Some hits in the central muon wall scintillator extension (CSX) detector and a COT track with $P_T \geq$8.34GeV/c passing through at least 4 super layers
- level 2: No further requirements
- level 3: COT track with $P_T \geq$18 GeV/c matched to the CMX stub to within 10 cm in $r - \phi$.

Table 4.1: Luminosities of dilepton categories

	Luminosity (pb^{-1})
No Silicon(ee)	203.7 $\pm$ 12.2
Good Silicon(ee)	169.6 $\pm$ 10.2
No Silicon(eμ and $\mu\mu$)	193.5$\pm$ 11.6
Good Silicon(eμ and $\mu\mu$)	161.6$\pm$ 9.7
No Silicon with CMX(eμ and $\mu\mu$)	175.3$\pm$ 10.5
Good Silicon with CMX(eμ and $\mu\mu$)	149.8$\pm$ 8.9

The efficiency of this trigger is measured to be $95.4 \pm 0.6\%$ [29]

Any event passing one of these four triggers has its raw data written to permanent storage for later analysis.

4.1.2 Luminosity And Data Quality

For data to be included in the analysis it is required to pass the good run requirements that ensure the appropriate detector components are functioning properly. For example, electrons require the tracker and the calorimeter to be operating normally, muons require the muon chambers in addition. Forward electrons also require the silicon detector for stand alone tracking. For that reason the number of data runs considered to make up the dataset, and therefore the luminosity of the dataset, depends upon the lepton category and is summarised in Table 4.1.

The average luminosity of the sample, taking into account the relative acceptance of the WW dilepton categories is 184$\pm$11 pb^{-1}. The error on this luminosity comes from a variety of sources [19]; the largest errors being the uncertainty on the proton anti-proton inelastic cross-section $\approx$4% and the CLC acceptance used in the luminosity measurement $\approx$4%. Others, such as beam losses and differences in beam conditions over time, gain changes in the PMT's and even the choice of the method used to calculate the luminosity contribute to a total error of 6% on the measured luminosity.

4.2 Event Simulation

Standard Model WW production is completely calculable at LO in QCD and so with an appropriate Monte Carlo program, samples of WW events can be generated from the theory prediction and used to explore event yields and kinematics.

Additional Monte Carlo samples are also produced to predict the backgrounds that will be discussed later. Samples produced with leading-order generators like PYTHIA have corrections applied to their cross-sections to account for the NLO matrix elements missing from the calculation. These corrections are known as k-factors and are detailed in the discussion of the background samples in chapter 8.

4.2.1 MC Generators

The default generator used in this analysis is PYTHIA [6], with additional samples produced with ALPGEN [51]+HERWIG [7] mostly for the purpose of cross-checking and deriving errors. PYTHIA and HERWIG differ primarily in the modelling of the outgoing parton showering and hadronisation. Interfacing ALPGEN to HERWIG provides a way of producing samples with specified numbers of additional partons to check jet multiplicities. NLO predictions of the cross-section are provided by MCFM [8] as described earlier. A second NLO program called MC@NLO [56] is also used to cross-check MCFM results. MC@NLO provides a method of matching the NLO calculation of a given QCD process with the parton showers in such a way that the transition between the hard and soft/collinear-emission regions is smooth, but lacks any description of W boson anomalous couplings or the spin correlations in W boson decays.

4.2.2 WW Monte Carlo Predictions

The event yields, efficiencies and kinematics of the signal are modelled by a large PYTHIA sample of $WW \to l\bar{\nu}\bar{l}\nu$ events. These are discussed in more detail later in Section 7.1. The cross-section is calculated to NLO with MCFM which was discussed earlier in Section 2.2.1. The effect of anomalous couplings are modelled by a combination of these two generators.

MCFYTHIA

MCFM run in leading order can be interfaced to PYTHIA (from here on referred to as MCFYTHIA), using a method detailed in [30], in order that the latter program can provide parton showering, fragmentation and hadronisation. This allows realistic event samples to be generated that include the anomalous couplings in the WWZ and $WW\gamma$ vertices, not currently available in PYTHIA.

4.2.3 Detector Simulation

The samples of Monte Carlo generated events are then passed through the full CDF detector simulation. The detector simulation is a GEANT-3 [31] based program that uses a Monte Carlo technique to simulate the interaction between particles and detector material. The Program also simulates the response of readout electronics.

For each event in the generated samples, the four-momentum of the particle is used to simulate the path of the particle and the interactions it undergoes as it passes through the detector. The description of the detector is as detailed as possible and incorporates an accurate description of the multiple scattering, bremsstrahlung and shower development of the subsequent particles produced.

The result of this simulation is a dataset that describes both the theoretical model of WW production and also renders as accurate a description as possible of their expected appearance in the CDF detector.

The output of the detector simulation consists of data banks that mimic the data banks from the DAQ system of the real detector, allowing the use of identical offline reconstruction software to be used on real and simulated data.

Chapter 5

Event Reconstruction

This chapter provides a description of the identification and reconstruction of the final state objects used in the selection of $WW \rightarrow l\bar{\nu}\bar{l}\nu$ events for this analysis.

5.1 Track Reconstruction

Two distinct types of tracks are used in this analysis. Muons and any electron in the central region of the detector use hit based, unseeded tracks, formed using information from the COT and are labelled COT tracks (these tracks may have silicon hits attached also, but it is not a requirement). Electrons in the forward (or plug) region rely on the silicon detector and its extended η coverage to provide the required tracking information. These are labelled as Phoenix tracks.

5.1.1 COT Tracking

The COT tracking algorithm [32] begins by forming segments in each of the axial super layers by grouping together hits based upon the position and timing of each hit. The segments are then linked together to form 2D tracks in the

$r-\phi$ view. The segment finding algorithm is then run over the stereo layers and the resulting segments are added into the 2D tracks where possible to provide z information. If no segments are found in the stereo layers, individual hits may be considered for attachment to the 2D tracks to provide z information in place of the stereo segments. The resulting tracks have a momentum resolution of $\sigma_{P_T} = 0.0015\ P_T^2$ GeV/c and the efficiency of the COT tracking, measured with central electron W events triggered with no track requirements, was found to be 99.3% [35] for these high$-P_T$ tracks. Additional offline requirements made on COT tracks are listed in Table 5.1.

Beam Constrained COT Tracking

Raw COT resolution can be significantly improved by imposing a constraint that the track pass through the beam spot. This is done by adding an additional hit to the track at the beam spot and recalculating all track parameters. The beam spot is found by averaging the point of closest approach to the beam of all tracks in a single Tevatron store. The resolution of the beam spot, when calculated in this way, is found to be about 30μm.

Curvature Correction

Misalignments in the COT generate false curvature measurements that are seen as an azimuthal dependent bias in the E/P distribution (assuming E is not charge biased). This bias, mirrored between electrons and positrons, is corrected with the expression below [36], where Q is the charge, P_T the beam constrained momentum and ϕ is azimuthal angle of the track. After the correction E/P is flat in ϕ and equal for electrons and positrons.

$$\frac{Q}{P_T^{corr}} = \frac{Q}{P_T} - 0.00037 - 0.00110 \times \sin(\phi + 0.28)$$

5.1.2 Phoenix Tracking

Specifically designed for the reconstruction of high-P_T electromagnetic objects in the forward region, Phoenix tracking [33] is a seeded algorithm that uses the event vertex and calorimeter objects to construct silicon tracks. The algorithm starts with the event vertex(which will be defined shortly) and looks for any EM calorimeter cluster. The position of the vertex, the position of the cluster (as given by the shower-max detector, section 3.2.2) and the cluster's associated E_T measurement define two paths between the points which differ only in the assumed sign of the charged particle. These two possible paths are then scanned for hits in the silicon detector to provide a well defined and precise track in a busy part of the detector. Due to the seeding used in the algorithm, the resolution of the resulting Phoenix tracks is dominated by the energy uncertainty of the PEM cluster. Hence Phoenix tracking is for electron identification purposes only, helping to distinguish electrons in the plug from jets and photons and not to improve electron kinematics which are taken from the calorimeter. The efficiency of the algorithm has been measured with $Z \to ee$ events and found to $83.2 \pm 1.0\%$ [37]. Additional quality cuts are then applied to these tracks as listed in Table 5.1.

5.1.3 Event Vertex

In events with a well defined high-P_T lepton, the event vertex is set to be the z co-ordinate of the track's closest approach to the beam line (z_0). In the case of

Track Type	Variable	Cut Requirement
COT	Good Super Layer	≥ 7 Hits
	$N^{Axial}_{Good\ Sup\ Lay}$	≥ 3
	$N^{Stereo}_{Good\ Sup\ Lay}$	≥ 3
Phoenix	$\|z_0\|$	≤ 60.0 cm
	N^{hits}_{svx}	≥ 3
	$\Delta_{\mathrm{R}}(\mathrm{Track, PES})$	≤ 3 cm

Table 5.1: Offline criteria for a good quality track for the two types of track used in this analysis. $N_{Good\ Sup\ Lay}$ is the number of good axial or stereo super layers and $\Delta_{\mathrm{R}}(\mathrm{Track, PES})$ is the distance of the Phoenix track's trajectory from the PES when extrapolated into the plug calorimeter.

multiple leptons the track of the highest-p_T lepton is used. In events that contain only forward electrons with Phoenix tracks, where an event vertex is required as an input to the tracking algorithm, a more global reconstruction is used. All tracks reconstructed in the COT are grouped together according to their z_0 when projected to the beamline and a weighted average z_0 is calculated and used as the event vertex.

5.2 Electron Reconstruction And Identification

As mentioned above, this analysis uses two different classes of electrons that depend on the region of the detector (Central or Plug) in which they are detected and therefore the type of tracking that is used to define the electron object. The reconstruction algorithm for the two different electron types is given in the sections below.

5.2.1 Electrons In The Central Region

Constructing an electron object [34] in the central ($|\eta| < 1$) region of the detector requires three objects from the detector: a cluster in the EM calorimeter, a track pointing to that cluster and a shower-max cluster in the CES associated with the track.

The reconstruction algorithm starts by finding all towers in the calorimeter with transverse energy (E_T) more than 3 GeV; these are the seed towers. Taking each tower in turn, ordered in E_T and starting with the highest, the towers on either side in η in the same wedge are checked for electromagnetic or hadronic energy deposits above 100 MeV; if both pass then the seed tower and the two shoulder towers become a cluster. Clusters are not allowed to cross physical boundaries in the detector (central to plug) and any tower that is chosen as a shoulder tower is removed from the seed list.

For this cluster to become a candidate for an electron object it must have a COT track whose position and direction, when extrapolated to the plane of the shower-max detectors of the wedge that contains the cluster, is within 25 cm in the x-ϕ plane (where x is the local CES x co-ordinate) and 38 cm in z from the centre of the EM seed tower. If there is more than one of these matching tracks then the highest P_T track falling inside the seed tower, or not more than 5 cm outside, is chosen. The EM energy of the cluster must be above 5 GeV and the cluster's corresponding hadronic towers must have less than 0.125 of the total EM energy (to reduce background from jets). In the case of electrons the shower-max cluster associated with the COT track is also added into the candidate electron object.

Corrections And Calibrations

To provide an improved precision in the energy measurement of the CEM, three effects need to be corrected for: A variation in the response of the calorimeter as a function of the local x and z position within the tower (where x is the distance in cm from centre line of tower and z the distance in cm along the centre line, starting from the base), a time dependent tower-to-tower variation and an overall energy scaling. These are discussed below.

Within a given wedge, EM showers close to the edge of a tower generate a lower response than those in the very centre of the tower. A face correction for this effect was calculated using 1994 test beam data [38] and applied to all EM objects in both the data and the simulated data. The correction also accounts for light loss in the wavelength shifting fibres and light attenuation in the scintillator. However, after this correction, the data still displays some x dependence. This is corrected for by averaging the values of E/P in the range 0.8 to 1.25 within each tower (Where E is the energy in the tower and P the momentum of the COT track for that cluster) and deriving the following correction:

$$E_T^{corr} = \frac{1.015}{1 + 0.000157x^2} \times E_T$$

.

Tower-to-tower variation is corrected by using the data to calculate the average E/P in a particular tower over time and then applying the inverse of this average value to the data (real data only, the simulation response is uniform), so that the final measured average E/P is unchanged but the distribution is flattened. This correction gives a 5% improvement in the CEM resolution.

The absolute energy scale is calibrated using a data sample of $Z \rightarrow ee$ events in the central region. Within a window of one decay width of the Z boson, a Gaussian is fitted to the di-electron mass and the energy scale is iteratively tuned until the fitted mass peak is at 91.18 GeV/c^2.

Central electron Identification

Once the electron candidate objects have been formed they are passed through the electron identification cuts to select a pure electron sample and reduce the backgrounds. The electron identification cuts used here are derived by analyses of $Z \rightarrow ee$ [39]. The quantities used for this selection are:

Transverse Electromagnetic Cluster Energy: The transverse electromagnetic cluster energy (E_T) is defined as the EM energy of the cluster times sinθ where θ is the angle of the track matched to the electron.

Had/EM: The ratio of hadronic energy to electromagnetic energy in the towers that make up the cluster.

Isolation: The ratio $E_T^{iso}/E_T^{cluster}$, where E_T^{iso} is the transverse energy inside a cone defined by $\Delta R = \sqrt{\Delta\eta^2 + \Delta\phi^2} \leq 0.4$ centred on the EM cluster minus the transverse energy of the cluster, $E_T^{cluster}$.

$\boldsymbol{\chi^2_{strip}}$: χ^2 of the fit between the pulse height shape of the energy deposited on each of the 11 strips in z in the CES cluster compared to the test-beam data expectation.

Lshr: A likelihood variable derived by comparing the profile of the energy distributed across the towers in the cluster, called the "lateral sharing profile" of the shower, to the expected profile measured from test-beam data. This variable helps distinguish real from fake electrons.

$$L_{shr} = 0.14\Sigma_i \frac{E_i^{adj} - E_i^{expected}}{\sqrt{(0.14\sqrt{E})^2 + (\Delta E_i^{expected})^2}}$$

- E_i^{adj} is the measured energy in the tower adjacent to the seed tower
- $E_i^{expected}$ is the expected energy in the adjacent tower as predicted by the test-beam data
- $0.14\sqrt{E}$ is the error on energy measurement
- $\Delta E_i^{expected}$ is the error on fit to test-beam expectation

E_T/P_T and $\boldsymbol{P_T}$: The transverse momentum of the electron measured from its track and the ratio of the E_T of the electron cluster to the P_T of the track are used to remove fake electrons but also removes real electrons that have emitted a large fraction of their energy in bremsstrahlung radiation.

$\boldsymbol{Z_{vertex}}$: The origin of the interaction (typically the z_0 of the track of the highest P_T lepton in the event).

$\mathbf{Q \cdot \Delta X}$: The difference between x measured in the CES and those measured by extrapolating the track out to the CES. Applied to identify electrons that have emitted bremsstrahlung radiation and consequently have a CES cluster inconsistent with the track trajectory and to reject jets faking electrons.

Fiduciality: Ensures the electron is inside the volume of the detector that is active i.e. well instrumented:

- ϕ location of CES $\leq$ 21 cm from centre of each wedge
- $|z|$ location between 9 and 230 cm.
- seed tower must not be highest η tower or near the solenoid cooling access area.

Triggers: Ensure the electron passed the appropriate triggers, which are described in section 4.1.1.

Conversions: Electrons consistent with conversions are removed by searching for partner tracks with the opposite charge that point to a common point of origin that also satisfy the following conditions [45]:

- $r - \phi$ separation < 0.2 cm
- $|\Delta cot\theta| < 0.04$

The cuts placed on these quantities are shown in Table 5.2. The efficiency of these cuts is 82.5$\pm$ 0.5% in $Z \rightarrow ee$ data [41]

Variable	Cut Requirement
E_T	> 20 GeV
Fiduciality	CES based
Had/EM	$< 0.055 + (0.0045 \times E)$
p_T	$>$ 10GeV/c
E/p	< 2.0 || $E_T > 50$ GeV
Track Quality	see Table 5.1
L_{shr}	< 0.2
χ^2_{strip}	< 10.0
$Q \cdot \Delta X$	$-3.0 < Q \cdot \Delta X < 1.5$ cm
$\|\Delta Z\|$	< 3.0 cm

Table 5.2: Criteria for electron candidate to be classified as a central electron (labelled CEM).

5.2.2 Electrons In The Forward Region

In many respects the reconstruction and identification of forward electrons is identical to that of central electrons. Therefore the following sections will concentrate only on the differences.

Constructing The Forward Electron Candidates

Construction of a forward electron candidate object follows the same logic as in the central case but with PEM and PES clusters rather than CEM and CES clusters. In the forward case there is no track in the COT from which to match the PES cluster to the PEM cluster; instead the matching simply uses the highest energy PES cluster in the seed tower.

Corrections And Calibrations

As in the central region a number of effects must be calibrated and corrected to give an accurate energy measurement. Again, x and z dependence is removed with a face correction which is derived from test beam data. The towers in the plug vary in size so a separate correction is needed for each tower. A uniform ϕ response can then be obtained by applying this map across all ϕ regions. Secondly a time dependent overall energy scaling is required to obtain the correct absolute scale. The method is identical to the one used in the central region, i.e. iteratively scale the di-electron mass so that it matches the Z mass [42]. The correction itself is shown in Table 5.3.

Run Range	Plug, $\eta > 0$	Plug, $\eta < 0$
141544 $\rightarrow$ 159600	1.069	1.057
159600 $\rightarrow$ 163600	1.097	1.084
163600 $\rightarrow$ 168890	1.089	1.077

Table 5.3: Energy scale factors applied to plug EM clusters in data events.

Plug Electron Identification

The only additional variables used in plug electron identification are as follows:

PEM 3×3 **Fit** χ^2: Compares the EM shower profile of the PEM cluster with test beam data.

PES 5×9: The ratio of the energy in the central 5 strips of the PES cluster to the energy of the whole cluster of 9 strips. Basically an isolation variable.

The identification cuts used are listed in Table 5.4 and the efficiency of these cuts is 85.9±0.8% in $Z \to ee$ data [43].

Variable	Cut Requirement
E_T	> 20 GeV
Fiduciality	PES based $1.2 < \|\eta\| < 2.0$
E_{HAD}/E_{EM}	$< 0.05 + 0.026 \cdot ln(\frac{E_{EM}}{100})$ (if $E_{EM} > 100$ GeV) < 0.05 (if $E_{EM} < 100$ GeV)
PEM 3×3 Fit tower	$\neq 0$
PEM 3×3 Fit χ^2	< 10
PES 5×9 U and V	> 0.65
Track Quality	see Table 5.1

Table 5.4: Criteria for electron candidate objects to be classified as plug electrons (labelled PHX)

5.3 Muon Reconstruction And Identification

Muon identification is driven by the separate muon subdetectors and in each case has slightly different identification requirements, though in general they comprise a COT track that is matched to a track segment (or "stub") in one of the muon detectors. The stubs are matched to a track by requiring that the separation, ΔX, is below some threshold.

5.3.1 Muon Candidate Types

In all cases a muon candidate is required to have a track pointing to an energy deposit in the calorimeter consistent with a minimum ionising particle. Additionally, muon fiduciality requirements may be imposed. The candidates are then separated into different muon types accordingly:

1. **CMUP muon**: has stubs in both the CMU and CMP detectors and $|\Delta X|_{\mathrm{CMU}} < 3\,\mathrm{cm}$ and $|\Delta X|_{\mathrm{CMP}} < 5\,\mathrm{cm}$ respectively.

2. **CMX muon**: has one stub in the CMX detector, with $|\Delta X|_{\mathrm{CMX}} < 6\,\mathrm{cm}$

3. **Non-Triggering muon**: Additional, non triggered muon categories are allowed to be the second lepton in a dilepton event. They are divided into 3 different sub-categories that appear in the following ways:

   (a) **CMU-only** (**CMP-only**) with a stub in the CMU (CMP) detector and non fiducial in the CMP (CMU) detector.

   (b) If there are no muon detector stubs, the minimum ionising high P_T isolated track will be classified as a stubless or **CMIO** muon.

5.3.2 Selecting Muons

The quantities used for the final muon identification are the same for all muon types and are as follows:

$\mathbf{P}_{\boldsymbol{T}}$: Transverse momentum of the muon's COT track.

$\mathbf{z_0}$: The location in z of the point of intersection of the muon's track to the beamline.

$\boldsymbol{\Delta x}$: The track-stub matching distance in the muon chamber.

Quantity/Variable	Cut Requirement
Track P_T	>20 GeV/c
Track $\|z_0\|$	$<$ 60 cm
E_{EM}	$<$ 2+Max(0,0.0115(P-100)) GeV
E_{HAD}	$<$ 6+Max(0,0.028(P-100)) GeV
Track $\|d_0\|$	0.2 cm (if no silicon hits attached) 0.02 cm (if silicon hits attached)
CMX muon	COT exit radius $>$ 140 cm.
Track quality	see Table 5.1

Table 5.5: Criteria for muon candidate objects to be classified as muons

$\mathbf{d_0}$: The impact parameter (distance of closest approach in $r-\phi$ of the track to the beamline)

cosmic ray filter: CDF algorithm to flag events consistent with a cosmic ray passing through the detector.

The cuts on these variables are shown in Table 5.5. The ID efficiency for CMX muons measured in $Z \rightarrow \mu\mu$ data is 90.1±0.8% [29] and 85.1±0.7% for CMUP muons.

5.4 Jet Reconstruction

The fragmentation of quarks and gluons into colourless bound states, known as hadrons, results in multiple tower clusters in both the Electromagnetic and Hadronic calorimeter and multiple tracks. These objects are known as jets. Several algorithms exist to define a jet object, all of which are based on the same goal of bounding the jet within a portion of the detector to provide a measurement of its energy while minimising the amount of energy from the rest of the event that is included. The cone algorithm [44] used in this analysis is a simple algorithm that, schematically, forms a cone of radius $R = \sqrt{(\Delta\eta)^2 + (\Delta\phi)^2} = 0.4$ around the highest energy tower in a particular neighbourhood of the detector and then sums the energy of the towers in that cone.

In this analysis jets are reconstructed using the cone algorithm described above and are required to have $|\eta| < 2.5$ and $E_T > 15$ GeV. Since the calorimeter is not 100% hermetic, there is a large amount of energy that is absorbed by non-active material or lost prior to the calorimeter that needs to be accounted for, if the measured energy of the jet is to be accurate. The corrections are applied one by one and are termed Levels.

- Level 1 - Relative corrections: corrects to ensure the jet energy scale is uniform in η and across the different calorimeter systems (CHA, WHA etc).

- Level 2 - Stability corrections: corrects for time dependence and ageing in the phototubes.

- Level 3 - Raw energy scaling of central calorimeter: corrects CEM Run 2 response to that of Run 1

- Level 4 - Multiple interactions: the energy from different $p\bar{p}$ interactions during the same bunch crossing can fall inside the jet cluster, increasing the energy of the measured jet. This is corrected by subtracting this contribution on average, where the average is derived from minimum bias data and is parameterised as a function of the number of vertices in the event, which closely follows the instantaneous luminosity.

- Level 5 - Absolute energy scale: corrects for any non-linearity in the calorimeter response and energy loss in the un-instrumented regions of each calorimeter by using the ΣP_T of the particles within the cone of same size around the parton direction which matched the jet direction with $\Delta R < 0.5$.

Reconstructed electrons are also explicitly removed from the list of possible jets to remove any overlap in final state object definitions.

5.5 $\not\!\!E_T$ Reconstruction

Any leptonic decay of a W boson produces a neutrino that does not interact in any directly measurable way with the CDF detector. Their presence can only be inferred from the energy they take away from the hard interaction. The difficulty faced at hadron colliders is that there is no exact measurement of the energy that went into the interaction. The only method that remains is to look in the transverse plane of the event where the input energy is known to be zero and define the missing E_T as

$$\not\!\!E_T = -\left(\sum_{towers} E_T\right)$$

Where all towers (electromagnetic and hadronic) in the region $|\eta| < 3.6$ are included in the sum if they have over 100 MeV energy deposited within them. The event vertex used in the calculation is the z_0 of the highest energy lepton track.

However, neutrinos will not be the only source of $\not\!\!E_T$. Any final state object (jets, electrons) can be badly measured (perhaps some of the shower disappears down a calorimeter crack) and thereby generate fake $\not\!\!E_T$ (to be discussed in more detail later). There is also some difficulty in events with muons, since they leave only a fraction of their energy in the detector (a MIP in the calorimeter) and hence any event with a muon will generate a large value of $\not\!\!E_T$ if the simple tower based definition above is used. The value of $\not\!\!E_T$ must therefore be corrected in events with muons by replacing the measured E_T from the muon's MIP signal with the P_T from its track. A second correction is also applied after the energy of the jets has been corrected as described in the previous section. The final measured resolution of the $\not\!\!E_T$ is found to be $(0.646 \pm 0.016)\sqrt{\Sigma E_T(\mathrm{GeV})}$. [46]

Chapter 6

Event Selection

The selection of $WW \rightarrow \bar{l}\nu l\bar{\nu}$ events begins with selecting events that contain leptons using the lepton identification cuts detailed in Chapter 5 and then applying kinematic and topological cuts that single out the $WW \rightarrow \bar{l}\nu l\bar{\nu}$ events from those background events that have the same leptonic final state.

6.1 Selecting Signal

Candidate $WW \rightarrow \bar{l}\nu l\bar{\nu}$ events are selected by searching for events with two high-p_T leptons (electrons or muons only), one from each W decay and $\not\!\!E_T$ greater than 25 GeV, to indicate the presence of neutrinos. Since this simple selection suffers from considerable backgrounds, additional requirements are added to reduce these backgrounds and provide a better signal-to-background ratio.

6.2 Background Rejection

Isolation requirements are imposed on the leptons to reduce backgrounds from events with jets or photons that fake leptons. Leptons are considered isolated if the fraction of the additional E_T found in a cone with radius $R = \sqrt{\Delta\phi^2 + \Delta\eta^2} = 0.4$ around the electron (muon) is less than 10% of the electron E_T (muon P_T). The corresponding isolation requirement calculated using track momenta rather than calorimeter energy is also imposed. Leptons passing the ID cuts from Chapter 5 and these additional isolation requirements are refered to as isolated baseline leptons. The leptons are required to have opposite charge, further helping to reduce the background from events containing fake leptons which will have random charge. Candidates with three or more isolated leptons are rejected to remove the background from the other heavy diboson channels WZ and ZZ, which are otherwise indistinguishable. The background from $t\bar{t}$ production is minimised by requiring the events to have no jets with E_T >15 GeV within the pseudo-rapidity range $|\eta^{jet}| < 2.5$.

The candidates are classified into three dilepton final states: ee, $e\mu$, $\mu\mu$ and the remaining selection becomes dependent upon those flavour combinations. Any CMIO muon in events in the $e\mu$ channel is required to be fiducial in the calorimeter to remove the large background from $Z \to ee$ where one of the electrons falls into a gap in the calorimeter coverage. The rejection of $Z \to l\bar{l}$ in the like-flavour channels is discussed in the next section.

6.3 Drell-Yan Background

Specific attention needs to be paid to the Drell-Yan background, $p\bar{p} \to \gamma * /Z + X \to l^+l^- + X$, given the Drell-Yan cross-section is almost 2000 times the WW cross-section. Hence if not properly controlled this background can swamp the signal.

Drell-Yan production results in two opposite sign high-P_T isolated leptons but has no neutrinos and therefore no *real* $\not\!\!E_T$. Figure 6.1 shows the $\not\!\!E_T$ distributions for signal WW Monte Carlo compared to a small background Monte Carlo sample of Drell-Yan. It is the high $\not\!\!E_T$ tail of the Drell-Yan distribution that constitutes the background to the WW signal. These tail events are those which have faked the required $\not\!\!E_T$ in one of two ways: mis-reconstruction of one of the leptons or mis-reconstruction of the hadronic recoil associated with the Z.

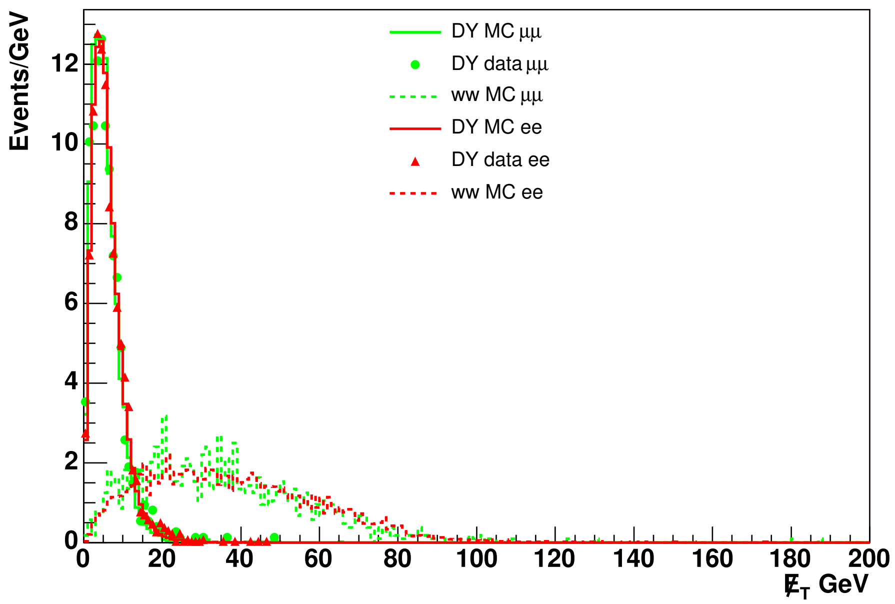

Figure 6.1: $\not\!\!E_T$ of signal and background events in the Z window, $76 < M_{l\bar{l}} < 106 GeV$, with 2 isolated baseline leptons in $126pb^{-}1$ of data, normalised to equal area. No other WW cuts have been applied.

Events where the $\not\!\!E_T$ direction is within 20° in ϕ of a lepton are removed to reject the background from events where lepton mis-reconstruction has given rise to the $\not\!\!E_T$. This cut is released at $\not\!\!E_T$ = 50 GeV to recover detection efficiency, since it is very unlikely that $\not\!\!E_T$ larger than 50 GeV has been faked. Figure 6.2 shows this to be a very conservative cut that does an excellent job at removing these lepton mis-measured, fake $\not\!\!E_T$ events. It is believed that the remaining

Drell-Yan background in this analysis is generated primarily by mis-measured jet activity.

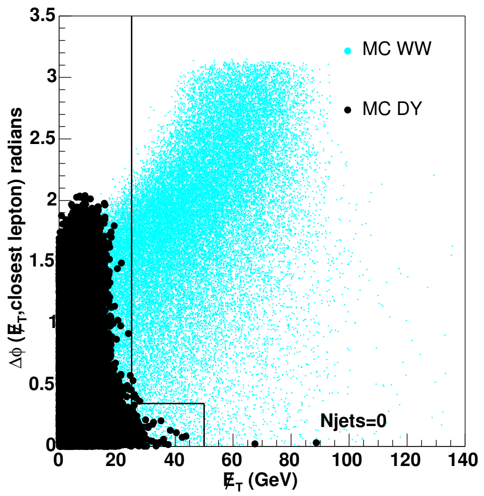

Figure 6.2: $\Delta\phi$ cut as a function of $\not\!\!E_T$

As mentioned above, events with jets are rejected to remove the large and uncertain background from top dilepton production. Even after this veto however, there will be hadronic activity below the E_T cut used for the jet veto that will generate fake $\not\!\!E_T$.

Weighting the $\not\!\!E_T$ by the amount of calorimeter activity makes it an improved discriminator between signal and background. This variable, which shall be called missing energy significance ($\not\!\!E_T^{sig}$), is defined as:

$$\not\!\!E_T^{sig} = \frac{\not\!\!E_T}{\sqrt{\Sigma E_T}} \approx \frac{\not\!\!E_T}{\sigma_{\not\,E_T}}$$

Where ΣE_T is the sum of the E_T of every tower in the event and $\sigma_{\not\,E_T}$ is the resolution on the $\not\!\!E_T$ measurement. So, for a given $\not\!\!E_T$: the higher the activity in the calorimeter, the less significant the $\not\!\!E_T$.

The introduction of the ΣE_T quantity poses a problem. This analysis considers two lepton flavours, electrons and muons. Obviously electrons and muons have a very different presence in the calorimeter and therefore different ΣE_T (Figure 6.3). This gives rise to different $\not\!\!E_T^{sig}$ distributions (Figure 6.4) for the different lepton flavours and hence different cuts for signal and background in the ee channel compared to the $\mu\mu$ channel.

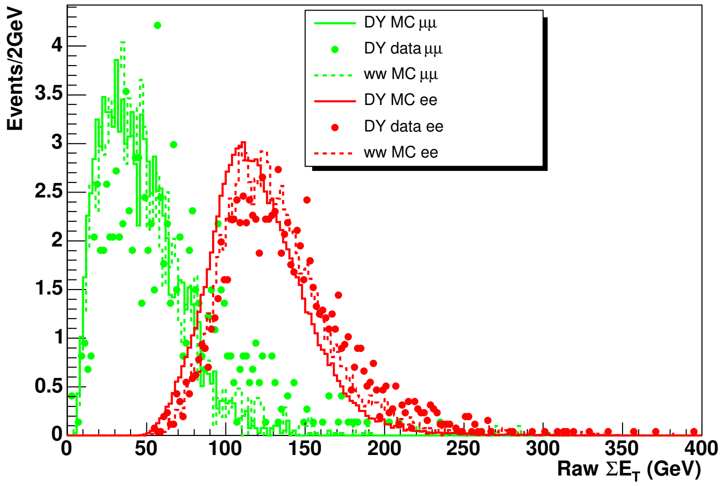

Figure 6.3: Raw ΣE_T of signal and background events in the Z window with 2 isolated baseline leptons. No other cuts applied.

To maintain the flavour invariance in the event selection, this difference in the ΣE_T variable needs to be accounted for. This is achieved in the same way that the $\not\!\!E_T$ is corrected for the presence of muons, by adding the P_T from the muon's beam constrained track (see section 5.5), as an approximation to its E_T, into the ΣE_T. To prevent over correcting, the E_T associated with the muon MIP towers is subtracted. This then gives a quantity that is flavour independent. The ΣE_T distributions after the muon correction are shown in Figure 6.5 and the resulting

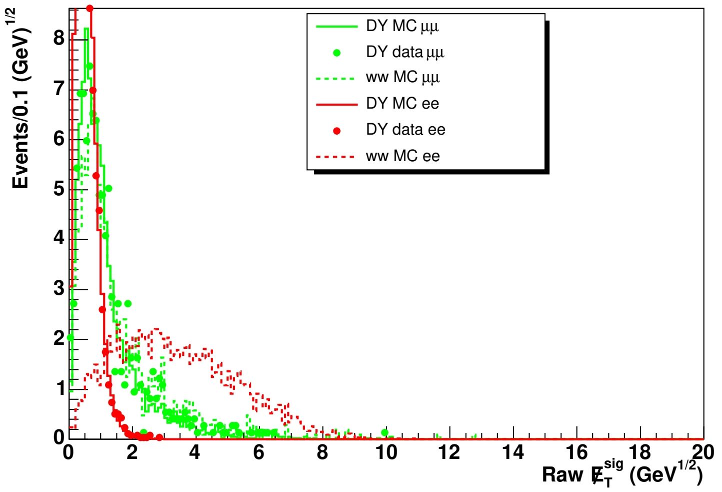

Figure 6.4: Raw $\not\!\!E_T^{sig}$ of signal and background events in the Z window with 2 isolated baseline leptons. No other cuts applied.

$\not\!\!E_T^{sig}$ distributions are shown in Figure 6.6.

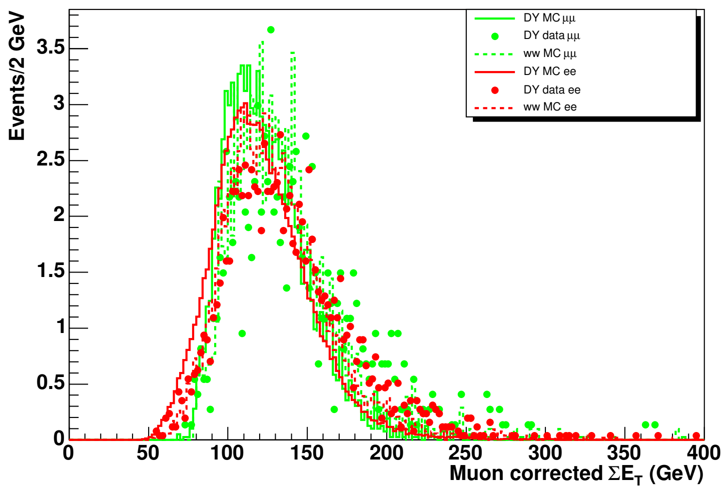

Figure 6.5: Muon corrected ΣE_T of signal and background events in the Z window with 2 baseline leptons. No other cuts applied.

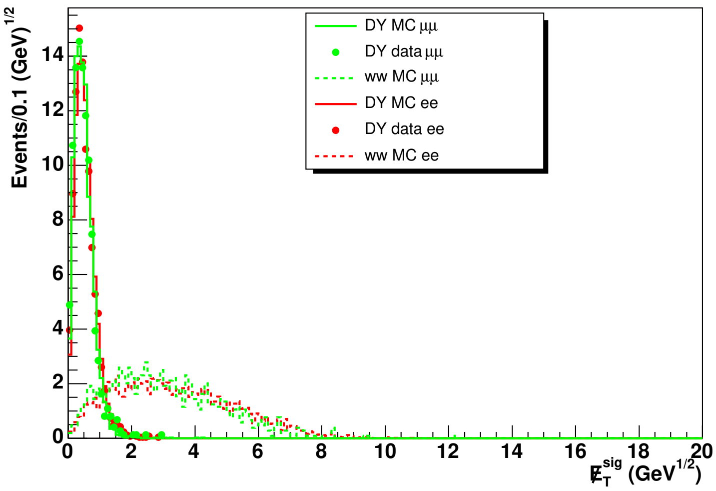

Figure 6.6: Muon corrected $\not\!\!E_T^{sig}$ of signal and background events in the Z window with 2 baseline leptons. No other cuts applied.

Effect Of Remaining Selection Cuts

Applying the remaining cuts of the $WW \rightarrow \bar{l}\nu l\bar{\nu}$ selection to the distributions shown in the previous figures shows that the signal and background separation remains and no obvious distortion of the distributions has occurred through applying these additional kinematic requirements (See Figure 6.8 and Figure 6.7).

Agreement between Data and Monte Carlo

There are some differences seen in the Monte Carlo and data distributions of ΣE_T (See Figure 6.5). This difference has been investigated [46] and is found to be due to the presence of multiple interactions in the data (removing events with more than 1 vertex reduces the difference between MC and data) and the mis-modelling of the boson P_T spectrum in the Monte Carlo. The effect of the difference is small due to the veto on jet activity and is discussed further in the section on systematic errors in Sections 7.4.7 and 8.1.1.

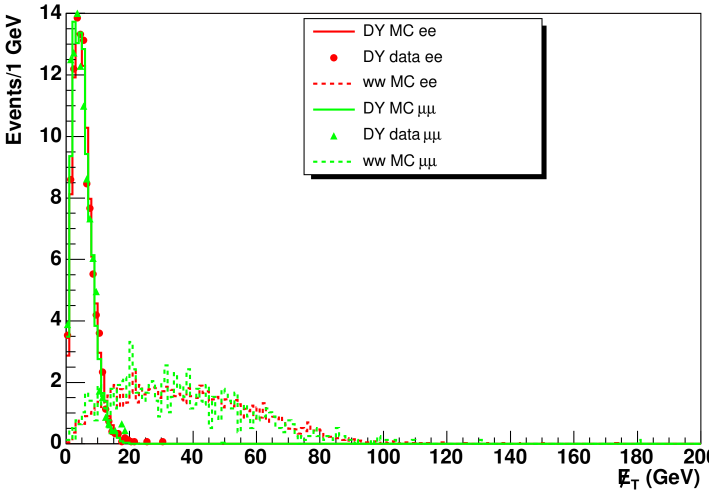

Figure 6.7: $\not\!\!E_T$ of Z window signal and background events with remaining WW event selection cuts applied.

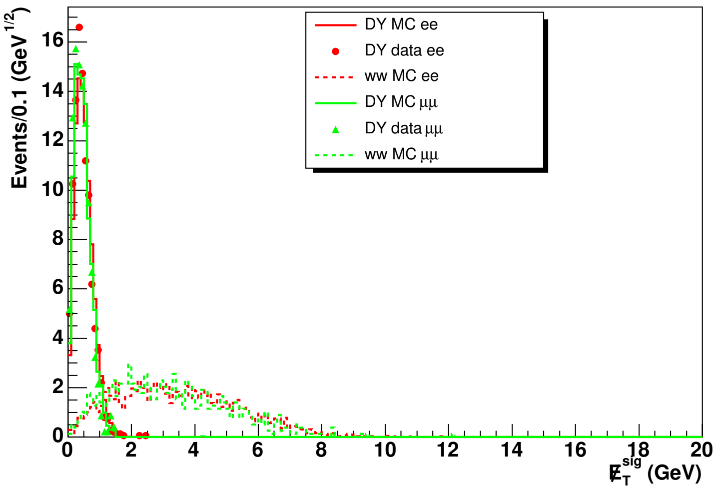

Figure 6.8: $\not\!\!E_T^{sig}$ of Z window signal and background events with remaining WW event selection cuts applied.

6.3.1 Drell-Yan Background Rejection Methods

The effect of different cuts that use the separation in the $\not\!\!E_T$ and $\not\!\!E_T^{sig}$ distributions shown in the previous section is investigated by taking a signal WW Monte Carlo sample and a Drell-Yan Monte Carlo sample and applying the whole $WW \to \bar{l}\nu l\bar{\nu}$ selection and then varying the selection cuts in the Z window $76 < M_{l\bar{l}} < 106$ GeV (see table 6.1).

The number of events surviving the selection and $\frac{S}{\sqrt{B}}$ are used as figures of merit by which to judge the effectiveness of these cuts, where S is the expected number of signal events and B is the expected number of Drell-Yan $Z/\gamma^{*}\to ee, \mu\mu$ background events. In both cases the event numbers are normalised to 126 pb^{-1} to allow them to be compared to a data subset.

In all plots shown in the following sections, the errors on $\frac{S}{\sqrt{B}}$ are of order 40%. This is because of low statistics in the background samples. Typically there are 10 events after the signal selection criteria on which to base a background estimate.

Drell-Yan Rejection with $\not\!\!E_T$

Figure 6.9 shows the $\frac{S}{\sqrt{B}}$ at 126 pb^{-1} for the whole $WW \to e\nu e\nu$ selection versus the $\not\!\!E_T$ cut applied to Z window events. The best cut is taken to be at 35 GeV. The resulting event yields are shown in Table 6.2 .

Drell-Yan Rejection with Muon Corrected $\not\!\!E_T$ Significance

Figures 6.10(a) and 6.10(b) show the $\frac{S}{\sqrt{B}}$ at 126pb^{-1} for the whole $WW \to \bar{l}\nu l\bar{\nu}$ selection versus the $\not\!\!E_T^{sig}$ cut applied to signal and background Monte Carlo events in the Z window. Again, low statistics in the background (5 events) make it difficult to interpret this curve. A cut at 3.0 is taken as the best on this evidence and the resulting event yields are shown in Table 6.2.

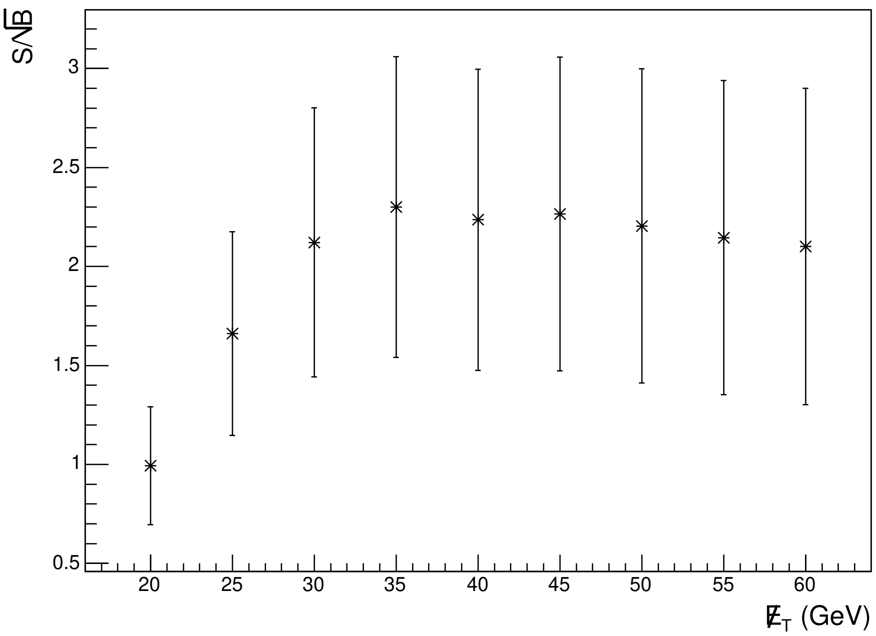

Figure 6.9: $\frac{S}{\sqrt{B}}$ of $WW \to e\nu e\nu$ event selection as a function of the $\not\!\!E_T$ applied to Z window events.

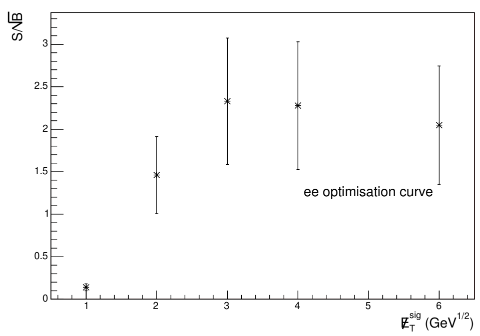

(a) electron-electron channel

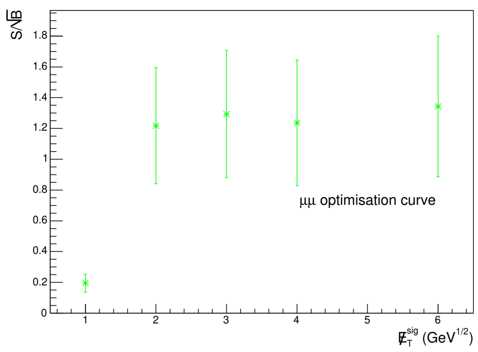

(b) $\mu\mu$ channel

Figure 6.10: $\frac{S}{\sqrt{B}}$ for $\not\!\!E_T^{sig}$ recovery of ee and $\mu\mu$ Z window WW events.

Drell-Yan Rejection with both $\not\!\!E_T$ and $\not\!\!E_T^{sig}$

It is possible that a combination of these cuts could result in a further improved signal acceptance and/or background rejection. Figures 6.11(a) and 6.11(b) show the correlation of $\not\!\!E_T$ with $\not\!\!E_T^{sig}$ of events with 2 good leptons in the Z window. The data is shown in Figures 6.12(b) and 6.12(a). It can be seen here that the flat cut in $\not\!\!E_T^{sig}$ will not be greatly improved by adding a $\not\!\!E_T$ cut since the background is very well contained in the low $\not\!\!E_T^{sig}$ region. The optimisation plane is shown in Figures 6.13(a) and 6.13(b) and the best cut is taken to be: $\not\!\!E_T > 25$GeV and $\not\!\!E_T^{sig}$ >3.0 GeV$^{1/2}$. This results in exactly the same event yields as with the $\not\!\!E_T^{sig}$ cut alone. See Table 6.2 for a complete comparison of these cuts.

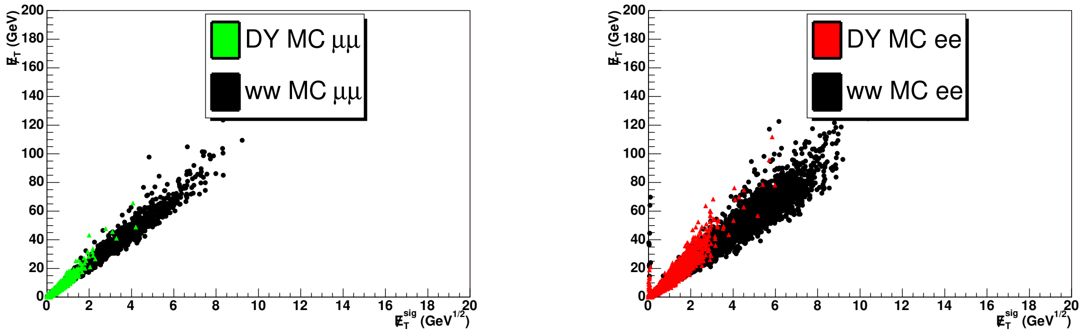

(a) $\mu\mu$ channel

(b) ee channel

Figure 6.11: $\not\!\!E_T$ versus $\not\!\!E_T^{sig}$ of signal and background events in the Z window with 2 isolated baseline leptons. No other WW cuts are applied.

6.3.2 Drell-Yan Rejection Summary

The resulting cut strategies are summarised in Table 6.2. All demonstrate a similar performance and give obvious improvement over a simple veto method, but there is little to choose between them. The combination cut of $\not\!\!E_T$>25 GeV and $\not\!\!E_T^{sig}$ >3.0 GeV$^{1/2}$ is chosen. This gives an event selection with a constant $\not\!\!E_T$ cut with which to select the signal and an additional requirement in the Z mass window of $\not\!\!E_T^{sig} > 3.0$ GeV$^{1/2}$ to remove the background.

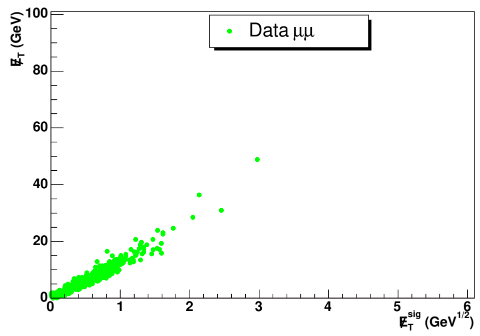

(a) $\mu\mu$ channel

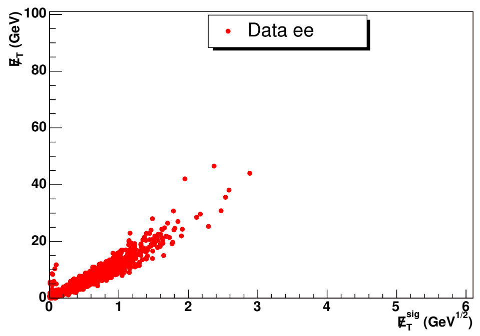

(b) ee channel

Figure 6.12: $\not{E}_T$ versus $\not{E}_T^{sig}$ of Z window data events .

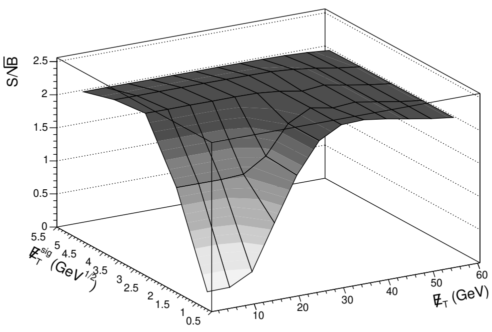

(a) ee channel

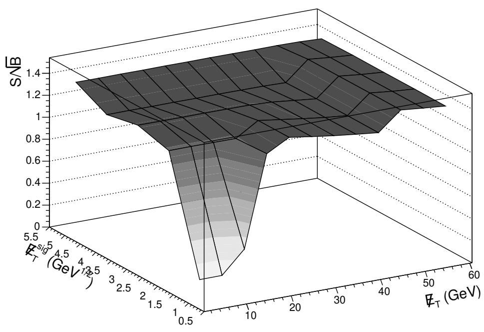

(b) $\mu\mu$ channel

Figure 6.13: $\frac{S}{\sqrt{B}}$ for $\not{E}_T$ versus $\not{E}_T^{sig}$ of $\mu\mu$ signal and background events in the Z window with 2 isolated baseline leptons. No other WW cuts are applied.

This final proposed selection results in the recovery of $80.2 \pm 3.2\%$ of the events that would be lost with a simple Z mass veto whilst continuing to reject a very large fraction of the Drell-Yan background.

Cuts outside Z window						
	2 iso-baseline leptons	$\not\!\!E_T > 25$		$\Delta\phi$ (l,$\not\!\!E_T$) > 20° if $\not\!\!E_T$ <50 GeV	Jet Veto	opp sign
Cuts inside Z window						
strategy 0	veto all events in Z window					
strategy 1	2 iso-baseline leptons	$\not\!\!E_T > 35$		$\Delta\phi$ (l,$\not\!\!E_T$) > 20° if $\not\!\!E_T$<50 GeV	Jet Veto	opp sign
strategy 2	2 iso-baseline leptons		$\not\!\!E_T^{sig} > 3$	$\Delta\phi$ (l,$\not\!\!E_T$) > 20° if $\not\!\!E_T$<50 GeV	Jet Veto	opp sign
strategy 3	2 iso-baseline leptons	$\not\!\!E_T > 25$	$\not\!\!E_T^{sig} > 3$	$\Delta\phi$ (l,$\not\!\!E_T$) > 20° if $\not\!\!E_T$<50 GeV	Jet Veto	opp sign

Table 6.1: Drell-Yan rejection strategies.

Cut on Z window events (all other cuts applied)	Electron Channel			
	WW Evts	DY Evts	S/B	S/$\sqrt{\text{B}}$
Veto	$1.59 \pm 0.02(8769)$	$0.66 \pm 0.20(11)$	2.40 ± 0.86	1.96 ± 0.72
$\not\!\!E_T$>35	$1.95 \pm 0.02(10787)$	$0.72 \pm 0.21(12)$	2.70 ± 0.89	2.30 ± 0.84
$\not\!\!E_T^{sig}$ >3	$1.98 \pm 0.02(10923)$	$0.72 \pm 0.21(12)$	2.73 ± 0.89	2.33 ± 0.84
$\not\!\!E_T$>25 + $\not\!\!E_T^{sig}$ >3	$1.98 \pm 0.02(10923)$	$0.72 \pm 0.21(12)$	2.73 ± 0.89	2.33 ± 0.84
Cut on Z window events (all other cuts applied)	**Muon Channel**			
	WW Evts	DY Evts	s/b	S/$\sqrt{\text{B}}$
Veto	$0.90 \pm 0.02(6497)$	$0.46 \pm 0.10(3)$	1.95 ± 0.67	1.34 ± 0.46
$\not\!\!E_T$>35	$1.01 \pm 0.02(7308)$	$0.62 \pm 0.12(4)$	1.63 ± 0.56	1.28 ± 0.56
$\not\!\!E_T^{sig}$ >3	$1.02 \pm 0.02(7354)$	$0.62 \pm 0.12(4)$	1.65 ± 0.57	1.30 ± 0.56
$\not\!\!E_T$>25 + $\not\!\!E_T^{sig}$ >3	$1.02 \pm 0.02(7354)$	$0.62 \pm 0.12(4)$	1.65 ± 0.57	1.30 ± 0.56

Table 6.2: Expected event yields with integrated luminosity L=126pb^{-1} of data with various methods to reject Z Window events. (Raw event numbers in parenthesis)

6.4 Event Selection Summary

With this additional requirement to suppress the Drell-Yan background, the event selection is finalised and is shown in full in Table 6.3. Having finalised the event selection, it is possible to estimate the expected signal and expected background by running the selection over Monte Carlo samples and to search the data itself for $WW \rightarrow \bar{l}\nu l\bar{\nu}$ candidates. These are discussed in the following three chapters.

	Event Selection
1	2 isolated leptons
2	$\not{E}_T > 25$ GeV
3	$\not{E}_T^{sig} > 3$ if $76 < M_{ee,\mu\mu} < 106$
4	$\Delta\phi(\not{E}_T, \text{nearest } l \text{ or } j) > 20^\circ$ if $\not{E}_T < 50$ GeV
5	No jets with $E_T^{\text{corr}} > 15$ GeV, $\mid \eta \mid < 2.5$
6	opposite charge leptons

Table 6.3: WW dilepton event selection cuts.

Chapter 7

$WW \rightarrow l\bar{\nu}\bar{l}\nu$ Acceptance

The probability of $WW \rightarrow l\bar{\nu}\bar{l}\nu$ events passing the event selection needs to be estimated so that the number of events that are generated for a given integrated luminosity can be translated into the number of events that are expected to be observed. This relationship is shown in Equation 7.1.

$$N_{WW}^{pred} = A \times \int \mathcal{L} \times \sigma_{WW}^{theory} \tag{7.1}$$

This probability, labelled in Equation 7.1 as A, is comprised of both the geometric acceptance of the event selection and the efficiency ϵ of identifying the leptons etc. Both of which will be detailed in the sections that follow.

7.1 Signal Acceptance

The signal acceptance (A) combined with an initial Monte Carlo estimate of the efficiencies ($(A \times \epsilon)_{MC}$) was evaluated using a PYTHIA MC sample that consisted of 828,000 WW events, where both W bosons were forced to decay leptonically: $W \rightarrow l\nu$; $l = e, \mu, \tau$. The equivalent WW sample size before any decay requirements is 7.9 million events. Using the best theoretical value for the cross-section averaged over two different PDFs, $\sigma_{NLO}^{WW} = 12.4 \pm 0.8$ pb [47], the luminosity of the sample is estimated to be 636 fb^{-1}, i.e. over 5,000 times the luminosity of the data sample. The efficiency of the event selection cuts is shown in Table 7.1

	WW					
	ee		$\mu\mu$		$e\mu$	
Cut		%		%		%
Lepton ID	23800.00		22665.0		44486.00	
Isolation	21407.00	89.95±0.19	20858.0	92.03±0.18	40574.00	91.21±0.13
Conv+Cosmic	21003.00	98.11±0.09	20858.0	100.00±0.00	40169.00	99.00±0.05
Z-veto	18531.00	88.23±0.22	18221.0	87.36±0.23	40169.00	100.00±0.00
$\not\!\!E_T$ >25 GeV :	14478.00	78.13±0.30	14161.0	77.72±0.31	29077.00	72.39±0.22
$\Delta\phi > 20^\circ$ if $\not\!\!E_T$ <50	13986.00	96.60±0.15	13644.0	96.35±0.16	27970.00	96.19±0.11
0 jets	11214.00	80.18±0.34	10930.0	80.11±0.34	22604.00	80.82±0.24
Opposite Sign	10334.51	92.16±0.25	10930.0	100.00±0.00	21725.03	96.11±0.13
Total Selection Eff	43.42%		48.22%		48.84%	

Table 7.1: PYTHIA WW events passing the WW analysis cuts for each dilepton category and the associated selection efficiencies. Efficiencies are relative to the previous row. Errors are statistical only.

From the surviving number of events the raw acceptance is calculated simply as:

$$A_{lep}^{raw} = \frac{N_{Passed}}{N_{Generated}} A^{raw} = A_{lep}^{raw} \times (3 \times BR(W \to l\nu))^2 \quad (7.2)$$

and has the $W \to l\nu$ branching ratio included to give the raw acceptance as a fraction of $p\bar{p} \to WW$ events generated. The resulting numbers for each dilepton category are shown in Table 7.2. The final Acceptance numbers are then the combination of the raw Acceptance, the efficiency corrections ϵ_{trig} and various scale factors (SF) which will be described later in Table 7.3:

$$A = A^{raw} \times \epsilon_{trig} \times SF$$

.

	A_{ee}	$A_{\mu\mu}$	$A_{e\mu}$	$A_{ee+\mu\mu+e\mu}$
A_{abs}^{raw}	(0.137 ± 0.001) %	(0.145 ± 0.001) %	(0.288 ± 0.002) %	(0.570 ± 0.003) %
A_{rel}^{raw}	24.0 %	25.4 %	50.5 %	100.0 %

Table 7.2: The first line shows the absolute values of the raw acceptances and the second line the relative acceptances in the ee, $\mu\mu$ and $e\mu$ channels. These numbers use a BR($W \to l\nu$) of 0.1068 [58].

7.2 Trigger Efficiencies And Efficiency Corrections

The acceptance now has to be modified for additional efficiencies such as the trigger efficiency and various differences between the Monte Carlo and the data; e.g. the cut on the event vertex position. Each of these is discussed below and then summarised in Table 7.3 at the end.

7.2.1 Trigger Efficiencies

Trigger efficiencies are the probabilities that an event with the appropriate kinematics will actually pass the trigger requirements. The efficiencies for events to be accepted by the triggers are measured in samples that contain the trigger object but were collected by "backup" triggers that made no requirement on that object. For example the efficiency of the track requirements that make up part of the high-p_T electron trigger path are measured using electron events collected by the "W-NO TRACK" trigger which makes no requirement on the tracks.

All of the triggers used in this analysis, except the MET_PEM trigger discussed below, have been studied in detail elsewhere and the results are summarised in Table 7.3.

	Value	Reference
Trigger Efficiency		
ϵ_{CEM}	0.961	[28]
ϵ_{CMUP}	0.887	[29]
ϵ_{CMX}	0.954	[29]
$\epsilon_{MET\_PEM}(PHX - electron)$	0.961	this thesis
$\epsilon_{MET\_PEM}(PHX - \mu)$	0.942	this thesis
Data/MC Reconstruction Efficiency		
F_{CEM}	0.965	[41]
F_{PHX}	0.927	[43]
F_{CMU}	0.890	[29]
F_{CMP}	0.943	[29]
F_{CMUP}	0.887	[29]
F_{CMX}	1.008	[29]
F_{CMIO}	1.000	[49]
Data/MC $\|z0\| < 60$ cm Efficiency		
F_{z0}	0.977	[50]

Table 7.3: The scale factors applied to Monte Carlo expectations for the trigger efficiencies and the lepton ID efficiencies.

MET_PEM

Forward electron triggered events are collected on the MET_PEM trigger path described earlier in Section 4.1.1. At Level 1 the trigger requires $\not{E}_T > 15$ GeV and $E_T^{EM} > 8$ GeV, at level 2 it requires $E_T^{EM} > 20$ and at level 3 $\not{E}_T > 15$ GeV and $E_T^{EM} > 20$ GeV. Certain dilepton categories that contain forward electrons such as Phoenix-CMIO and Phoenix-Phoenix can only be collected on this trigger. There are two main sources of inefficiency: the $\not{E}_T$ requirement at Level 1 and the PEM requirements at Level 2.

The efficiency of the Level 1 $\not{E}_T$ requirement has been estimated in the $W \to e\nu$ forward electron analysis described in [48] and found to be very close to 100%. The inefficiency in $WW \to l\bar{\nu}\bar{l}\nu$ events will be even lower due to the raised $\not{E}_T$

cut of 25 GeV applied here, compared to just 20 GeV used in that analysis. By comparing Monte Carlo samples of $W \to e\nu$ and $WW \to l\bar{\nu}\bar{l}\nu$ it is observed that the trigger efficiency would be 100% for the Pheonix categories, were it not for the use of muon corrected $\not\!\!E_T$ in the offline analysis, which is less well correlated with the raw $\not\!\!E_T$ used during triggering. The Pheonix-μ categories therefore have some inefficiency. Using Monte Carlo, a 2% residual inefficiency is expected due to event topologies that result in much smaller raw $\not\!\!E_T$ compared to muon corrected $\not\!\!E_T$.

The level 2 PEM requirements are also estimated in [48] and found to be 96.6% efficient. Monte Carlo studies show that the E_T spectrum of plug electrons in $W \to e\nu$ events is not the same as the spectrum in WW pair production. Using the trigger turn-on parameterisation in [48] indicates that the difference in efficiency between the these two processes is, however, only around 0.5%; resulting in an efficiency of 96.1% for this analysis.

Using these number the overall trigger efficiencies for the MET_PEM trigger are found to be:

$$\epsilon_{MET\_PEM}(PHX - electron) = \epsilon_{L1} \times \epsilon_{L2} = 1.00 \times 0.961 = 0.961$$

$$\epsilon_{MET\_PEM}(PHX - \mu) = \epsilon_{L1} \times \epsilon_{L2} = 0.98 \times 0.961 = 0.942$$

The systematic uncertainty on the trigger efficiencies is also estimated in [48] and found to be 2%. Given the differences between $W \to e\nu$ and $WW \to l\bar{\nu}\bar{l}\nu$ event kinematics a similar uncertainty could arise due to those differences that would not be covered completely by the Monte Carlo methods used above and therefore a 3% systematic uncertainty on the above efficiencies is assigned.

7.2.2 Lepton ID Efficiency Corrections

The lepton ID cuts used in this analysis are standard cuts defined by the CDF electroweak analysis group and so the efficiencies of these selections have been measured elsewhere, as have the differences between data and Monte Carlo. These data/Monte Carlo corrections and their references are given in Table 7.3, while the efficiencies themselves were noted in the appropriate sections of Chapter 5.

In addition to these trigger and ID efficiency corrections, there are certain other effects that need to be accounted for, such as the charge identification of the Phoenix tracking algorithm and the track isolation cut, since they are not part of these CDF standard efficiencies. These are discussed in the following sections.

Forward Electrons

An η dependent scale factor is calculated to compensate for the discrepancy between the Monte Carlo and data in describing the frequency of Phoenix electrons obtaining the incorrect charge assignment, known as the charge fake rate, that results in an inefficiency due to the opposite sign cut applied in the event selection.

This scale factor is applied to the Monte Carlo acceptances to account for the over-estimate. The charge ID rate is calculated in central-plug $Z \rightarrow ee$ events in both Monte Carlo and data, where the charge ID is defined as the number of events with 2 oppositely charged leptons(OS)divided by OS + same-sign(SS) events ($OS/(SS + OS)$). This distribution is shown in Figure 7.1(b) and the resulting scale factor is shown in Figure 7.2.

Since there is a significant difference between the η distributions of plug electrons in these WW and Drell-Yan events with one central and one plug electron (see Figure 7.1(a)), the scale factor cannot be applied as an average, so is instead applied as a function of η. A linear fit is applied to each side of the scale factor distribution and these functions (shown in Table 7.4) are used to correct the Monte Carlo estimates.

	a	b
$+\eta$	1.049	-0.0071
$-\eta$	1.069	0.0093

Table 7.4: The values of the fit, $a + b\eta$ of the Phoenix charge ID data/MC scale factor. No significant P_T dependence was observed [48]

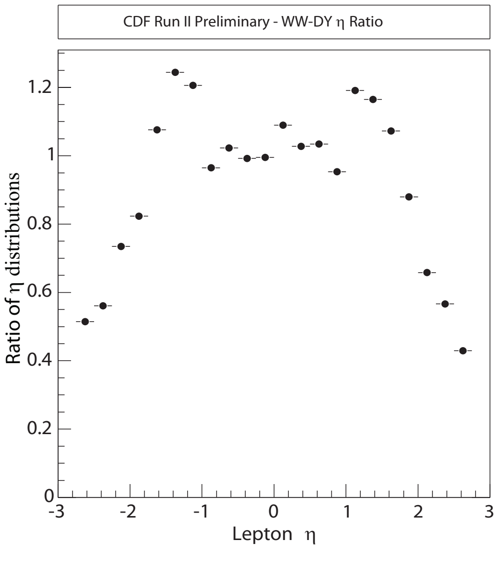

(a) The ratio of the η distributions for WW and DY MC

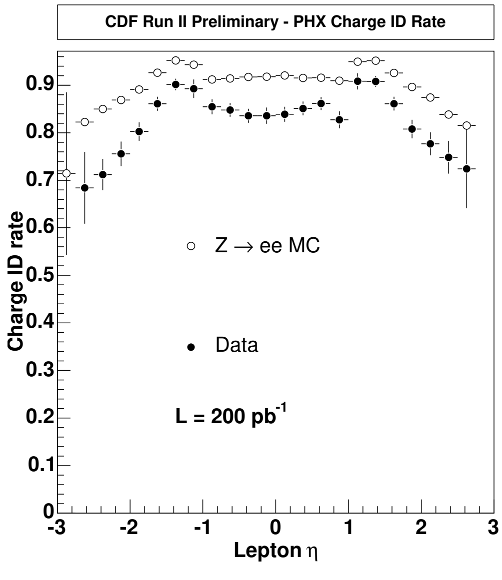

(b) The Phoenix charge ID rate as a function of η for both $Z \to ee$ MC and data.

Figure 7.1: Charge mis-ID studies for Phoenix tracking

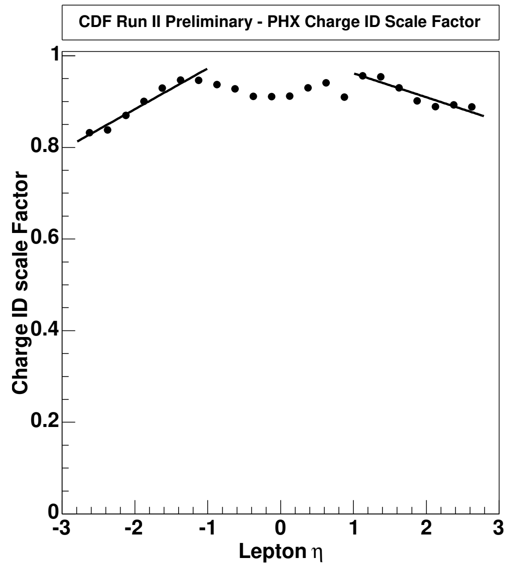

Figure 7.2: Result of the fit to the data/MC Phoenix charge scale factor ratio, used to determine the η dependent scale factor for Phoenix electrons.

Track Isolation Requirement

The track isolation requirement used in this analysis is not a standard CDF requirement and so is not included in the lepton ID efficiencies discussed earlier. The efficiency of this cut was examined with WW Monte Carlo and found to be 97% efficient. Any potential mis-modelling of this quantity in the Monte Carlo was estimated by comparing Z yields with and without track isolation and found to be consistent with 1.0 for all lepton categories for which it is applied. A systematic error is assigned in section 7.4.6 to cover all observed variations in this efficiency modelling.

7.2.3 Luminosity Correction

The luminosity measured by the CLC includes the whole luminous region of the detector, but the analysis uses a vertex cut of $|z0| < 60$ cm to ensure well measured event properties. The efficiency of this cut is measured in data collected on a minimum-bias trigger and is found to be 95.0±0.1% [50]. This is applied to the luminosity measured by the CLC to obtain a corrected luminosity for the data sample used in this analysis. And a scale factor is applied to the Monte Carlo estimates to account for the difference in this efficiency between data and Monte Carlo (see Table 7.3).

7.3 Final Acceptance

The final Acceptance numbers are then the combination of the raw Acceptance and the efficiency corrections: $A = A^{raw} \times \epsilon_{trig} \times SF$, and are detailed in Table 7.5.

	A_{ee}	$A_{\mu\mu}$	$A_{e\mu}$	$A_{ee+\mu\mu+e\mu}$
A^{raw}_{abs}	(0.137 ± 0.001) %	(0.145 ± 0.001) %	(0.288 ± 0.002) %	(0.570 ± 0.003) %
A^{raw}_{rel}	24.0 %	25.4 %	50.5 %	100.0 %
A_{abs}	(0.119 ± 0.001) %	(0.113 ± 0.001) %	(0.233 ± 0.002) %	(0.464 ± 0.002) %
A_{rel}	25.6 %	24.3 %	50.2 %	100.0 %

Table 7.5: As before: the absolute and relative acceptances in the ee, $\mu\mu$ and $e\mu$ channels use a BR($W \rightarrow l\nu$) of 0.1068. The upper rows show the raw acceptance and efficiencies. The lower rows show the final acceptance with trigger efficiencies and scale factors included

7.4 Systematic Uncertainties On The Signal Acceptance

There are many sources that contribute to the uncertainty on the measured acceptance. In the sections that follow each of these sources is varied in turn and the observed change in acceptance is used to estimate the size of the associated error.

7.4.1 Jet Veto Uncertainty ("ISR")

Using the LO generator PYTHIA to measure the acceptance presents a well known problem; namely that leading order generators do not accurately reproduce the fraction of events with 0 jets (with $|\eta| < 2.5$ and $E_T > 15$ GeV) or 1 jet etc , since they do not model the QCD radiation well enough. Due to the jet veto applied in this analysis there is a significant sensitivity to this mis-modelling of the jet fractions and it is expected to be the largest single source of uncertainty on the acceptance estimate.

The size of any underestimate is calculated by a combination of data and Monte Carlo samples generated by the NLO WW generator MC@NLO.

The 0-jet fraction of WW events in PYTHIA Monte Carlo is consistently lower than that of MC@NLO over a wide range of masses. The averaged PYTHIA/MC@NLO ratio is 0.955 ± 0.010. This is consistent with a comparison based on data [53]. A ratio of 0.955 ± 0.009 is obtained when PYTHIA generated $Z \to ee$ Monte Carlo is compared to data. Thus a 0.955 scale factor is applied to the PYTHIA WW acceptance to account for the overestimate of the 0-jet fraction of events.

However, there is an overall difference of 6% between the 0-jet fraction of WW events compared to Drell-Yan events arising from the fact that QCD radiation is not completely process independent and that there is a different $\hat{s}$ dependence between Z and WW production. This is used as an estimate of the systematic error on the WW acceptance due to QCD corrections to the 0-jet fraction.

7.4.2 Generator

Systematic effects due to the choice of generator are estimated by comparing WW acceptances from samples generated by ALPGEN+HERWIG to the central

PYTHIA acceptance value. HERWIG has a different parton showering model to PYTHIA and so gives rise to differences in the isolation variables, particle multiplicity and therefore event selection efficiencies. The overall difference between the two samples is 6.3%. This difference is not all due to the different parton showering models however; there is a significant contribution from differences in the branching ratios used for the leptons. By analysing the samples at the generator level it is seen that PYTHIA uses same BR for all lepton types, but ALPGEN+HERWIG uses different values for each lepton which are all different to PYTHIA's values. This branching ratio difference needs to be factored out in order to derive a systematic error due to QCD and event modelling differences. The individual acceptances in each dilepton channel are renormalised by folding in the assumed branching ratio and then ratios between the two samples are independent of the these branching ratio differences. Averaging over the different dilepton channels then gives a 4% difference between the PYTHIA and HERWIG samples, which is taken as the systematic error due to the generator.

7.4.3 PDF Uncertainty

There are two associated systematic effects due to PDFs. The first is the PDF and QCD factorisation scale systematic effects on the theoretical cross-section and the second a direct effect on the $WW \rightarrow l\bar{\nu}\bar{l}\nu$ acceptance due to PDF uncertainties.

Cross-Section Systematic Effects

The effect of the PDF choice and QCD factorisation scale choice on the theoretical cross-section results in an uncertainty on the WW yield only, not the WW acceptance.

The effect of the chosen QCD scale is explored in Table 7.6. The error due to the PDF choice is estimated by first calculating the NLO WW cross-section at $\sqrt{s} = 2$ TeV using MCFM and the CTEQ6 LHAPDF and then using the Hessian method [57] to calculate the uncertainty. 40 member PDFs of the CTEQ6 family are used, giving a resultant uncertainty on the central cross-section value, $\sigma_0 = 12.4$ pb, of:

$$(\sigma_0 - \delta_{\sigma-}, \sigma_0 + \delta_{\sigma+}) = \sigma_0(1 - 3.9\%, 1 + 4.6\%)$$

where the $\delta_{\sigma\pm}$ are the quadratic sum of the variations of σ due to the 40 different PDFs. i.e. $(\delta_{\sigma\pm})^2 = \sum_1^{40}(\sigma_i - \sigma_0)^2$.

The resulting largest combined variation in the theoretical cross-section due to choice of QCD scale and PDF is 6%

Q^2	σ (pb)	$\frac{\sigma(Q^2)-\sigma(M_W^2)}{\sigma(M_W^2)}$ (%)
$(M_W)^2$	12.4	
$(\frac{M_W}{2})^2$	13.0	4.6
$(2M_W)^2$	11.9	-4.4

Table 7.6: QCD scale dependence of the total cross-section for $p\bar{p} \rightarrow W^+W^-$

Acceptance Systematic Effects

Direct systematic effects on the acceptance due to varying the PDF are estimated by running MCFM in LO using NLO PDF CTEQ6 and applying a simplified event selection of $P_T \geq 20$ GeV, $\not\!\!E_T \geq 25$ GeV and $\eta \leq 1$ over the generated events. Changes in this acceptance are then noted as the choice of PDF is varied. The largest change is $\approx 1\%$ and this is consequently included into the total acceptance systematic.

7.4.4 Jet Energy Scale

Systematic errors on the jet energy corrections [40] are complicated and display a strong P_T and η dependence.

- The correction to the η response of the calorimeter is derived from dijet balancing and shows some considerable systematic differences across the different systems, the biggest being in the plug region. The systematic error, assigned as a function of η, is around 0.2% in the central region to 7% in the plug.

- The correction for multiple interactions is parameterised according to the number of vertices in the event, but shows some systematic differences between different samples and cone sizes used to make the correction and also a systematic dependence on the instantaneous luminosity. A 7% error covers differences between the Z,W and jet data samples and the largest variation due to the luminosities is 10%. Giving a total 15% error on the scale.

- The absolute jet energy scale correction takes account of any un-instrumented regions and non-linearity in the central calorimeter response. The largest systematic error observed is found when varying the calorimeters' response to individual particles and gives a total 3% systematic error.

- Fragmentation and underlying event corrections have systematic errors with very strong P_T dependence, becoming as large as 10% at low jet P_T.

Taking all these errors on the jet energy scale in quadrature to give a total systematic error, σ_{jet} that is a function of both P_T and η and applying a $\pm 1\sigma_{jet}$

variation to the signal sample on a jet by jet basis changes the total $WW \to l\bar{\nu}\bar{l}\nu$ acceptance by 3% due to the jet veto cut.

7.4.5 Lepton ID

The systematic errors on most lepton ID efficiencies are typically around 1%(see [41] and [29]). The exception is that of the forward electrons where the error is conservatively estimated to be several %. Since this only applies to around 25% of the expected WW events, the overall error is taken as 2%.

7.4.6 Track Isolation

Estimating the efficiency correction between Monte Carlo and data of the track isolation requirement found it to be consistent with 1.0 as discussed earlier(section 7.2.2) and also showed no obvious systematic effects. The largest variation across dilepton categories was 4% so this is taken as the systematic error.

7.4.7 $\not{E}_T^{sig}$ Uncertainty

The $\not{E}_T^{sig}$ distribution is well modelled in single Z production, but much less well modelled in single W production. Most of this mis-modelling is due to much poorer ΣE_T modelling. Since WW production has properties similar with both; two high-P_T charged leptons as in single Z production but real $\not{E}_T$ as in single W production, it is assumed that WW will be somewhere between the two. The error on single W is taken as a conservative estimate of the systematic effect of $\not{E}_T^{sig}$ mis-modelling on the WW signal. The difference in efficiency of the $\not{E}_T^{sig}$ =3.0 cut between single W data and Monte Carlo is calculated as the number of jets in the event is varied from 0 to 2. The largest variation observed is 10%.

This error only applies to that portion of the WW acceptance for which the $\not{E}_T^{sig}$ cut is applied, which is 15%, giving a total 2% error from this source.

7.4.8 Trigger Uncertainty

Most trigger efficiency uncertainties are ≤1% (see [28] and [29]). MET_PEM is by far the largest and was estimated earlier in Section 7.2.1 and found to be 3%. Since only 10% of events rely on the MET_PEM trigger, the overall error due to the trigger efficiency uncertainty is reduced to ≈1% .

7.4.9 Combined Systematic

Taking each of these errors and adding them in quadrature gives a total acceptance systematic of 10% which is assumed to be correlated across all dilepton channels. Table 7.7 gives a summary of all of the systematic errors that comprise this 10%.

Source	Systematic Error
Jet Veto (“ISR”)	6%
Generator/Parton-Shower Model	5%
PDF/QCD-Scale	5%
PDF Acceptance	1%
Jet Energy Scale	3%
Lepton ID	2%
Track Isolation	4%
Trigger Efficiency	1%
$\not{E}_T^{sig}$	2%
Combined	10%

Table 7.7: Sources of systematic uncertainty on the $WW \rightarrow l^+l^-\nu\bar{\nu}$ acceptance. The PDF/QCD-Scale systematic is included here from the studies described in 7.4.3, but does not contribute to the systematic on the acceptance. It is included in the systematic on the expected WW yield.

7.5 Signal Expectation

With the total acceptance and all scale factors determined the final signal expectation N_{WW}^{pred} is estimated from the number of events that survived the event selection in Table 7.1. The resulting predictions in each dilepton channel are shown in Table 7.5.

	CDF Run II Preliminary			
Source	ee	$\mu\mu$	$e\mu$	$\ell\ell$
$WW \rightarrow$ dileptons	2.61 ± 0.31	2.48 ± 0.29	5.11 ± 0.60	10.20 ± 1.19

Table 7.8: Final $WW \rightarrow l\bar{\nu}\bar{l}\nu$ event expectations in 184 pb^{-1}. Errors are statistical and systematic combined.

Chapter 8

Backgrounds

Backgrounds to WW dilepton production are dominated by mis-reconstructed events that mimic the WW signal by faking either the leptons or the $\not{E}_T$, with some additional background from other physics processes that overlap in phase space and final states. This chapter provides a description of each of these backgrounds, explaining why they are backgrounds, how they are minimised and how they are estimated.

8.1 Estimating The $Z/\gamma^* \rightarrow l\bar{l}$ Background

A discussion of how Drell-Yan production constitutes a background to $WW \rightarrow l\bar{\nu}\bar{l}\nu$ and how it is minimised was presented in Chapter 6. In this section an estimate of the remaining background from this source is presented.

It is well known that the Monte Carlo does not model the $\not{E}_T$ distribution of Drell-Yan events very well and since this distribution is the primary variable used to reject Drell-Yan events in this analysis it is possible that a Monte Carlo based estimate of this background could be seriously flawed. One possible solution is to use the data itself to estimate this background where at all possible. This can only be done in the same flavour channels where there is a significant data sample known to be dominated by Drell-Yan production. This is not true for the $e\mu$ dilepton category. The background estimate in that channel is therefore entirely Monte Carlo based. Also, the $Z/\gamma^* \to \tau\tau$ background has real neutrinos and so Monte Carlo is expected to yield be a reliable estimate.

The Drell-Yan background expectation is therefore estimated with a combination of real data and much larger samples of PYTHIA generated Drell-Yan events than used in the previous studies. These samples have 2.85M $\mathrm{Z}/\gamma^* \to \mathrm{ee}$ events, 2.89M $\mathrm{Z}/\gamma^* \to \mu\mu$ events, and 422k $\mathrm{Z}/\gamma^* \to \tau\tau$ events, and a minimum dilepton mass cut of 30 GeV.

As stated above the Drell-Yan background estimate in the $e\mu$ channel is entirely Monte Carlo based. The contribution from $Z/\gamma^* \to \tau\tau$ is discussed shortly, the contribution from $Z/\gamma^* \to ee$ and $Z/\gamma^* \to \mu\mu$ is estimated by simply passing the Monte Carlo samples through the event selection. The results are summarised in Table 8.1 and Table 8.2.

The background from $Z/\gamma^* \to \tau\tau$, which is found to constitute a background in all three measurement channels, is also based on Monte Carlo alone and is summarised in Table 8.3.

Data Estimate of like-flavour Drell-Yan Background

Simply applying the event selection to the like-flavour Drell-Yan data is not possible, since this would result in the selection of the WW signal candidates themselves. So a method to estimate how many like-flavour Drell-Yan data events will fall inside the event selection without applying all of the event selection cuts simultaneously is needed.

Cut	Drell-Yan e^+e^- in the eμ channel #evts	%
Lepton ID	1084.00	
Isolation	805.00	74.26 ± 1.33
Conv+Cosmic	801.00	99.50 ± 0.25
Z-veto	801.00	100.00 ± 0.00
$\not{E}_T$ >25 GeV :	20.00	2.50 ± 0.55
$\Delta\Phi > 20°$ if $\not{E}_T$ <50	7.00	35.00 ± 10.67
0 jets	2.00	28.57 ± 17.07
Opposite Sign	2.00	100.00 ± 0.00
Drell-Yan e^+e^- in 184pb^{-1}	0.05 ± 0.03	

Table 8.1: Raw number of $Z/\gamma^* \to ee$ Monte Carlo events in the $e\mu$ channel surviving each event selection cut and the percentage of events surviving from previous cut. These numbers are scaled to the appropriate luminosity to produce the background estimate in the bottom row and in Table 8.22.

Cut	Drell-Yan $\mu^+\mu^-$ in the eμ channel #evts	%
Lepton ID	1160.00	
Isolation	581.00	50.09 ± 1.47
Conv+Cosmic	542.00	93.29 ± 1.04
Z-veto	542.00	100.00 ± 0.00
$\not{E}_T$ >25 GeV :	80.00	14.76 ± 1.52
$\Delta\Phi > 20°$ if $\not{E}_T$ <50	39.00	48.75 ± 5.59
0 jets	28.00	71.79 ± 7.21
Opposite Sign	17.09	61.03 ± 9.22
Drell-Yan $\mu^+\mu^-$ in 184pb^{-1}	0.28 ± 0.07	

Table 8.2: $Z/\gamma^* \to \mu\mu$ Monte Carlo events in the $e\mu$ channel surviving each event selection cut. These numbers are scaled to the appropriate luminosity to produce the background estimate in the bottom row and in Table 8.22.

To do this it is assumed that the number of events passing all cuts can be estimated by first applying all of the WW selection cuts to the data but with the 'Drell-Yan rejection' cuts reversed to specifically select Drell-Yan events, thereby giving a data sample that looks like WW in most respects but is dominated by Drell-Yan (Figure 8.1(a)). All that is needed then is a way of predicting how many

	Drell-Yan $\tau^+\tau^-$					
	ee		$\mu\mu$		$e\mu$	
Cut		%		%		%
Lepton ID	20623.0		19406		36650.0	
Isolation	18597.0	90.18±0.21	17789	91.67±0.20	33181.0	90.53±0.15
Conv+Cosmic	18336.0	98.60±0.09	17789	100.00±0.00	32912.0	99.19±0.05
Z-veto	17161.0	93.59±0.18	16749	94.15±0.18	32912.0	100.00±0.00
$\not\!\!E_T$ >25 GeV :	787.0	4.59±0.16	816	4.87±0.17	1590.0	4.83±0.12
$\Delta\Phi > 20^\circ$ if $\not\!\!E_T$ <50	293.0	37.23±1.72	324	39.71±1.71	576.0	36.23±1.21
0 jets	42.0	14.33±2.05	44	13.58±1.90	89.0	15.45±1.51
Opposite Sign	38.4	91.43±4.32	44	100.00±0.00	87.5	98.34±1.35
Drell-Yan $\tau^+\tau^-$ in $184pb^{-1}$	0.047 ± 0.01		0.046 ± 0.01		0.099 ± 0.011	

Table 8.3: $Z/\gamma^* \to \tau\tau$ Monte Carlo events surviving each event selection cut. These numbers are scaled to the appropriate luminosity to produce the background estimate in the bottom row and Table 8.22.

of these 'Drell-Yan rich, WW-like' events will fluctuate into the event sample by passing the Drell-Yan rejection cuts. This is calculated by returning to the 'pure' Drell-Yan data (i.e. the inclusive two baseline lepton sample. Figure 8.1(b)) and, with no other cuts, calculating the ratio of the number of events that pass the Drell-Yan rejection cuts to the number of events that fail. Applying this ratio to the number events in the 'Drell-Yan rich, WW-like' sample gives an estimate of the number of Drell-Yan events that fall inside the WW event selection, i.e. the Drell-Yan background (Figure 8.1(c)). Symbolically, this method can be represented by the equation:

$$N(c_1 \wedge c_2 \wedge .... \wedge c_{n-1} \wedge c_n) = N(c_1 \wedge c_2 \wedge .... \wedge c_{n-1} \wedge \neg\, c_n) \times \frac{N(c_n)}{N(\neg\, c_n)}$$

where there are n cuts and N events surviving each cut,c. The $\neg$ symbol refers to the NOT operator and $\wedge$ the AND operator.

The method is summarised in the formula below along with an explicit description of the cuts used to determine each of the inputs. Each of these terms will be discussed in detail in the sections that follow.

The total background estimate is

$$n_{DY}^{tot} = R_{\frac{out}{in}} n_{ww}^{in} + R_{\frac{\hat{DY}}{DY}} \hat{n}_{ww}^{in}$$

where

- $R_{\frac{out}{in}}$ is calculated from Drell-Yan Monte Carlo events that have two baseline leptons, $\not{E}_T > 25 GeV$ and $\Delta\phi(\not{E}_T, \text{nearest } l/j) > 20°$.
- n_{ww}^{in} is the number of data events that have 2 baseline leptons in the Z window with $\not{E}_T < 25$ GeV, opposite sign leptons, $\Delta\phi(\not{E}_T, \text{nearest } l/j) > 20$ and 0 jets minus the expected contamination from other physics processes n_{other}^{mc}.
- $R_{\frac{\hat{DY}}{DY}}$ is calculated from data events that have 2 baseline leptons and counting the number of events that have $\not{E}_T > 25 \wedge \not{E}_T^{sig} > 3$, subtracting the contamination estimated by applying the same cuts to the MC samples for the other physics processes in this region $\hat{n}_{other}^{mc}$, and then dividing by the number of data events that have $\not{E}_T < 25 \vee \not{E}_T^{sig} < 3$. i.e.

$$R_{\frac{\hat{DY}}{DY}} = \frac{n(\not{E}_T > 25 \wedge \not{E}_T^{sig} > 3)^{data} - \hat{n}_{other}^{mc}}{n(\not{E}_T < 25 \vee \not{E}_T^{sig} < 3)^{data}}$$

- $\hat{n}_{ww}^{in}$ is calculated by counting the number of data events with 2 baseline leptons in the Z window with 0 jets, opposite sign leptons, $\Delta\phi(\not{E}_T, \text{nearest } l/j) > 20°$, and $\not{E}_T < 25 \vee \not{E}_T^{sig} < 3$.

There are several issues inherent in this method which will be described in the following sections. The first being that the event selection cuts vary as a function of dilepton mass. Inside the Z window a combination of $\not\!\!E_T$ and $\not\!\!E_T^{sig}$ cuts is used to reject Drell-Yan events but outside the Z window only the $\not\!\!E_T$ cut is applied. The data estimate of this background must therefore be split into two sections and the calculation completed separately for each mass region.

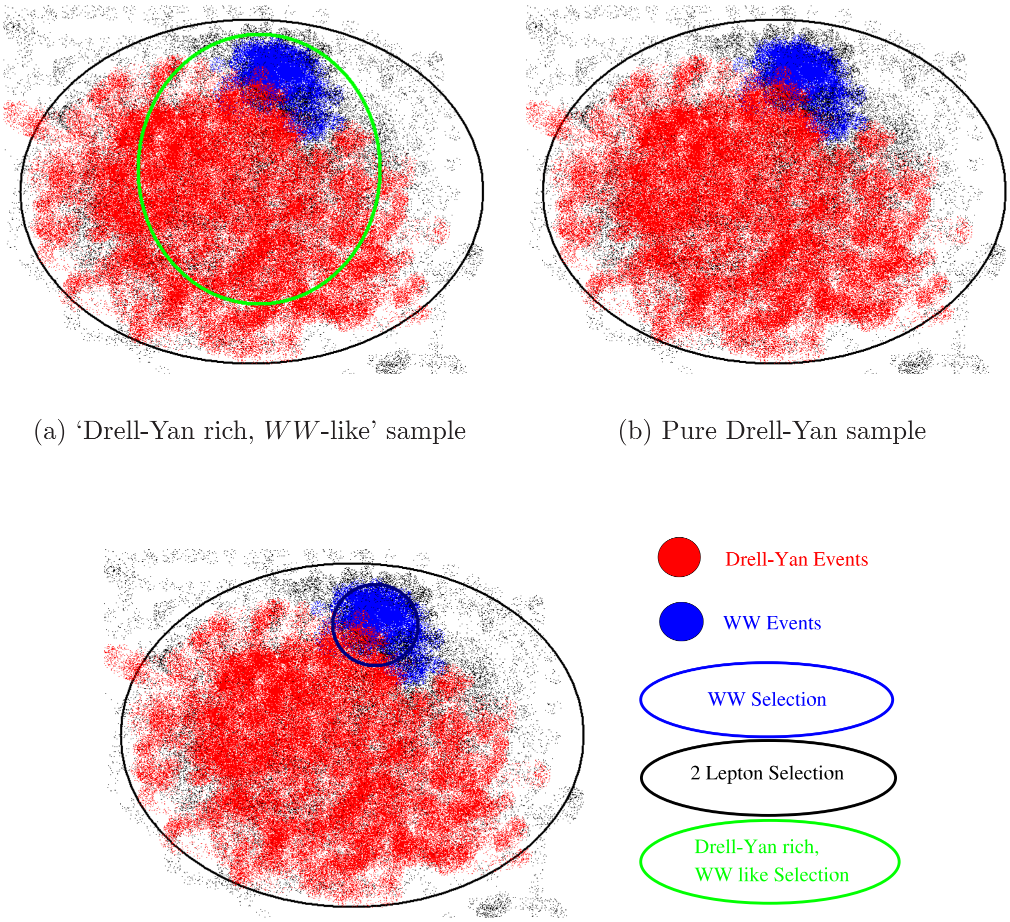

(a) 'Drell-Yan rich, WW-like' sample

(b) Pure Drell-Yan sample

(c) The WW sample

(d) Key

Figure 8.1: Cartoon description of Drell-Yan background prediction using data. The dots represent the data events in an N-dimensional space. The lines represent the selection regions, or event classification. The goal being to estimate the number of Z/γ^* events inside the WW selection region in 8.1(c) by applying the ratio calculated in 8.1(b) to the event count in 8.1(a)

Outside the Z window

The easiest of the two mass regions is the contribution from outside the Z window. Here the Drell-Yan rejection cut is simply the requirement that the events are away from the Z peak. So the 'Drell-Yan rich, WW-like' sample consists of the Drell-Yan data events that fall inside the Z window but pass all of the WW cuts that would be applied outside the Z window (labelled n^{in}_{ww}). To then extrapolate this number of events into the background contribution, all that is needed is simply the ratio of 'pure' Drell-Yan events that fall inside the Z window to those that fall outside the Z window ($R_{\frac{out}{in}}$).

Here the method encounters more difficulties; when forming the 'Drell-Yan rich, WW-Like' sample it is found that even in the Z window there are very few events that survive after applying the $\not\!\!E_T$ cut. With such small numbers of events it is no longer possible to treat n^{in}_{ww} as a sample dominated by Drell-Yan since it is known that there is significant contribution from other physics processes in this region of high $\not\!\!E_T$. To account for this an estimate of the amount of 'contamination' from these other processes (WW,WZ,ZZ,$W\gamma$,fakes,$Z \to \tau\tau$, $t\bar{t}$) using Monte Carlo and QCD fake rate machinery is made and then subtracted from n^{in}_{ww}. The estimated amount of contamination (n^{in}_{other}) and the resulting values of n^{in}_{ww} for ee and $\mu\mu$ channels are shown in Table 8.4 and Table 8.5. With such a small number of data events it also becomes important to use Poisson, rather than Gaussian, errors to ensure that the upper bound is not underestimated[1]. These (asymmetric) Poisson errors on the data counts are then propagated through the rest of the calculation as normal. Low side errors are truncated at 0 events at the very end of the calculation to ensure that event counts remain positive integers.

[1]Taking a Poisson probability of the form $P(n) = e^{-\mu}\frac{\mu^n}{n!}$ and for n observed events plotting P(n) as a function of μ (such that the peak is at $n = \mu$). The Poisson 1σ error is then the range of the mean μ defined by $\Delta(\log(\mathrm{P})) = 0.5$.

The second difficulty is in the calculation of $R_{\frac{out}{in}}$. When applying this ratio to the event count in the 'Drell-Yan rich, WW-like' sample, it is being applied to events that have high $\not{E}_T$. Since high $\not{E}_T$ could be due to mis-measured leptons it implies that these events are more likely to have a lower reconstructed Z mass and hence a different value of $R_{\frac{out}{in}}$ than the pure, well reconstructed Drell-Yan sample. This effect will be lessened by the presence of the $\Delta\phi$ cut which is applied precisely for this reason, but a significant effect may remain. The window ratio is therefore calculated in both a pure Drell-Yan data sample and in the Monte Carlo; firstly with a $\not{E}_T$ cut and secondly with a $\not{E}_T$ and $\Delta\phi$ cut and the three results are compared. In a pure Drell-Yan data sample it is found that the ratio is about 0.1, but in MC with a $\not{E}_T > 25GeV$ it is closer to 0.5 when averaged over the dilepton categories and with a $\Delta\phi$ cut applied in addition, the electron channel ratio is reduced to around 0.3 (see Table 8.6), indicating this mis-measurement is an important effect in the calculation and hence it is safest to use the MC ratio that includes both the $\not{E}_T$ and $\Delta\phi$ cut, and not the data ratio.

The background estimate from Drell-Yan outside the Z window that results from these numbers is shown in Table 8.7.

	WW	$t\bar{t}$	WZ	Fake	$Z/\gamma^* \to \tau\tau$	ZZ	$W\gamma$	Total (n^{in}_{other})
ee	0.70	0.007	0.28	0.124	0.012	0.38	0.06	1.56
$\mu\mu$	0.65	0.0	0.28	0.092	0.007	0.39	0.0	1.42

Table 8.4: Number of events in the Z window with all Out-Of-Window WW cuts applied, used to statistically subtract the background from the outside window 'Drell-Yan rich, WW-like' event sample.

Inside the Z window

The contribution from inside the window is more difficult to calculate in the data because there are two, correlated cuts used to reject the Drell-Yan events inside

	ee	$\mu\mu$
n_{ww}^{in}	2	1

Table 8.5: Number of events in the outside window 'Drell-Yan rich, WW-like' data sample.

	ee			$\mu\mu$		
	Data	MC ($\not\!\!E_T$)	MC ($\not\!\!E_T, \Delta\phi$)	Data	MC ($\not\!\!E_T$)	MC ($\not\!\!E_T, \Delta\phi$)
Out-window	577	242	49	604	219	69
In-window	5459	471	152	4934	385	131
$R_{\frac{out}{in}}$	0.106±0.005	0.51±0.04	0.32±0.05	0.122±0.005	0.57±0.05	0.53±0.08

Table 8.6: Numbers of Drell-Yan events inside and outside the Z-mass window, used in the data-based estimate of the Drell-Yan background outside the Z window. Monte Carlo expectations are normalised to the Data luminosity.

Background Estimate	ee	$\mu\mu$
n_{raw}^{in}	2	1
$n_{ww}^{in} = (n_{raw}^{in} - n_{other}^{in})$	$(2 - 1.56)$	$(1 - 1.42)$
$(n_{ww}^{in} - n_{other}^{in}) \times R_{\frac{out}{in}}$	$(2 - 1.56) \times 0.32$ $= 0.14^{+0.45}_{-0.34}$	$(1 - 1.42) \times 0.53$ $= -0.22^{+0.70}_{-0.55}$

Table 8.7: Estimated amount of Drell-Yan background originating outside the Z window. Errors are statistical only

the window ($\not\!\!E_T$ and $\not\!\!E_T^{sig}$) rather than just one. Using the method described above, the data sample that is 'Drell-Yan rich, but WW-like', is in this case, the number of events in the Z window that pass all WW cuts but fail *either* the $\not\!\!E_T$ or the $\not\!\!E_T^{sig}$ cut ($\hat{n}_{ww}^{in}$). This is then extrapolated into the background estimate by multiplying this event count by the ratio of 'pure' Drell-Yan events that pass *both* the $\not\!\!E_T$ and $\not\!\!E_T^{sig}$ cuts to those that fail *either* the $\not\!\!E_T$ or the $\not\!\!E_T^{sig}$ cut ($R_{\frac{\hat{DY}}{DY}}$).

Here, again, the method encounters a problem of contamination. The numerator of the ratio $R_{\frac{\hat{DY}}{DY}}$ is a data sample that is, as before, low in statistics and therefore not dominated by Drell-Yan and again it is necessary to turn to Monte Carlo to estimate this contamination ($\hat{n}_{other}^{mc}$) and subtract it from the event count.

The calculated amounts of contamination and the resulting estimate of $R_{\frac{\hat{DY}}{DY}}$ are shown in Table 8.8 and Table 8.9. $\hat{n}^{in}_{ww}$ and the resulting background estimate is shown in Table 8.10 and Table 8.11 respectively. Again, Poisson errors are used on the small number of observed data events.

	WW	$t\bar{t}$	WZ	Fake	$Z\tau\tau$	ZZ	$W\gamma$	Total (n^{in}_{other})
ee	0.74	0.56	0.59	0.09	0.06	0.47	0.23	2.75
$\mu\mu$	0.65	0.51	0.53	0.07	0.05	0.47	0.0	2.27

Table 8.8: Number of events from MC in the Z window with $\not\!\!E_T > 25$ and $\not\!\!E_T^{sig} > 3$ used to statistically subtract the background from the numerator of $R_{\frac{\hat{DY}}{DY}}$.

	ee	$\mu\mu$
Passing $\not\!\!E_T \wedge \not\!\!E_T^{sig}$	3	3
Failing $\not\!\!E_T \lvert\rvert \not\!\!E_T^{sig}$	5456	4931
$R_{\frac{\hat{DY}}{DY}} = \frac{\text{Numerator}-\text{n}^{\text{in}}_{\text{other}}}{\text{Denominator}}$	$\frac{3-2.75}{5456}$ $= 4.6 \times 10^{-5}\,{}^{+0.0004}_{-0.0003}$	$\frac{3-2.27}{4931}$ $= 0.00015^{+0.0004}_{-0.0003}$

Table 8.9: The Monte Carlo corrected data estimate of Drell-Yan events passing $\not\!\!E_T$ and $\not\!\!E_T^{sig}$ cuts (numerator), and those failing (denominator), together with the resulting ratios.

	ee	$\mu\mu$
$\hat{n}^{in}_{ww}$	3160	3107

Table 8.10: Number of events in the inside window 'Drell-Yan rich, WW-like' event sample.

Background Estimate	ee	$\mu\mu$
$\hat{n}^{in}_{ww}$	3160	3107
$\hat{n}^{in}_{ww} \times R_{\frac{\hat{DY}}{DY}}$	$3160 \times (4.6 \times 10^{-5})$ $= 0.14^{+1.21}_{-0.86}$	3107×0.00015 $0.46^{+1.38}_{-1.27}$

Table 8.11: Estimate of amount of Drell-Yan background originating inside the Z window.

Total Data Estimate of Like-Flavour Drell-Yan

The further complication in the calculation is due to the dilepton category with two forward electrons (PHX-PHX) entering the dataset on a trigger that requires $\not\!\!E_T$; thereby making the data method invalid for this category. To compensate for this a scale factor, derived from Monte Carlo, to account for the expected contribution for the PHX-PHX channel is applied to the total background in the ee channel calculated using central electron - central electron (CEM-CEM) and central electron - forward electron (CEM-PHX) events only. Since the PHX-PHX category is a very small contribution to the acceptance this scale factor is expected to be only a small effect. Calculating this scale factor after all WW cuts gives a value of 1.0 with a systematic error of 15% (discussed in section 8.1.1).

The total estimate of the Drell-Yan background is shown in Table 8.12.

Channel	Inside	Outside	Total
ee	$0.14^{+1.21}_{-0.86}$	$0.14^{+0.45}_{-0.34}$	$0.27^{+1.29}_{-0.27}$
$\mu\mu$	$0.46^{+1.38}_{-1.27}$	$-0.22^{+0.70}_{-0.55}$	$0.46^{+1.56}_{-0.46}$

Table 8.12: Data based estimate of DY background inside and outside the Z window. Negative event counts and low-side errors are truncated to zero events.

The Monte Carlo estimates of the amount of contamination used in the above calculation are dependent upon the measured WW cross-section, which in turn depends upon the amount of Drell-Yan background, which is dependent upon the estimated amount of contamination. To take account of this dependence loop, an iteration calculation is performed. Firstly the amount of contamination is estimated using the theoretical WW cross-section. This estimate is then used to calculate the Drell-Yan background and then the measured WW cross-section. Using this measured cross-section, the contamination is recalculated and fed back into the Drell-Yan estimate and so on, until the result converges. The muon channel estimate converges after two iterations and the electron channel after three iterations. The final numbers for the post-iteration Drell-Yan background estimates are shown in Table 8.13.

Channel	Total Background
ee	$0.16^{+1.29}_{-0.16}$
$\mu\mu$	$0.38^{+1.56}_{-0.38}$

Table 8.13: Data based estimate of DY background after the iteration procedure to account for the assumed WW cross-section in the contamination estimates. Negative event counts and low-side errors are truncated to zero events.

8.1.1 Systematic Uncertainty On The Drell-Yan Background

The systematic error on the data based estimates of the Drell-Yan background consist of two major contributions; incorrectly estimating the scale factor to account for the PHX-PHX category and incorrectly estimating the fraction of events that fall inside the Z window to those outside the window. The first effect is estimated by calculating the scale factor at different stages of the WW cuts and gives a systematic error of around 15% in the final estimates. The second effect is estimated by observing the change in the final background estimate when changing the cuts used in the calculation of the window ratio and gives rise to a systematic error of 30%.

The dominant source of systematic uncertainty on the MC estimates of the Drell-Yan background derives from the Monte Carlo modelling of the $\not{E}_T$ distribution. The ΣE_T distribution for Drell-Yan data after the event selection is reasonably well described by Monte Carlo, so it is believed that discrepancies in the numerator of the $\not{E}_T^{sig}$ also dominate the systematic uncertainty on the Drell-

Yan background inside the Z-mass window. To estimate the size of the systematic effects of this mis-modelling on the $e\mu$ channel and $Z \rightarrow \tau\tau$ estimates, the $\not{E}_T$ distribution in the ee and $\mu\mu$ channel is studied by comparing Monte Carlo and data and the equivalent variation is then assumed to exist in the $e\mu$ and $Z \rightarrow \tau\tau$ channels.

Figure 8.2 shows the $\not{E}_T$ distribution for Drell-Yan data and Monte Carlo in both the ee and $\mu\mu$ channel. Whilst the $\mu\mu$ channel shows reasonable agreement between the data and the simulation, the ee channel has a systematic under-estimate in the Monte Carlo which is quite significant in the range of $10 < \not{E}_T < 20$ GeV.

It can be seen that the agreement between ee data and Monte Carlo is substantially improved after the $\Delta\phi$ cut (see Figure 8.3). This suggests that a major source of discrepancy between the data and Monte Carlo is the modelling of the calorimeter resolution, which is much reduced by the $\Delta\phi$ cut in this analysis and also explains the smaller discrepancy that is seen in the muon channel.

Despite the improvement after the $\Delta\phi$ cut, there is still some evidence for a harder $\not{E}_T$ distribution in ee data compared to Monte Carlo. To estimate the potential effect of this mis-modelling on the Drell-Yan background expectation, an additional Gaussian smearing is applied directly to the Monte Carlo $\not{E}_T$ distribution. The σ of the Gaussian is given by $A \times \sqrt{E_T}$, where A is a constant that is varied until the χ^2 of the data histogram and this smeared MC histogram is minimised. The χ^2 is calculated in the range 10 to 20 GeV where the agreement is worst. The χ^2 distribution as a function of A is shown in Figure 8.4(a). A polynomial fit is applied to this χ^2 function to obtain the minimum, and thereby the optimum amount of smearing, which is found to be at A = 0.18. The resulting $\not{E}_T$ distribution is shown in Figure 8.4(b) where it is compared to the data

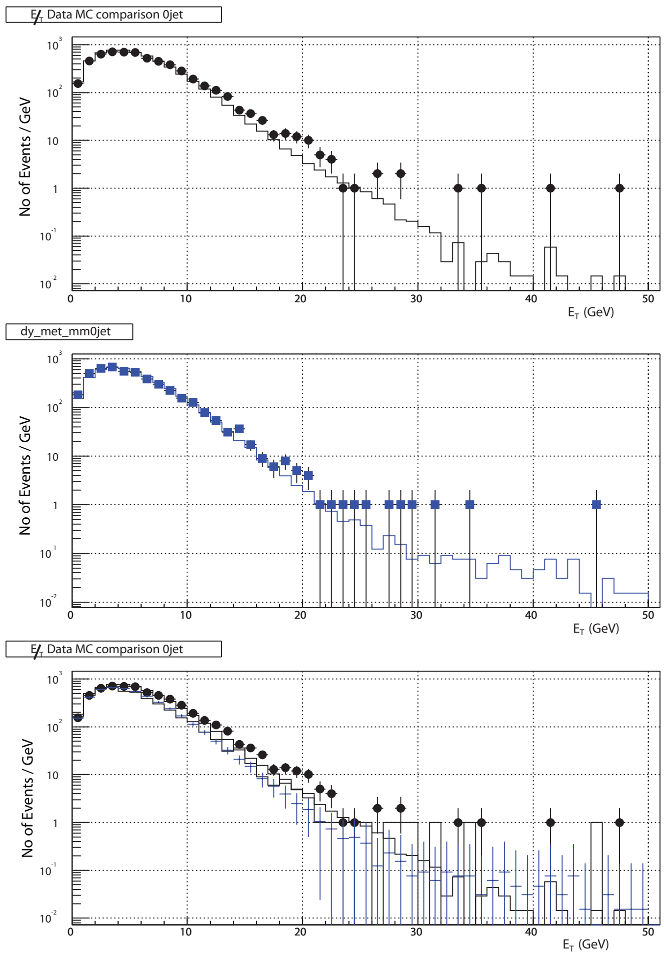

Figure 8.2: Comparison of the Data and Monte Carlo $\not{E}_T$ distributions in the ee channel (Top) and in the $\mu\mu$ channel (Bottom).

and the unsmeared Monte Carlo. Applying this optimised additional smearing gives rise to Monte Carlo background estimates that are 28% larger above the cut of 25 GeV. Varying the value of A from its minimum by 3 units of χ^2 (3 is approx χ^2_{min}) alters this portion by 13%. Changing the form of the smearing from $\sqrt{\sum E_T}$ to $\sqrt{\not{E}_T}$ alters it by around 2% and widening the range over which the χ^2 is calculated gives a 7% change.

The uncertainty on the $\mu\mu$ background is estimated in the same way. Much less disagreement is observed between the data and the MC in the muon case,

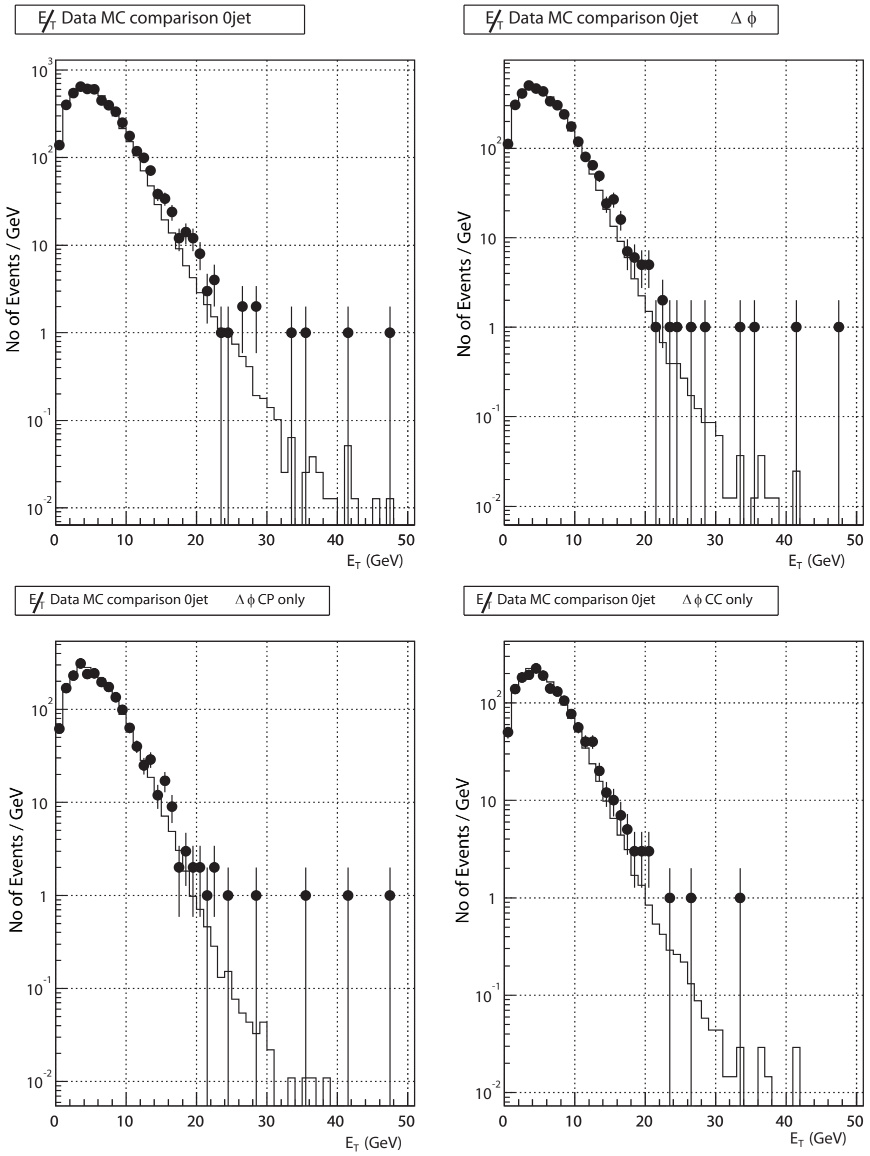

Figure 8.3: Discrepancy between data and MC in $\not\!\!E_T$ distribution (Top Left) is substantially improved by the addition of the $\Delta\phi$ cut (Top Right) and seems to be dominated by central-central events (Bottom Right), the central-plug events (Bottom Left) have better agreement in the range 10 to 20 GeV

which is born out by the much shallower χ^2 curve shown in Figure 8.5. However a wide range of smearing parameters are also not excluded and as in the electron channel, these can change the expected number of events significantly, up to 40%.

Conservatively therefore, a 40% systematic error, being the largest variation observed, is added to **all** Drell-Yan background estimates in **all** categories.

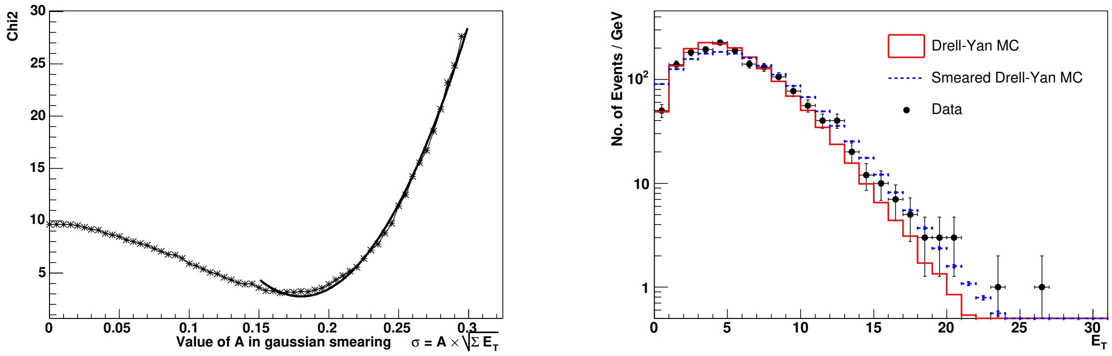

(a) (b)

Figure 8.4: 8.4(a) shows the χ^2 of the data-smeared MC histograms as a function of applied smearing. 8.4(b) shows a comparison of the $\not{E}_T$ distribution of DY ee events in the Data, Monte Carlo and the optimum smeared Monte Carlo.

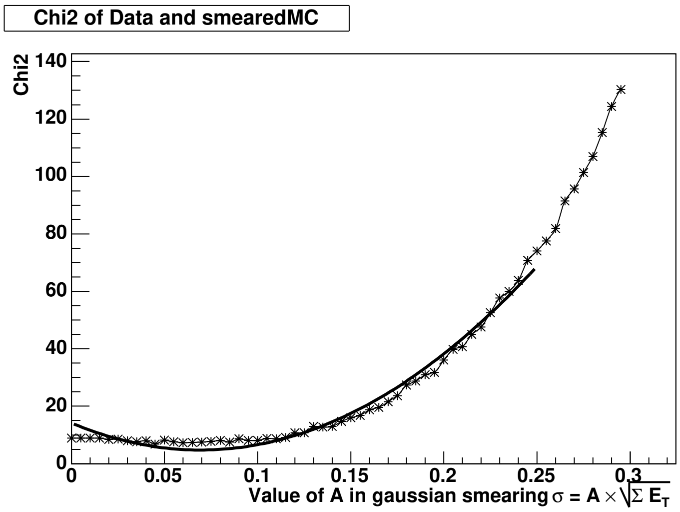

Figure 8.5: The χ^2 of the Data-Smeared MC histograms in the $\mu\mu$ channel as a function of applied smearing.

Summary: The Total Drell-Yan Background

The number of events in the Monte Carlo based estimates for the $e\mu$ channel, given in Tables 8.1 and 8.2, and for the $Z \rightarrow \tau\tau$ source, given in Table 8.3, are normalised to the data luminosity using $\sigma(DY) \times BR(ll) = 236\,\mathrm{pb}$ from PYTHIA with a NLO/LO k-factor of 1.4 [52]. These estimates are then combined with the data estimates from Table 8.12 to give the final background numbers from the Drell-Yan contribution in each dilepton channel in $184\,\mathrm{pb}^{-1}$ shown in Table 8.22. The asymmetric errors from the data estimates are propagated into the final total Drell-Yan estimates in each dilepton category along with the systematic errors.

8.2 QCD Background

A second large source of background is W+jet events where the quark or gluon jet fluctuates and fakes a lepton. This background is suppressed by the isolation requirements and the opposite sign cut (since jet-faked leptons have a random signed charge this requirement removes half the background) but nevertheless remains a substantial background.

8.2.1 Estimating QCD Background: The Fake Calculation

The method uses a similar philosophy as used to estimate the Drell-Yan background, simply replacing the "Drell-Yan rejection" cuts by the "Fake Rejection" cuts, i.e. rather than using ratios based on passing or failing $\not\!\!E_T$ cuts they are ratios based on lepton-ID cuts.

To estimate the fake background then, a P_T dependent jet $\rightarrow$ lepton fake ratio for each lepton category is obtained from a variety of QCD samples. These fake ratios are then applied to $l + \not\!\!E_T + d$ events, where d denotes any object which could fake a lepton in the signal sample ($W + jets$) to obtain the fake background estimates [53].

The Fake Ratios

The fake ratios are obtained from large samples of jet triggered data with E_T thresholds of 20, 50, 70, and 100 GeV. The trigger jet in each event is excluded from the fake ratio calculation to reduce trigger bias.

Calculated for each lepton category separately and in three P_T bins of $20 < P_T < 60$, $60 < P_T < 100$, $100 < P_T < 140$ GeV to account for a P_T dependence, the ratios are defined as $\frac{A}{B_e}$ and $\frac{A}{B_\mu}$.

A is the number of isolated baseline leptons found in the jet sample after correcting for the presence of real leptons from W and Z production.

Z contamination is reduced by excluding events from inside the Z mass window and the contamination from Ws is removed by direct subtraction as follows. The number of $W + \geq 1$ jet events in the signal sample, that also fired the jet triggers and thus contaminate the jet samples with real leptons, is subtracted from the number of events in the QCD samples. Electrons are not allowed to be the highest E_T object in the event, since the leading jet is thrown away in the fake calculation. Certain muon categories have no trigger and so must be estimated using Monte Carlo which incorporates a simulation of the jet triggers.

$\boldsymbol{B_e}$ is the number of jets with raw $E_T > 20$ GeV and $|\eta| < 1.1$ for central electrons and $1.2 < |\eta| < 2.5$ for plug electrons.

$\boldsymbol{B_\mu}$ is the number of tracks that are consistent with a MIP. They are required to pass the selection in Table 8.14

Corrected track $P_T > 20\,\mathrm{GeV}$
$E/P < 1.0$
track $\lvert z_0 \rvert < 60.0\,\mathrm{cm}$
track $\lvert d_0 \rvert < 0.2\,\mathrm{cm}$, 0.02 if track has silicon hits
non-cosmic

Table 8.14: Requirements for track to be included in calculation of $\boldsymbol{B_\mu}$.

With these definitions of A and B, the resulting probability for an object to fake a lepton is of the order 10^{-4} to 10^{-3} depending on the lepton type and detector region. For each P_T bin the ratios are averaged across the QCD samples and an error of half the spread of the central values is applied to each. The resulting ratios are summarised in Table 8.15

P_T (GeV)	$20 < \mathrm{P_T} < 60$	$60 < \mathrm{P_T} < 100$	$100 < \mathrm{P_T} < 140$
CEM	$5.0 \pm 2.0 \times 10^{-5}$	$3.0 \pm 3.0 \times 10^{-5}$	$6.0 \pm 5.0 \times 10^{-5}$
PHX	$3.9 \pm 0.5 \times 10^{-4}$	$5.9 \pm 4.2 \times 10^{-4}$	$2.4 \pm 2.8 \times 10^{-3}$
CMUP	$4.2 \pm 3.2 \times 10^{-4}$	$4.6 \pm 5.1 \times 10^{-3}$	$1.0 \pm 0.75 \times 10^{-2}$
CMU	$2.7 \pm 0.16 \times 10^{-4}$	$0.85 \pm 1.4 \times 10^{-3}$	0.0 ± 0.0
CMP	$5.3 \pm 4.6 \times 10^{-4}$	$4.9 \pm 5.0 \times 10^{-4}$	$9.2 \pm 12 \times 10^{-3}$
CMX	$3.7 \pm 2.2 \times 10^{-4}$	$1.4 \pm 1.2 \times 10^{-3}$	$1.2 \pm 1.8 \times 10^{-3}$
CMIO	$2.6 \pm 2.8 \times 10^{-3}$	$3.2 \pm 1.6 \times 10^{-3}$	$5.4 \pm 3.3 \times 10^{-3}$

Table 8.15: Fake ratios averaged over the QCD samples and after W/Z contamination subtraction for the various sample types.

Fake Background Estimate

To apply the fake ratios, the inclusive signal samples are searched for fakeable events. The fakeable events have one baseline lepton and B > 0, which are the jets or tracks as defined for the fake ratio calculations. The fakeable events are required to pass the remainder of the WW selection criteria. The opposite sign requirement is applied to events where the B is a track, assuming it fakes a muon with the same charge. If B is a jet, it fakes a positive or negative electron with equal probability and any likely deviation from a 50:50 charge symmetry in the W+jets sample is covered by the systematic errors discussed shortly. The resulting event counts of these fakeable events are shown in Table 8.16.

The fake estimate is obtained by applying the average fake ratios from the previous subsection to the number of B events found above. The resulting fake background estimates are shown by lepton category in Table 8.16 and are summarised in Table 8.17.

Fakeable-Lepton Type	Event Count	Background Estimate
CEM	5799	0.250±0.011±0.114±0.070
PHX	2576	0.605±0.027±0.299±0.169
CMUP	54	0.041±0.006±0.016±0.020
CMU	18	0.008±0.002±0.006±0.004
CMP	27	0.016±0.003±0.016±0.008
CMX	37	0.033±0.005±0.026±0.016
CMIO	181	0.426±0.032±0.376±0.213

Table 8.16: Number of fakeable events found in the signal sample and the resulting fake background estimates. First error is from the propagation of the statistical error on the number of fakeable events in the signal sample, the second error is due to the propagation of the fake ratio error and the third is the systematic error discussed in Section 8.2.2

dilepton category	Fake Background Estimate
ee	0.519±0.025±0.197±0.145
eμ	0.682±0.032±0.274±0.267
$\mu\mu$	0.178±0.018±0.133±0.089
Total	1.379±0.044±0.495±0.501

Table 8.17: Summary and totals of the fake background estimates. Errors follow the same description as in Table 8.16

8.2.2 Fake Systematics

A variety of systematic effects in the QCD background estimate must be accounted for. Firstly, if the jets in the QCD sample are different to the jets in the signal sample then applying ratios calculated in one to the other would result in erroneous estimates. This effect is estimated by varying the definition of the denominator objects; in the case of electrons, by varying the EM energy fraction of the jets (from 0.0 to 0.8) to make them more or less electron like, and in the case of muons, by varying the E/P cut (from 0.0 to 1.0) used to make the denominator objects more or less muon like. No effect is observed in the electrons, but some dependence is seen in the muons resulting in a systematic error of 50% to cover all observed changes in the fake ratios.

A second possible source of systematic error is in the use of jet energy rather than EM energy in the definition of the electron denominator objects. This is estimated by simply repeating the calculation using denominator objects defined by EM energy rather than raw jet energy (i.e. multiplying the raw energy by the EM-fraction). This gives rise to a 20% variation in fake ratios which is then propagated to the fake background estimates along with the previous systematic effects above and added in quadrature to give a final systematic error on the fake background of 36%.

8.3 The $W + \gamma$ Background

The background from radiative W production, where the γ fakes the second lepton, can be significant. This contributes to dilepton categories in which one leg is a PHX electron, since such electrons have no track isolation or conversion requirements.

This background is estimated by running over approximately 425k $W+\gamma$ Monte Carlo events, generated using the Monte Carlo program WGAMMA and described in [54] and references therein. The $k-$factor corrected cross section is $\sigma(W)\times BR(W\to l\nu)=44.7$ pb (for $E_T^\gamma > 5$ GeV, $|\eta^\gamma|<10$, and $\Delta R(l,\gamma)>0.2$). Since the Monte Carlo datasets include both electron and muon decays, the effective integrated luminosity of the sample is 4.74 fb^{-1}.

Running the Monte Carlo sample through the full analysis chain, a total of 35 events survive all cuts, corresponding to an estimated background of 1.1 ± 0.2 events. The breakdown by dilepton category is given in table 8.18.

In order to estimate any possible overlap between this estimate and the data based fake background estimate, the fake ratios derived from QCD data are applied to the $W+\gamma$ Monte Carlo. The resulting total expected number of events calculated this way is found to be negligible, and therefore it is assumed that no overlap exists between these two background estimates.

$W(\gamma)\to e\nu\gamma$	
CEM-CEM	0.08 ± 0.06
CEM-PHX	0.31 ± 0.10
PHX-PHX	0.09 ± 0.05
Total	0.48 ± 0.13
$W(\gamma)\to \mu\nu\gamma$	
μ-CEM	0.07 ± 0.05
μ-PHX	0.50 ± 0.12
Total	0.57 ± 0.13
Combined	
Total	1.05 ± 0.19

Table 8.18: The breakdown by dilepton category of the background in $184\,\mathrm{pb}^{-1}$ due to radiative W production.

8.4 The $t\bar{t}$ Background

Production of $t\bar{t}$ pairs in the dilepton channel $t\bar{t} \to l\bar{\nu}\bar{l}\nu b\bar{b}$ result in a final state identical to WW candidates apart from the presence of additional b-jets. The jet veto cut is effective at reducing this background, but some background remains when the jets in the $t\bar{t}$ event are missed (either fiducially or by failing the E_T cut).

The sample used to determine the $t\bar{t}$ background rejection consisted of 349933 PYTHIA $t\bar{t}$ events. Using the theoretical value of $\sigma(t\bar{t}) = 7$ pb, the luminosity of the sample is 50 fb^{-1}.

Table 8.19 shows the $t\bar{t}$ rejection after every analysis cut. The jet veto is mainly responsible for rejecting $t\bar{t}$ events. The expected $t\bar{t}$ background numbers in 184 pb^{-1} are given at the end of this section in the summary Table 8.22. The biggest systematic effect observed is due to the jet energy scale. It is found that varying the jet energy scale by $\pm 1\sigma$ alters the $t\bar{t}$ background estimate by around 30%.

	$t\bar{t}$					
	ee		$\mu\mu$		$e\mu$	
Cut		%		%		%
Lepton ID	1278.0		1532.0		2837.0	
Isolation	907.0	70.97±1.27	1081.0	70.56±1.16	2057.0	72.51±0.84
Conv+Cosmic	884.0	97.46±0.52	1081.0	100.00±0.00	2021.0	98.25±0.29
Z-veto	813.0	91.97±0.91	997.0	92.23±0.81	2021.0	100.00±0.00
$\not{E}_T$ >25 GeV :	739.0	90.90±1.01	900.0	90.27±0.94	1762.0	87.18±0.74
$\Delta\Phi > 20°$ if $\not{E}_T$ <50	688.0	93.10±0.93	829.0	92.11±0.90	1612.0	91.49±0.66
0 jets	6.0	0.87±0.35	4.0	0.48±0.24	15.0	0.93±0.24
Opposite Sign	5.91	98.57±4.84	4.0	100.00±0.00	14.67	97.82±3.77
$t\bar{t}$ in $184pb^{-1}$	0.021 ± 0.009		0.012 ± 0.006		0.046 ± 0.012	

Table 8.19: $t\bar{t}$ events from the PYTHIA sample described in the text passing dilepton cuts for each dilepton category, and the associated efficiencies of each cut (after all previous cuts have been applied). Errors are statistical only.

8.5 The WZ Background

WZ events can only constitute a background in this analysis if some part of the final state is mis-measured, either a missing lepton in the case of both bosons decaying leptonically or by generating fake $\not\!\!E_T$ through mis-measurement of hadronic activity in the case of hadronic decays. The requirement that the event have exactly 2 leptons approximately halves this background compared to allowing trilepton events through the analysis. Of the remaining background, the jet veto gets rid of most of the $WZ \rightarrow q\bar{q}'\ ll$ contribution and only 70% of the dilepton events from $WZ \rightarrow \ell\nu\ \ell^+\ell^-$ are opposite sign. The resulting contribution to the background due to WZ production therefore predominantly occurs when both bosons decay leptonically and one of the leptons is not detected.

The sample used to determine the WZ background consisted of 80430 WZ PYTHIA events. In this sample a dilepton filter was applied after the generation and prior to simulation that demanded two leptons (e,μ or τ) with $P_T > 10$ GeV and $|\eta| < 2$, thereby allowing the inclusion of the (very) small contribution from the case when both leptons come from the Z. The efficiency of the filter is 5.80±0.01%.

With a cross-section $\sigma_{NLO}^{WZ} = 3.96 \pm 0.06$ pb [55], the luminosity of the sample was estimated to be 350 fb^{-1}. The cut efficiencies for WZ are given in Table 8.20 and the expected number of WZ background events is reported in table 8.22.

A systematic error the same as that for WW is assigned to the WZ background, since the processes are somewhat similar.

Cut	WZ ee	%	WZ $\mu\mu$	%	WZ $e\mu$	%
Lepton ID	10789.0		9238.0		2480.0	
Isolation	9221.0	85.47±0.34	8073.0	87.39±0.35	1980.0	79.84±0.81
Conv+Cosmic	9054.0	98.19±0.14	8073.0	100.00±0.00	1962.0	99.09±0.21
Z-veto with $\not{E}_T^{sig}$	2551.0	28.18±0.47	2275.0	28.18±0.50	1962.0	100.00±0.00
$\not{E}_T$ >25 GeV :	2072.0	81.22±0.77	1820.0	80.00±0.84	1512.0	77.06±0.95
$\Delta\Phi > 20°$ if $\not{E}_T$ <50	1909.0	92.13±0.59	1697.0	93.24±0.59	1366.0	90.34±0.76
0 jets	739.0	38.71±1.11	960.0	56.57±1.20	699.0	51.17±1.35
Opposite Sign	591.96	80.10±1.47	739.0	76.98±1.36	328.28	46.96±1.89
WZ in $184pb^{-1}$	0.29 ± 0.01		0.33 ± 0.01		0.15 ± 0.01	

Table 8.20: PYTHIA WZ events passing dilepton cuts for each dilepton category, and the associated efficiencies of each cut (after all previous cuts have been applied). Errors are statistical only.

8.6 The ZZ Background

Events of the type $ZZ \rightarrow l^+l^-\nu\bar{\nu}$ constitute a significant background since they are extremely similar to the WW signal; two leptons, no jets and large real $\not{E}_T$.

This background is evaluated by running on a sample of 290541 PYTHIA generated ZZ events. PYTHIA includes γ^* in a consistent way. At the generator level each Z/γ^* in the sample is required to have a mass larger than 30 GeV since very little acceptance is expected below this mass. A post-generator filter required at least two generator level electrons or muons with $P_T > 1$ GeV, with a resulting efficiency of 21.3%. With PYTHIA's Leading Order cross-section, combined with a MCFM k-factor calculated with the same cuts, the cross-section is found to be $\sigma_{NLO}^{ZZ} = 1.30$ pb, giving an effective luminosity of the sample of 1000 fb^{-1}. The numbers of events surviving each cut are shown in Table 8.21.

It can be seen that the Z-veto is not as effective at removing these events as it is at removing Drell-Yan events, due to the fraction of ZZ events with real missing-E_T. The final number of background events expected from ZZ production is 0.70 ± 0.06. This is of the same order as the background from

WZ production. A systematic error of 10% is applied to this estimate, the same as for the WW signal.

Cut	ZZ					
	ee		$\mu\mu$		$e\mu$	
		%		%		%
Lepton ID	23364.0		21926.0		1714.0	
Isolation	19666.0	84.17±0.24	18563.0	84.66±0.24	1090.0	63.59±1.16
Conv+Cosmic	19279.0	98.03±0.10	18563.0	100.00±0.00	1074.0	98.53±0.36
Z-veto with $\not\!\!E_T^{sig}$	4926.0	25.55±0.31	4812.0	25.92±0.32	1074.0	100.00±0.00
$\not\!\!E_T$ >25 GeV :	3514.0	71.34±0.64	3645.0	75.75±0.62	650.0	60.52±1.49
$\Delta\Phi > 20°$ if $\not\!\!E_T$ <50	3229.0	91.89±0.46	3384.0	92.84±0.43	512.0	78.77±1.60
0 jets	2343.0	72.56±0.79	2445.0	72.25±0.77	145.0	28.32±1.99
Opposite Sign	2168.53	92.55±0.54	2376.0	97.18±0.33	74.29	51.23±4.15
ZZ in $184pb^{-1}$	0.35 ± 0.01		0.34 ± 0.01		0.011 ± 0.001	

Table 8.21: PYTHIA ZZ events passing dilepton cuts for each dilepton category, and the associated efficiencies of each cut (after all previous cuts have been applied). Errors are statistical only.

8.7 Heavy Flavour Backgrounds

The requirement that both leptons be isolated is expected to significantly reduce any $b\bar{b}$, $c\bar{c}$ or $Wb\bar{b}$ background. In addition some of the heavy flavour contribution will be included in the QCD estimate. The two main contributions are QCD events containing heavy flavour jets and $W\bar{b}b$

8.7.1 QCD+Heavy Flavour

The $b\bar{b}$ contribution is estimated by running on a PYTHIA $b\bar{b}$ sample with an effective luminosity of $733\,\mathrm{pb}^{-1}$. After lepton ID and isolation requirements only, only 1 ee, 2 $e\mu$ and 0 $\mu\mu$ $b\bar{b}$ events remain. If any isolation requirements on one lepton leg are lifted 34 events remain, indicating the effectiveness of isolation in removing heavy flavour.

To get a approximate limit from these numbers on the $b\bar{b}$ contribution it is assumed that the $\not{E}_T > 25\,\mathrm{GeV}$ cut efficiency is approximately the same as that in $Z \to \tau\tau$ i.e. 5% (see table 8.3). By not applying *any* other cut efficiencies, this gives a $b\bar{b}$ contribution of 0.04 events, thereby showing that QCD + heavy flavour can be neglected as a source of background in this analysis.

8.7.2 $W\bar{b}b$

Passing a large Monte Carlo sample of $W\bar{b}b$ through the WW event selection results in fewer than 0.01 events remaining and so this process is assumed to be negligible also. As a cross-check, applying the fake ratios found in QCD data to the number of fakeable events in this sample also resulted in a negligible event expectation, within large statistical errors.

8.8 Summary Of All Backgrounds

Table 8.22 gives a summary of the expected contribution from each background source in each dilepton channel.

	CDF Run II			
Source	ee	$\mu\mu$	$e\mu$	$\ell\ell$
Drell-Yan e^+e^-	$0.16\,^{+1.29}_{-0.16}$	0.00 ± 0.00	0.05 ± 0.04	$0.21\,^{+1.29}_{-0.17}$
Drell-Yan $\mu^+\mu^-$	0.00 ± 0.00	$0.38\,^{+1.56}_{-0.38}$	0.28 ± 0.13	$0.66\,^{+1.56}_{-0.40}$
Drell-Yan $\tau^+\tau^-$	0.047 ± 0.021	0.046 ± 0.020	0.099 ± 0.041	0.19 ± 0.05
WZ	0.29 ± 0.03	0.33 ± 0.03	0.15 ± 0.02	0.76 ± 0.06
ZZ	0.35 ± 0.04	0.34 ± 0.04	0.011 ± 0.002	0.70 ± 0.07
$W + \gamma$	0.48 ± 0.13	0.00 ± 0.00	0.57 ± 0.13	1.06 ± 0.19
$t\bar{t}$	0.021 ± 0.011	0.012 ± 0.007	0.046 ± 0.018	0.078 ± 0.023
Fake	0.52 ± 0.19	0.17 ± 0.16	0.65 ± 0.37	1.34 ± 0.66
Total Background	$1.86\,^{+1.31}_{-0.30}$	$1.27\,^{+1.57}_{-0.42}$	1.86 ± 0.43	$5.00\,^{+2.15}_{-0.84}$

Table 8.22: Summary of all backgrounds. Errors are statistical and systematic combined.

Chapter 9

Experimental Results.

This chapter presents the results of the $WW \to l\bar{\nu}\bar{l}\nu$ selection and the extraction of the cross-section from the data. Several kinematic distributions of the data candidates are compared to the theoretical predictions and one in particular, the lepton-P_T, is used to extract limits on anomalous trilinear gauge boson couplings.

9.1 WW Data Candidates

The expected number of $WW \to l\bar{\nu}\bar{l}\nu$ candidate events found in the data is simply the sum of the background expectation and the signal expectation in each dilepton channel. These expectations are shown in Table 9.2 below. The data candidates are obtained by passing the datasets discussed in Chapter 4 through the $WW \to l\bar{\nu}\bar{l}\nu$ event selection. 17 candidate events are observed, 6 in the ee channel, 5 in the $e\mu$ channel and 6 in the $\mu\mu$ channel. Trilepton candidates are also listed for interest (recall that trilepton events are vetoed since it significantly reduces the WZ background and has almost no effect on the WW acceptance). The numbers of data events surviving each cut in the event selection are summarised in Table 9.1 and the resulting data candidates are combined with the expectation from backgrounds and signal in the final summary Table 9.2.

Category	ID	ISO	Conv+Cosm	Z veto	$\not\!\!E_T > 25$GeV	$\Delta\phi$	0j	OS
CEM-CEM	4227	3620	3455	402	15	7	4	4
CEM-PHX	4015	3585	3487	275	7	6	4	2
PHX-PHX	43	36	36	9	6	4	0	0
$e-e$	8285	7241	6978	686	28	17	8	**6**
CEM-CMUP	30	19	17	17	4	3	1	1
CEM-CMU	7	4	4	4	1	1	0	0
CEM-CMP	11	4	4	4	2	2	1	1
CEM-CMX	24	12	11	11	6	6	2	2
CEM-CMIO	46	16	16	16	3	2	0	0
PHX-CMUP	11	10	10	10	4	4	1	0
PHX-CMU	1	1	1	1	0	0	0	0
PHX-CMP	5	2	2	2	1	1	1	1
PHX-CMX	9	8	8	8	2	1	0	0
PHX-CMIO	15	3	3	3	0	0	0	0
$e-\mu$	159	79	76	76	23	20	6	**5**
CMUP-CMUP	1014	948	948	121	2	2	1	1
CMUP-CMU	429	405	405	41	1	0	0	0
CMUP-CMP	566	517	517	59	5	5	1	1
CMUP-CMX	1151	1079	1079	114	4	3	1	1
CMUP-CMIO	2076	1939	1939	218	4	4	2	2
CMX-CMX	404	363	363	36	1	1	0	0
CMX-CMU	259	249	249	26	0	0	0	0
CMX-CMP	263	243	243	32	0	0	0	0
CMX-CMIO	911	834	834	78	3	1	1	1
$\mu-\mu$	7073	6577	6577	725	20	16	6	**6**
TRILEPTON	7	7	7	3	0	0	0	0

Table 9.1: WW dilepton channel analysis results in $184\,\mathrm{pb}^{-1}$ for each of the dilepton categories. Also shown is the trilepton category not included in this analysis.

9.1.1 Candidate Kinematics

Figures 9.1 and 9.2 display the kinematic features of the candidate events with the theoretical predictions from Monte Carlo. The open histograms are the Monte Carlo expectation of signal plus background, the solid histograms are the expected

Source	ee	$\mu\mu$	$e\mu$	$\ell\ell$
Drell-Yan e^+e^-	$0.16^{+1.29}_{-0.16}$	0.00 ± 0.00	0.05 ± 0.04	$0.21^{+1.29}_{-0.17}$
Drell-Yan $\mu^+\mu^-$	0.00 ± 0.00	$0.38^{+1.56}_{-0.38}$	0.28 ± 0.13	$0.66^{+1.56}_{-0.40}$
Drell-Yan $\tau^+\tau^-$	0.047 ± 0.021	0.046 ± 0.020	0.099 ± 0.041	0.19 ± 0.05
WZ	0.29 ± 0.03	0.33 ± 0.03	0.15 ± 0.02	0.76 ± 0.06
ZZ	0.35 ± 0.04	0.34 ± 0.04	0.011 ± 0.002	0.70 ± 0.07
$W+\gamma$	0.48 ± 0.13	0.00 ± 0.00	0.57 ± 0.13	1.06 ± 0.19
$t\bar{t}$	0.021 ± 0.011	0.012 ± 0.007	0.046 ± 0.018	0.078 ± 0.023
Fake	0.52 ± 0.19	0.17 ± 0.16	0.65 ± 0.37	1.34 ± 0.66
Total Background	$1.86^{+1.31}_{-0.30}$	$1.27^{+1.57}_{-0.42}$	1.86 ± 0.43	$5.00^{+2.15}_{-0.84}$
$WW \to$ dileptons	2.61 ± 0.31	2.48 ± 0.29	5.11 ± 0.60	10.20 ± 1.19
Total Expectation	$4.47^{+1.36}_{-0.45}$	$3.75^{+1.60}_{-0.53}$	6.97 ± 0.76	$15.20^{+2.51}_{-1.55}$
Run 2 Data	6	6	5	17

Table 9.2: Final $WW \to l\bar{\nu}\bar{l}\nu$ event expectations and observed data candidates. Errors are statistical and systematic combined

total background and the black dots are the data with statistical error bars. The signal histograms are normalised to the measured WW cross-section. In the angular distributions the data candidates are separated into the dilepton categories ee, $\mu\mu$ and $e\mu$.

The plots show excellent agreement with the Standard Model expectations, given the small statistics, and there are no major shape discrepancies observed. The final two plots, Figures 9.2(c) and 9.2(d) showing the $\not{E}_T$ and $\not{E}_T^{sig}$ variables, demonstrate that despite the difficulties these distributions are reasonably well modelled and the cuts are being applied in a sensible way. The lepton-P_T distribution (Figure 9.1(c)) is of particular interest since this possesses the most sensitivity to the presence of anomalous couplings, which will be explored in Section 9.3.

Figures A.1 through A.5 of Appendix A show event displays of a few of the candidate events.

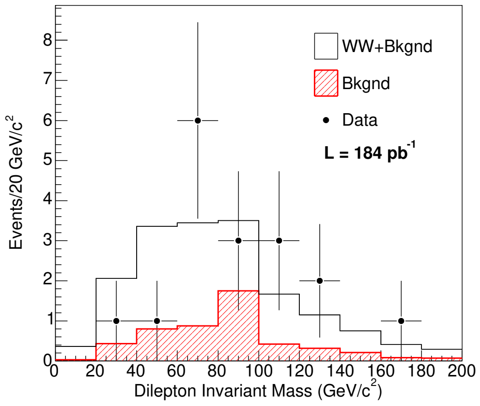

(a) The dilepton invariant mass.

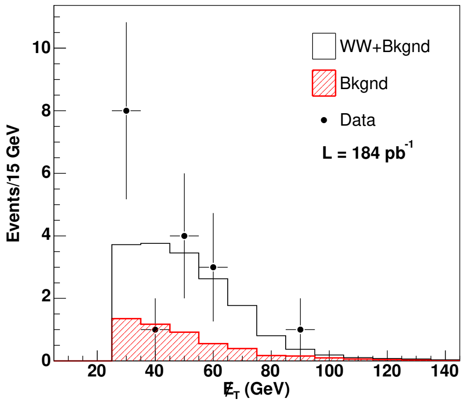

(b) The missing transverse energy.

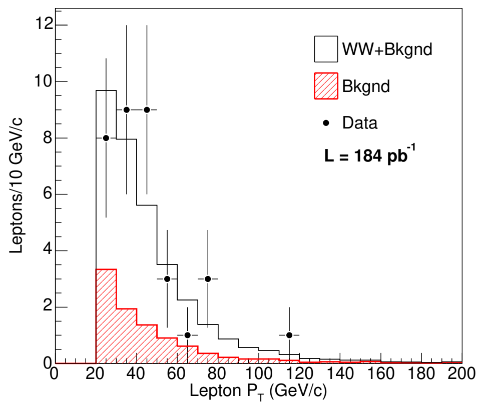

(c) The transverse momentum of each lepton.

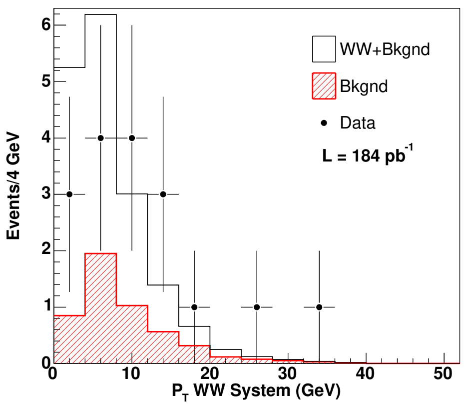

(d) The transverse momentum of the WW system.

Figure 9.1: Kinematics of data candidates compared to theoretical predictions: 9.1(a) Dilepton invariant mass, 9.1(b) Missing Transverse energy($\not\!\!E_T$), 9.1(c) P_T of leptons and 9.1(d) P_T of WW system. The data is overlayed on the total Standard Model expectation of WW plus all backgrounds after all cuts(black line histogram). The solid histogram is backgrounds only.

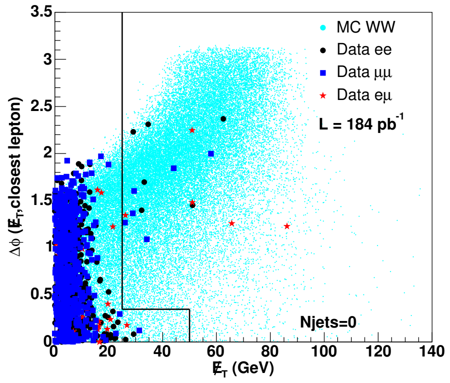

(a) The azimuthal separation between the $\not\!\!E_T$ and the closest lepton or jet versus the $\not\!\!E_T$.

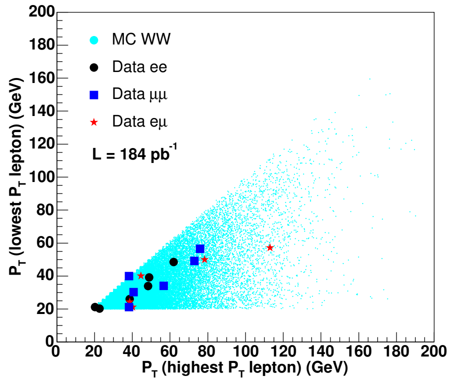

(b) Correlation between P_T of the leading lepton and the second lepton

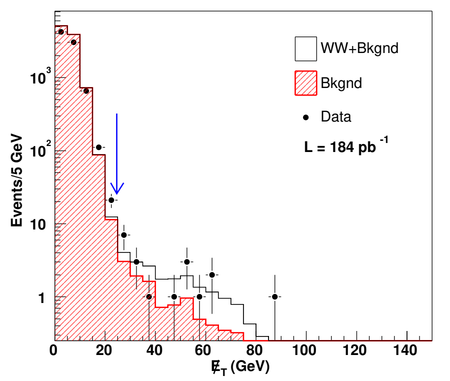

(c) The missing transverse energy before $\not\!\!E_T$ and $\not\!\!E_T^{sig}$ cuts.

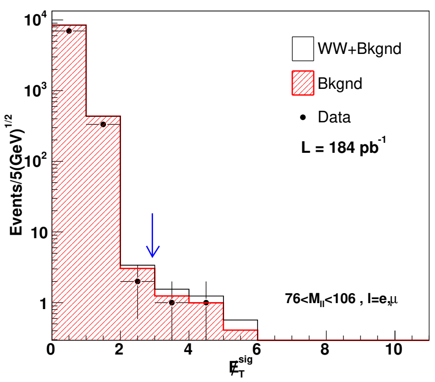

(d) The missing transverse energy significance before the $\not\!\!E_T$ and $\not\!\!E_T^{sig}$ cuts.

Figure 9.2: Top row shows angular kinematics of data candidates compared to theoretical predictions. In (a) all cuts except $\not\!\!E_T$, $\Delta\phi$ and opposite sign are applied; in (b) all cuts are applied. Bottom row shows missing energy variables before the $\not\!\!E_T$ and $\not\!\!E_T^{sig}$ cuts. Data is overlayed on the WW plus all backgrounds Monte Carlo expectation (black line histogram). The solid histogram is backgrounds only. All other WW cuts are applied.

9.2 Cross-Section Determination

The measured WW cross-section is given by the equation

$$\sigma_{meas}^{WW} = \frac{(N_{obs} - N_{bk})}{A_{abs} \times \mathcal{L}} = \frac{(N_{obs} - N_{bk})}{A_{lep} \times [3 \times BR(W \to l\nu)]^2 \times \mathcal{L}} \tag{9.1}$$

where N_{obs} is the observed number of events and N_{bk} is the expected number of background events. The efficiency A_{abs} is the total efficiency for selecting $p\bar{p} \to WW$ events in this analysis. As described earlier in Section 7.1 this acceptance has been estimated using a WW sample with leptonic decays only, hence the efficiency measured is in fact A_{lep}. This is converted into A_{abs} by folding in the Standard Model branching ratio of $BR(W \to l\nu) = 0.1068$ [58] as in Equation 7.2

.

Noting that the denominator in Equation 9.1 can be re-expressed in terms of the total expected number of events, N_{WW}^{pred}, by rearranging thus:

$$\begin{aligned} \sigma_{meas}^{WW} &= \frac{(N_{obs} - N_{bk})}{A_{lep} \times [3 \times BR(W \to l\nu)]^2 \times \mathcal{L}} \times \frac{\sigma_{theory}^{WW}}{\sigma_{theory}^{WW}} \\ \sigma_{meas}^{WW} &= \frac{(N_{obs} - N_{bk})}{N_{WW}^{pred}} \times \sigma_{theory}^{WW} \end{aligned} \tag{9.2}$$

The advantage in using Equation 9.2 is that the various efficiencies, scale factors and luminosities for the different dilepton categories are automatically taken into account in N_{WW}^{pred}, whereas Equation 9.1 would require the use of average luminosities and efficiencies. Clearly there is no sensitivity to the assumed value of the theoretical cross-section since it cancels in the numerator and denominator, but there is sensitivity to the value of the branching ratio $BR(W \to l\nu)$.

The method described in [59] is used to calculate a 68.27% confidence level for the signal. This method takes the number of observed events and the expected backgrounds as inputs and is equally valid at setting upper limits and two-sided confidence intervals. If the lower confidence level is above 0.0 then a central cross-section value can be quoted.

Taking the systematic errors discussed in the previous chapters and the luminosity error of 6% described in section 4.1.2 and propagating them using Equation 9.1 and calculating the cross-section using Equation 9.2 the measured result for the $p\bar{p} \rightarrow W^+W^-$ cross-section is found to be

$$\sigma^{WW}_{meas} = 14.5^{+5.8}_{-5.1}(stat)^{+1.8}_{-3.0}(syst) \pm 0.9(lum)\ pb \tag{9.3}$$

9.3 Limits On Anomalous Trilinear Gauge Boson Couplings

Using the measured cross-section from the previous chapter it is possible to extract limits on the values of any possible anomalous trilinear gauge boson couplings consistent with the data. It is also possible to use the kinematic properties of the candidate WW events to place additional and even tighter limits on any such deviation from the Standard Model couplings.

9.3.1 A First Estimate: Coupling Limits From The Cross-Section

The presence of anomalous couplings tends to increase the cross-section from the Standard Model value. Therefore a measured cross-section can give direct limits on the values of anomalous couplings.

Producing limits directly from the cross-section begins by estimating the NLO cross-section using MCFM for various different coupling values in an 11 by 11 grid from -3 to +3 in { $\Delta\kappa, \lambda$ } space, and repeated using both the Equal and HISZ coupling schemes. The cross-section at these points is then fitted with a parabolic surface of the form $\sigma_{WW}^{anom} = a_0 + a_1\lambda + a_2\Delta\kappa + a_3\lambda\Delta\kappa + a_4(\lambda)^2 + a_5(\Delta\kappa)^2$. The form of this parabolic surface can be easily understood by considering the addition of an anomalous coupling component to the amplitude, $\mathcal{A} = \mathcal{A}_{SM} + \mathcal{A}_{ANOM}$, which when squared to give the cross-section results in a quadratic dependence on the anomalous couplings. The limits on the anomalous couplings can then be estimated by taking the 95% upper confidence level of the measured cross-section and finding the intercept with these paraboloids.

The 95% C.L. upper limit on the measured cross-section is found to be 26.5 pb and the resulting limits are shown in Figure 9.3 and Figure 9.4 and restrict the coupling values to about $|\Delta\kappa| < 1.5$ and $|\lambda| < 1.0$ (95% C.L) in the HISZ couplings and in the Equal couplings to about $|\Delta\kappa| < 1.0$ and $|\lambda| < 0.5$ (95% C.L.).

9.3.2 Limits From The Lepton P_T Spectrum

The high-P_T^{WW} part of the cross-section has more sensitivity to the presence of anomalous couplings [60] and so the lepton-P_T spectrum of the observed WW dilepton candidates will possess higher sensitivity than the overall cross-section. A maximum likelihood fit to the lepton P_T spectrum of the candidates will therefore result in tighter limits on the anomalous couplings.

Expected signal P_T spectra are generated as a function of anomalous couplings. From Figure 9.4(c) and Figure 9.3(c) it can be seen that the samples required need only extend from -2 to +2 in $\{\Delta\kappa,\lambda\}$ space. From Figure 9.4(c) it can also be seen that the choice of $\Lambda = 1$ TeV is the safest way to ensure that the experimental limits are tighter than the limits from tree-level unitarity requirements (as discussed in chapter 2).

Given that the WW kinematics change with the addition of anomalous couplings, the detection efficiency is also likely to change. Therefore generator level

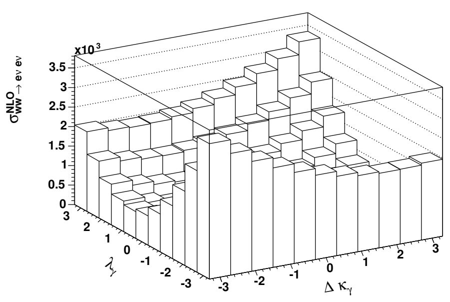

(a) NLO $\sigma(WW \to e\bar{\nu}\bar{e}\nu)$

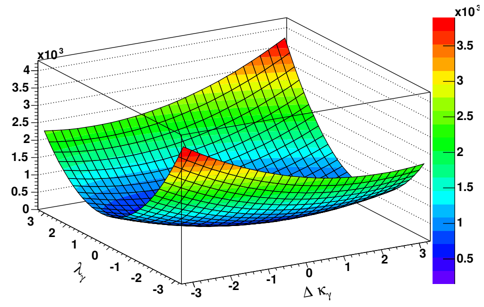

(b) Fitted NLO $\sigma(WW \to e\bar{\nu}\bar{e}\nu)$

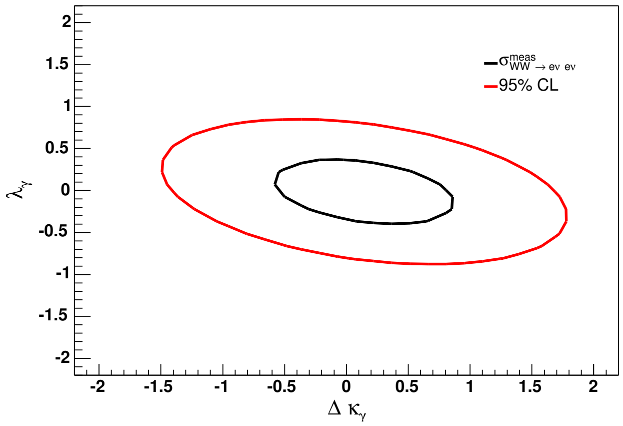

(c) Limits from intercept of measured $\sigma(WW \to e\bar{\nu}\bar{e}\nu)$ and 95% CL upper limit

Figure 9.3: Estimate of (HISZ) coupling limits extracted using the measured WW cross-section. The NLO cross-section from MCFM is calculated in the $WW \to e\bar{\nu}\bar{e}\nu$ channel and compared to the 95% C.L. upper limit of $\sigma(WW)^{meas} \times BR(W \to e\nu)^2$.

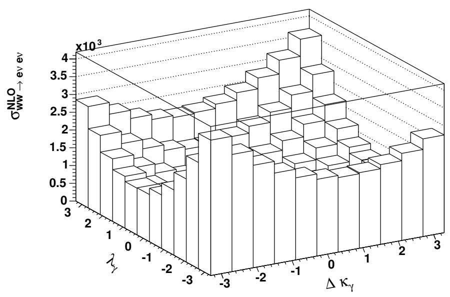

(a) NLO $\sigma(WW \to e\bar{\nu}\bar{e}\nu)$

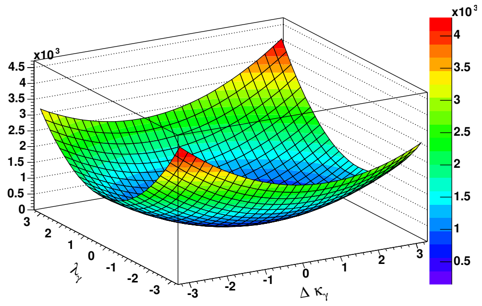

(b) Fitted NLO $\sigma(WW \to e\bar{\nu}\bar{e}\nu)$

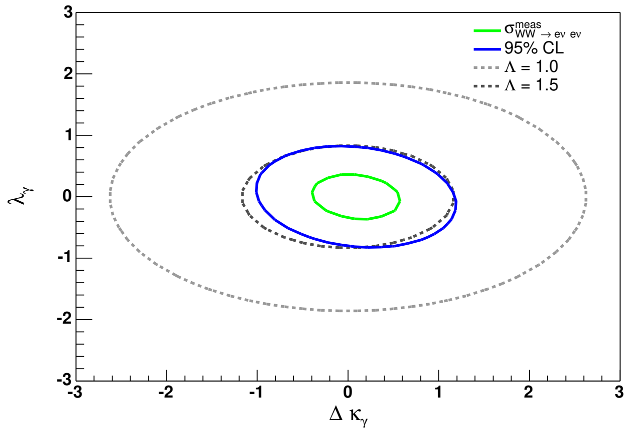

(c) Limits from intercept of measured $\sigma(WW \to e\bar{\nu}\bar{e}\nu)$ and 95% CL upper limit

Figure 9.4: Estimate of (EQUAL) coupling limits extracted using the measured WW cross-section. The NLO cross-section from MCFM is calculated in the $WW \to e\bar{\nu}\bar{e}\nu$ channel and compared to the 95% C.L. upper limit of $\sigma(WW)^{meas} \times BR(W \to e\nu)^2$. Limits from Λ unitarity requirements are also shown

quantities cannot be used and instead the full detector response and kinematic selection needs to be applied.

Samples of 250k events are generated with 25 different values of the couplings, in a grid from -2.0 to 2.0 in steps of 1.0 and then passed through the full CDF simulation and the complete WW selection described in Chapter 6 is performed. The generated sample size is chosen to ensure that the statistics are high enough to give $\approx$ 1% statistical errors after all cuts (assuming a raw WW selection efficiency of order 4%). The luminosity and NLO cross-section of each of the generated samples are shown in Figure 9.5. Note that the {0,0} point in these plots corresponds to the previously quoted Standard Model cross-section of 12.4 pb.

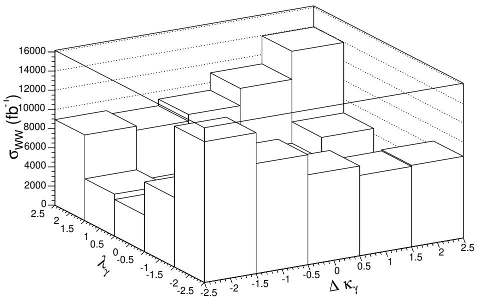

(a) NLO WW cross-section of HISZ anomalous coupling samples.

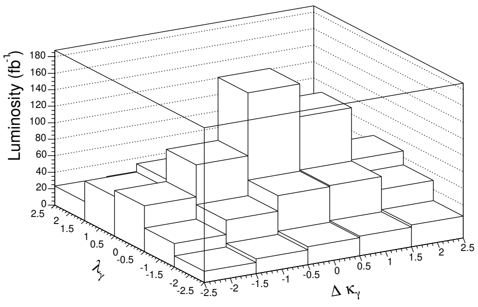

(b) Resulting luminosity of each HISZ sample

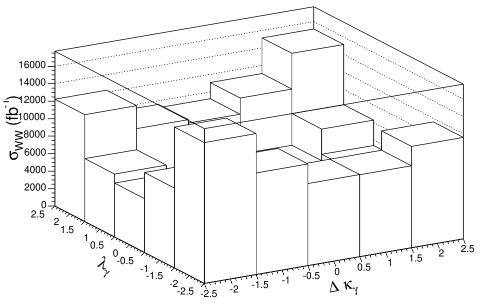

(c) NLO WW cross-section of EQUAL anomalous coupling samples.

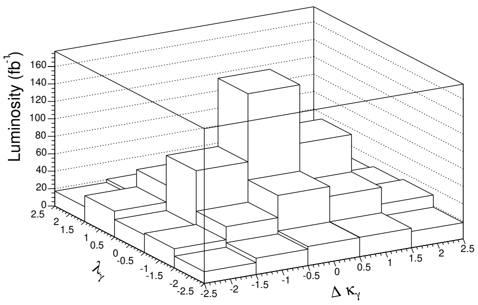

(d) Resulting luminosity of each EQUAL sample

Figure 9.5: Cross-section and luminosity of WW samples as a function of anomalous couplings $(\Delta\kappa, \lambda)$

After the event selection, the lepton-P_T distributions of the surviving WW events in each sample are collected together and passed into a likelihood calculation along with the lepton-P_T distributions of the expected background and the observed data candidates. These input distributions are shown in Figure 9.6 and are split into 5 bins with edges 20-40 GeV, 40-60 GeV, 60-100 GeV, 100-150 GeV and 150+ GeV.

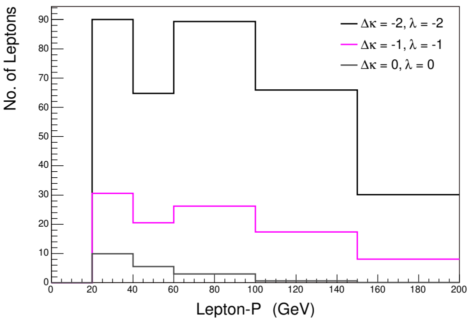

(a) Examples of lepton-P_T distributions in HISZ WW samples

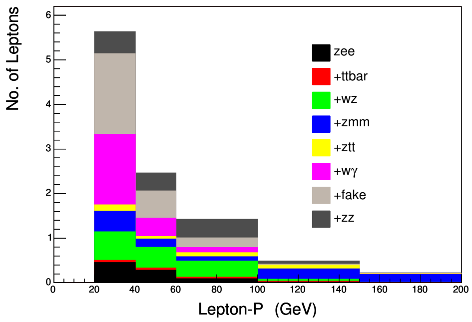

(b) Lepton-P_T of expected backgrounds

Figure 9.6: Input lepton-P_T distributions used in likelihood calculation. The data was shown previously in Figure 9.1(c)

The Likelihood Calculation

A two dimensional histogram of the expected number of signal events, as a function of $\{\Delta\kappa, \lambda\}$, is formed for each bin in the lepton-P_T distribution. The cross-section is known to have the form $\sigma_{WW}^{anom} = a_0 + a_1\lambda + a_2\Delta\kappa + a_3\lambda\Delta\kappa + a_4(\lambda)^2 + a_5(\Delta\kappa)^2$, where the a's represent cross-sections corresponding to unique event ensembles. Changing the anomalous couplings simple alters the WW kinematics by the relative weights of these sub-ensembles. Each ensemble will have its own unique selection efficiency which is independent of the value of the anomalous coupling. Hence the number of events in each bin of the lepton-P_T distribution can again be written in the form $N_{WW}^{anom} = a_0 + a_1\lambda + a_2\Delta\kappa + a_3\lambda\Delta\kappa + a_4(\lambda)^2 + a_5(\Delta\kappa)^2$. The a's are now interpreted as the unique efficiency times the unique cross-section for each ensemble multiplied by the total luminosity.

Figure 9.7 shows the WW expectation and the parabolic fit for the first and last lepton-P_T bin in the HISZ coupling samples. The fit parameters for both EQUAL and HISZ samples are listed in Table 9.3. All fits have a χ^2 less than 0.15.

HISZ Couplings						
	a_0	a_1	a_2	a_3	a_4	a_5
P_T Bin 1	9.8±1.7	-1.0±0.8	-0.14±1.0	3.8±0.7	2.8±0.7	12.7±0.76
P_T Bin 2	5.5±1.4	-1.1±0.71	0.13±0.85	2.4±0.64	2.8±0.56	9.1±0.64
P_T Bin 3	3.1±1.2	-1.5±0.80	-0.39±0.97	3.0±0.75	4.5±0.60	13.2±0.71
P_T Bin 4	0.75±0.70	-0.62±0.64	-0.08±0.85	1.7±0.65	3.1±0.47	11.1±0.60
P_T Bin 5	0.15±0.33	-0.19±0.41	-0.01±0.59	0.60±0.45	1.2±0.29	5.7±0.41
EQUAL Couplings						
	a_0	a_1	a_2	a_3	a_4	a_5
P_T Bin 1	9.60±1.8	-1.7±0.94	-0.091±1.1	1.3±0.81	5.7±0.74	12.6±0.80
P_T Bin 2	5.3±1.4	-1.4±0.85	-0.29±0.91	0.74±0.72	6.1±0.66	9.1±0.69
P_T Bin 3	3.4±1.4	-1.8±1.0	-0.62±1.1	0.67±0.86	10.0±0.75	13.2±0.78
P_T Bin 4	1.0±0.84	-1.6±0.86	-1.0±0.93	0.51±0.76	7.6±0.62	11.0±0.66
P_T Bin 5	0.28±0.45	-0.77±0.56	-0.74±0.64	0.18±0.51	3.1±0.40	5.6±0.45

Table 9.3: Values of the fit parameters to the anomalous WW expectations in all lepton P_T bins.

Using this signal expectation, the expected background and the observed data candidates, a Poisson probability is formed for each lepton-P_T bin thus:

$$P_i = \frac{e^{-\mu_i}\mu_i^{n_{data}}}{n_{data}!} \tag{9.4}$$

where n_{data} is the number of observed data candidates and the total expectation μ is given by $\mu = N_{WW} + N_{bkgd}$.

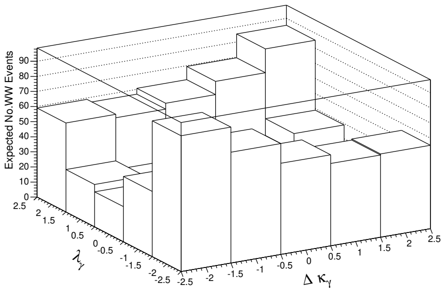

(a) WW expectation for Lepton-P_T of 20-40 GeV.

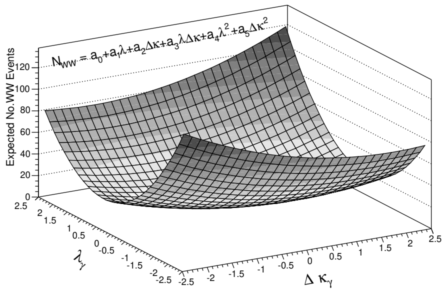

(b) Fitted WW expectation for Lepton-P_T of 20-40 GeV

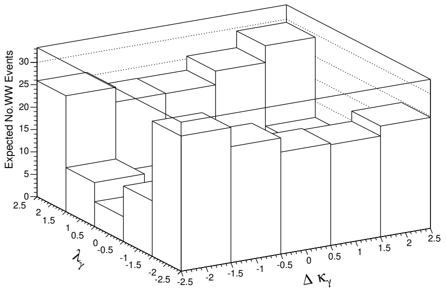

(c) WW expectation for Lepton-P_T of 150+ GeV.

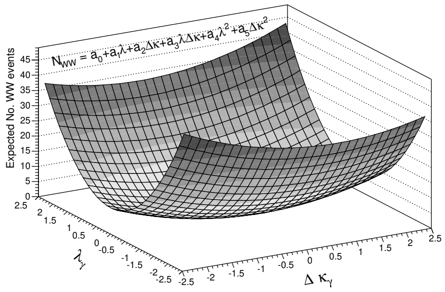

(d) Fitted WW expectation for Lepton-P_T of 150+ GeV

Figure 9.7: WW expectation as a function of HISZ anomalous couplings for first and last lepton P_T bins

Each of these probability surfaces is then combined into a single log-likelihood surface by taking the product over the P_T bins, as follows:

$$L = -log\left(\prod^{P_T\ bin\ i} P_i\right) \tag{9.5}$$

However, the expected number of events is a measured quantity with associated uncertainties (acceptance, luminosity etc). This likelihood must therefore include a Gaussian smearing around the central value of these quantities [61]. The final log-likelihood is then given by:

$$L = -log\left(\int_0^\infty \int_0^\infty \prod^{P_T\ bin\ i} P_i G(0,\sigma_b) G(0,\sigma_s)\ dn_b\ dn_s\right) \tag{9.6}$$

where the integration is over the systematic errors on the background expectation ($\sigma_{n_b} = 45\%$) and the signal expectation ($\sigma_{n_s} = 10\%$) which are assumed to be Gaussian distributed.

The integration is performed using a Monte Carlo technique. First note that the integral is essentially a Gaussian-weighted average Poisson probability. This average can then be calculated by sampling the Poisson probability multiple times, each time drawing the value of the expectation μ_j from a Gaussian distribution and then averaging these results to a single value of the likelihood. The Gaussian distribution has a mean equal to the central value of the expectation, μ and a σ equal the systematic error on the expectation, σ_μ.

The 95% C.L. on the value of the anomalous couplings consistent with the observed spectrum is given simply by the ellipse defined by $\Delta L = L_{min} - \frac{1}{2}s$ where s=5.99 for two free parameters(ellipse) at 95%C.L and 3.84 for one free parameter(on-axis limits) at 95%C.L [62].

The resulting 2D limits with both the HISZ and EQUAL coupling assumptions are shown in Figure 9.8 and the 1D, on-axis, values are:

$$-0.4 < \Delta\kappa < +0.6\ (\lambda = 0); \quad -0.3 < \lambda < +0.4\ (\Delta\kappa = 0)$$

for the EQUAL couplings and

$$-0.7 < \Delta\kappa < +0.9\ (\lambda = 0); \quad -0.4 < \lambda < +0.4\ (\Delta\kappa = 0)$$

for the HISZ couplings.

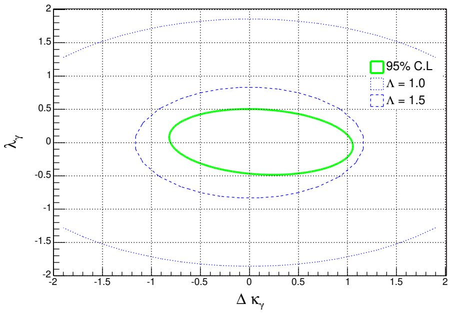

(a) HISZ 95%C.L. limits.

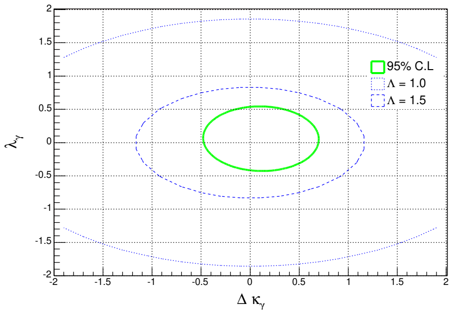

(b) EQUAL Limits

Figure 9.8: The 95%C.L. limits for HISZ and EQUAL anomalous coupling schemes. Also shown are the tree-level unitarity limits due to choice of Λ. Both limits were generated with $\Lambda = 1.0$TeV.

Chapter 10

Conclusions

This thesis has detailed a measurement of the cross-section of $p\bar{p} \rightarrow WW$ in the dilepton channel using data collected by CDF at the Tevatron collider operating at a centre of mass of 1.96 TeV. This cross-section measurement and the lepton P_T distributions have then been used to place constraints upon the possible value of anomalous trilinear gauge boson couplings in the $WW\ Z/\gamma$ vertex under the EQUAL and HISZ coupling schemes.

The measurement of the WW production cross-section allows a direct test of the non-Abelian structure of the Standard Model and its ability to accurately describe nature. The data shows excellent agreement with the Standard Model prediction of both the cross-section and kinematic distributions. No evidence for new physics in this channel is observed. The resulting cross-section measurement of $\sigma^{WW}_{meas} = 14.5^{+5.8}_{-5.1}(stat)^{+1.8}_{-3.0}(syst) \pm 0.9(lum)$ pb provides the expected significant improvement over the Run 1 CDF and DØ results. The measurement has been accepted for publication [63] in Physics Review Letters.

The recently published Run 2 DØ result, discussed in Section 2.3.2, offers the first 5σ observation and has both a better signal-to-noise ratio (or smaller systematic error) and a larger data sample of 220-250 pb^{-1}. The two results are however in excellent agreement with each other. A summary plot of these WW cross-section measurements at the Tevatron is shown in Figure 10.1.

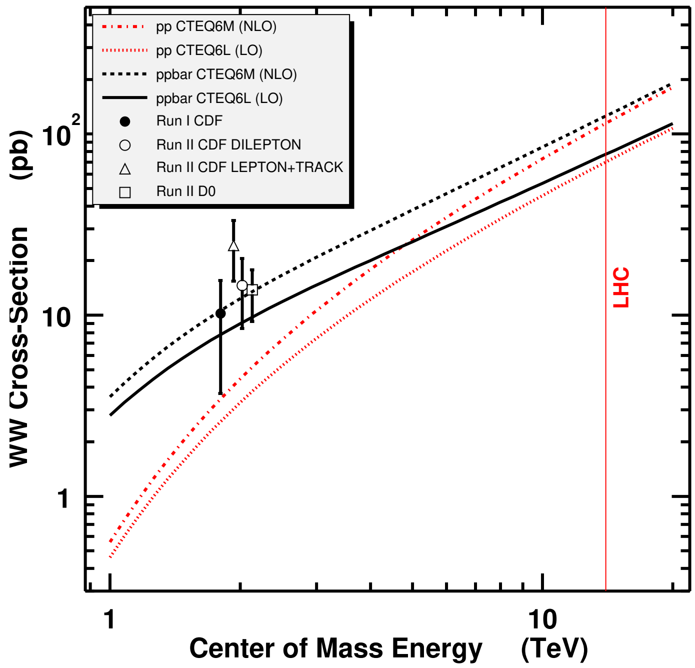

Figure 10.1: Summary of Tevatron WW cross-section measurements compared to theory.

This analysis and the DØ result have for the first time established a clear signal for W pair production at a hadron collider. The current knowledge of W pair production has also been extended by probing a different region of phase space with the higher centre-of-mass energy in Run 2. More importantly, by adding significantly more data ($\times 2$) the accuracy of the measurements has been greatly increased, as has their sensitivity to any new physics in the WW or $l\bar{\nu}\bar{l}\nu$ final state.

The anomalous coupling limits in both the EQUAL and HISZ schemes are again a significant improvement over the equivalent limits from Run 1, reducing the limits measured in $WW \rightarrow l\bar{\nu}\bar{l}\nu$ from $-1.1 < \Delta\kappa < 1.3$ to $-0.4 < \Delta\kappa < 0.6$ and from $-0.9 < \lambda < 0.9$ to $-0.3 < \lambda < 0.4$ for the 1D EQUAL couplings at the 95% C.L. However, a lack of statistics mean these limits still suffer in comparison to the combined LEP2 limits (see Section 2.3.4).

10.0.3 Future Work

As of May 1st 2005 the total Run 2 CDF dataset has expanded to over 500 pb^{-1}. It can be expected that both the cross-section and anomalous coupling results reported in this thesis will very soon be improved upon by the simple addition of new data. The anomalous coupling limits will be tightened still further by combinations with the other Run 2 measurements that probe the WWZ/γ vertex, such as the Wγ, Zγ and WZ channels and also WW production in the semi-leptonic decay channel. It is still expected therefore, that the final Run 2 limits will be competitive with the final LEP2 limits.

Appendix A

Event displays

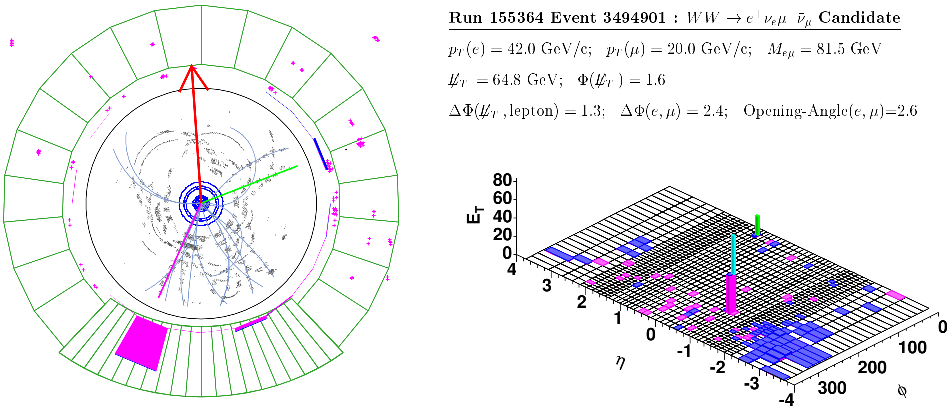

Figure A.1: r-ϕ and lego views of the $WW\to e\mu$ candidate: Run, Event = 155364, 3494901.

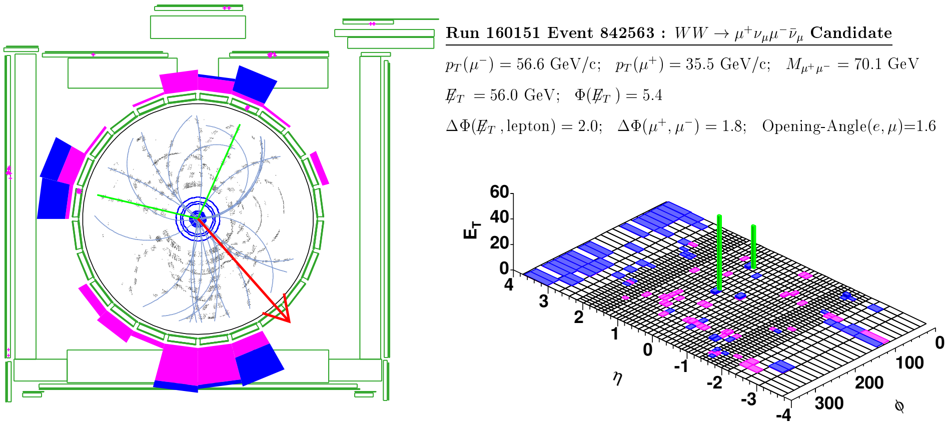

Figure A.2: r-ϕ and lego views of the $WW \to \mu\mu$ candidate: Run, Event = $160151, 842563$.

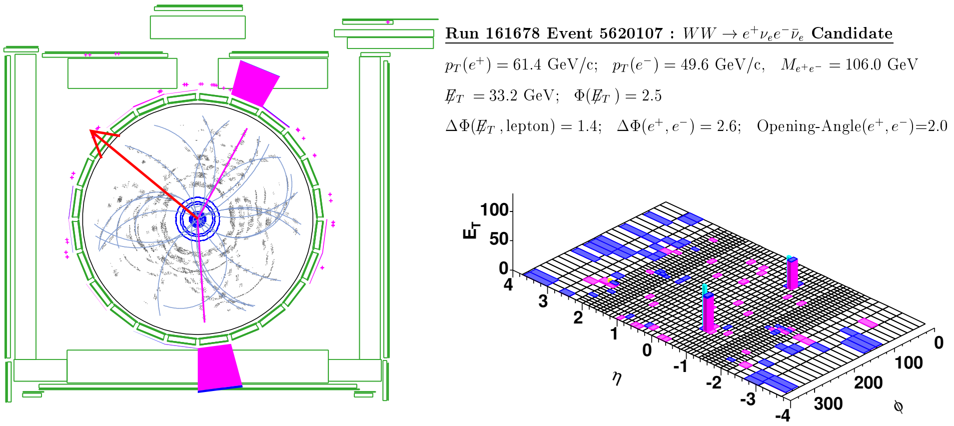

Figure A.3: r-ϕ and lego views of the $WW \to ee$ candidate: Run, Event = $161678, 5620107$.

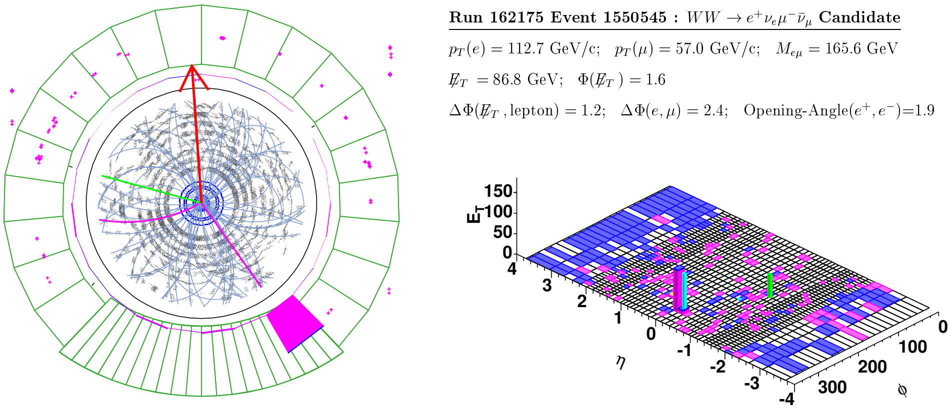

Figure A.4: r-ϕ and lego views of the $WW \to e\mu$ candidate: Run, Event = 162175, 1550545.

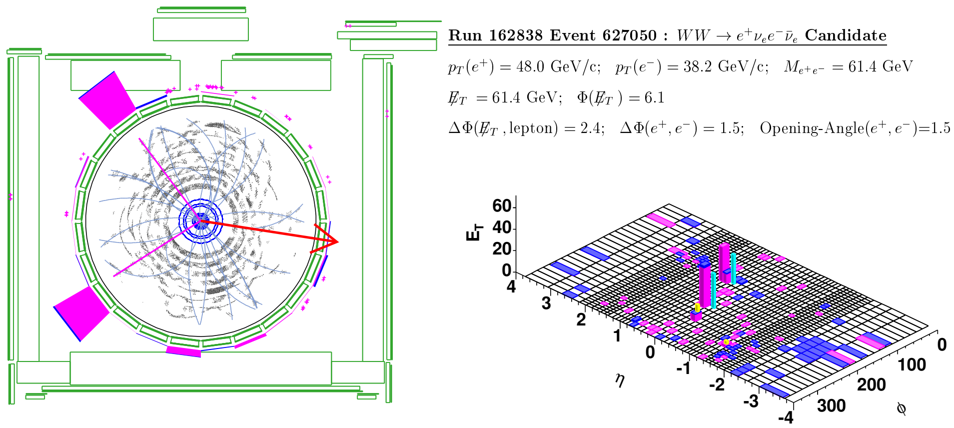

Figure A.5: r-ϕ and lego views of the $WW \to ee$ candidate: Run, Event = 162838, 627050.

Appendix B

Glossary

BMU	(component) Barrel Muon Detector
CCR	(component) Central crack gas chamber
CDF	(jargon) Collider Detector at Fermilab
CEM	(component) Central E-M calorimeter
CES	(component) Central E-M strip/wire gas chamber
CHA	(component) Central hadron calorimeter
CLC	(component) Cerenkov Luminosity Counters
CMP	(component) Central muon wall chamber upgrade
CMU	(component) Central muon chamber ADCs and TDCs
CMX	(component) Central muon wall chamber extension
COT	(component) Central Open-cell Tracking chamber wires
CPR	(component) Central pre-radiator gas chamber
CSP	(component) Central muon wall scintillator upgrade
CSX	(component) Central muon wall scintillator extension
PEM	(component) Plug E-M gas calorimeter pads
PES	(component) Plug E-M gas calorimeter strip wires
PHA	(component) Plug hadron gas calorimeter pads
PMT	(jargon) PhotoMultiplier Tube (a.k.a., phototube)
SVT	(component)Silicon Vertex Trigger finds displaced vertices in the SVX for the Level 2 trigger
SVX	(component) Silicon vertex chamber
WHA	(component) Endwall hadron calorimeter
XFT	(component)eXtremely Fast Tracker finds tracks in the COT for the Level 1 trigger

Bibliography

[1] Y. Ashie *et al.* [Super-Kamiokande Collaboration], “Evidence for an oscillatory signature in atmospheric neutrino oscillation,” Phys. Rev. Lett. **93** (2004) 101801 [arXiv:hep-ex/0404034]. 12

[2] S.L. Glashow, Nucl. Phys. **22**, 579 (1961); A. Salam in *Elementary Particle Theory*, ed. by N. Svartholm (Almqvist and Wiksells, Stockholm, 1968); S. Weinberg, Phys. Rev. Lett. **19**, 1264 (1967). 14

[3] K. Hagiwara, R. D. Peccei, D. Zeppenfeld and K. Hikasa,“Probing The Weak Boson Sector In $e^+e^- \to W^+W^-$,”Nucl. Phys. B **282**, 253 (1987). 19, 22

[4] K. Hagiwara, S. Ishihara, R. Szalapski, D. Zeppenfeld, ”Low energy effects of new interactions in the electroweak boson sector”, *Physical Review* **D48**, 2182 (1993) 22

[5] A. Djouadi, J. Kalinowski and M. Spira,“HDECAY: A program for Higgs boson decays in the standard model and its supersymmetric extension,” Comput. Phys. Commun. **108** (1998) 56 [arXiv:hep-ph/9704448]. 23

[6] T. Sjostrand et al., Comp. Phys. Commun. 135 (2001) 238 26, 58

[7] G. Corcella *et al.*,“HERWIG 6: An event generator for hadron emission reactions with interfering gluons (including supersymmetric processes),” JHEP **0101**, 010 (2001) [arXiv:hep-ph/0011363]. 26, 58

[8] J. M. Campbell *et al.*, “MCFM v3.4.3 Users Guide”, http mcfm.fnal.gov 26, 58

[9] R. K. Ellis, D. A. Ross and A. E. Terrano, Nucl. Phys. B 178, 421 (1981).

[10] H. L. Lai et al., Eur. Phys. J. **C12** (2000) 375. 27

[11] U. Baur and D. Zeppenfeld,“Unitarity Constraints On The Electroweak Three Vector Boson Vertices,” Phys. Lett. B **201**, 383 (1988). 29

[12] H. Aihara *et al.*,“Anomalous gauge boson interactions,” arXiv:hep-ph/9503425. 29

[13] DØ Collaboration, ”Limits on $WW\gamma$ and WWZ Couplings from W Boson Pair Production.”, Phys. Rev D58, Rapid Communications 051101 (1998), FERMILAB PUB-98-076-E, hep-ex/9803004. 30

[14] DØ Collaboration, ”Limits on Anomalous WWγ Couplings from $\mathrm{p\bar{p}} \rightarrow \mathrm{W}\gamma + \mathrm{X}$ Events at $\sqrt{s} = 1.8$ TeV”, Phys. Rev. Lett. 78, 3634 (1997) (hep-ex/9612002) 30

[15] DØ Collaboration, V. M. Abazov et al., hep-ex/0410066 (submitted to Phys. Rev. Lett). 31

[16] F. Abe *et al.*, The CDF Collaboration, ”Evidence of W^+W^- Production in $p\bar{p}$ Collisions at $\sqrt{s} = 1.8$ TeV”, Phys. Rev. Lett. 78, 4537 (1997). 31

[17] F. Abe *et al.*, The CDF Collaboration, "Measurement of $W-\gamma$ couplings in $p\bar{p}$ collisions at $\sqrt{s}=1.8$ TeV", Phys. Rev. Lett. 74, 1936 (1995). 31

[18] LEP Collaborations,"A combination of preliminary electroweak measurements and constraints on the standard model," arXiv:hep-ex/0412015. 31

[19] J. Konigsberg, S. Klimenko, S.M. Wang, D. Tsybychev, A. Sukhanov, S. Pronko, V. Necula, D. Acosta, G. Mitselmakher, A. Korytov, G. Lungu, "A first look at the CLC Luminosity Measurements", CDF-6052. 37, 57

[20] R. Blair *et al.* [CDF-II Collaboration],"The CDF-II detector: Technical design report," FERMILAB-PUB-96-390-E. 39

[21] J.P. Fernndez, "The CDF silicon detector for Run II", Nucl. Inst. & Meth. A 535 (2004), 370-373. 42

[22] T. Affolder *et al.*, "CDF Central Outer Tracker", Nucl. Inst. & Meth. A 526 (2004), 249-299. 43

[23] L. Balka *et al.*, "The CDF central electromagnetic calorimeter", Nucl. Instr. & Meth. A 267 (1988) 272. 46, 47

[24] M. Albrow *et al.*, "The CDF plug upgrade electromagnetic calorimeter: test beam results", Nucl. Instr & Meth. A 480 (2002) 524. 46, 47

[25] L. Balka, *et al.*, "The CDF central and endwall hadron calorimeter", Nucl. Instr. & Meth. A 267,(1988) 301. 46

[26] A. Artikov *et al.*, "Design and construction of new central and forward muon counters for CDF II", Nucl. Inst. & Meth. A 538, (2005), 358-371. 48

[27] G. Brandenburg, T. Liss, P. Schlabach *et al.*, "The CDF Run 1 Muon System Upgrade", CDF-6362 49

[28] Y.-K. Kim, J. Nielsen, L. Tompkins, G. Veramendi, "Trigger Efficiencies for High-E_T Electrons", CDF-6234. 55, 94, 105

[29] V. Martin, L. Cerrito, "Muon Cuts and Efficiencies for 4.11 Analyses", CDF-6825. 56, 57, 73, 94, 104, 105

[30] M. Lancaster D. Waters, "A Monte Carlo Program for W Production with Electroweak Radiative Corrections", CDF-5240 59

[31] "GEANT Detector Description And Simulation Tool", CERN Program Library Writeup W5014 (1994) 59

[32] Chris Hays, Peter Tamburello, Ashutosh Kotwal, Peter Wittich, Rick Snider "The COT Pattern Recognition Algorithm and Offline Code" CDF-6992. 61

[33] Tim Nelson, Rick Snider, David Stuart "Forward Electron Tracking with the PhoenixMods Package" CDF-6278. 63

[34] Robert G. Wagner "Electron Identification for Run II: Algorithms" CDF-5456. 65

[35] J. Thom, D. Glenzinski, M. Herndon, C. -J. Lin, A. Yagi, "Determination of the Run II COT Tracking Efficiency using the W-No-Track Sample", CDF-6866 62

[36] Larry Nodulman, "Curvature Corrections for 5.3.1", CDF-6971 62

[37] D. Glenzinski,P. Merkel,J. Thom,A. Yagil, C. Hill,J. Incandela,C. Mills, N. Lockyer,P. Wittich, P. Savard,R. Tafirout, "Addition of PHX Electrons to the Dilepton Analysis using the Tight Lepton and Isolated Track Sample", CDF-6787 63

[38] K. Yasuoka *et al*, Nuclear Instruments and Methods, A267 (1984), 315. 66

[39] D. Acosta *et al.* [CDF II Collaboration],"First measurements of inclusive W and Z cross sections from Run II of the Tevatron collider," Phys. Rev. Lett. **94** (2005) 091803 [arXiv:hep-ex/0406078]. 67

[40] Florencia Canelli, Anwar Bhatti, "Generic Jet Corrections for Run II", CDF-7358. 103

[41] M. Coca *et al.*, "Central Electron Identification Efficiencies for Summer 2003 Conferences", CDF-6580. 69, 94, 104

[42] Susana Cabrera *et al.*, "Measurement of ZZ+WZ cross-section using Run II data" CDF-6920 70

[43] C. Issever *et al.*, "Plug Electron Baseline Cuts and Efficiencies for Summer 2003", CDF-6789. 71, 94

[44] G. C. Blazey *et al.*,"Run II jet physics," arXiv:hep-ex/0005012. 73

[45] E. Halkiadakis, C. Hays, M. Tecchio and W. Yao, "A Conversion Removal Algorithm for the 2003 Winter Coferences", CDF-6250. 69

[46] A. Ivanov, E. Halkiadakis, A. Hocker, P. Tipton, "A study of $\not\!\!E_T$ Resolution in the $Z \to \mu\mu$ sample", CDF-6462 76, 83

[47] J. M. Campbell and R. K. Ellis, Phys. Rev. D 60 (1999) 113006; next-to-leading-order calculation using MCFM version 3.4.5. 92

[48] G. Chiarelli, R. Dell, I. Fedorko, S. Leone, A. Sidoti, “Measurement of the $\sigma(p\bar{p} \to W) \times BF(W \to e\nu)$ in the Plug Region Using Combined Calorimetric and Forward Tracking Information”, CDF-6535. 94, 95, 97

[49] M. Tecchio, “Adding CMIO muons to the top dilepton cross-section measurement”, CDF-6517. 94

[50] W. K. Sakumoto and A. Hocker, “Event $|Z_{vtx}| \leq 60$ cm Cut Efficiency for Run II”, CDF-6331. 94, 99

[51] M. L. Mangano, M. Moretti, F. Piccinini, R. Pittau and A. D. Polosa, “ALPGEN, a generator for hard multiparton processes in hadronic collisions”, JHEP **0307** (2003) 001 [arXiv:hep-ph/0206293]. 58

[52] Giulia Manca, Young-Kee Kim, ”$Z \to e^+e^-$ Cross-Section Measurement with Run II Data”, CDF-6202. 123

[53] Susana Cabrera *et al.*, “WW Production Cross-Section in the Dilepton Channel at CDF in Run II”, CDF-6323 100, 124

[54] D. Benjamin, A. Goshaw, M. Kirby, B. Heinemann, H. Hayward, N. Tanimoto, ”Measurement of the $W\gamma$ and $Z\gamma$ Production Cross Sections using 200/pb of Run 2 Data”, CDF-6601 128

[55] J.M. Campbell, R.K. Ellis, “An update on vector boson pair production at hadron colliders”, hep-ph/9905386. 130

[56] S. Frixione and B. R. Webber, “Matching NLO QCD Computations and Parton Shower Simulations”, hep-ph/0204244. 58

[57] D. Stump *et al.*, " Inclusive Jet Production, Parton Distributions, and the Search for New Physics", hep-ph/0303013. M. Blackston *et al*, "PDF studies using LHAPDF and the Hessian Method", CDF-6630 102

[58] S. Eidelman *et al.*, Phys. Lett. B **592**, 1 (2004). 93, 139

[59] G. J. Feldman and R. D. Cousins, "A Unified Approach to the Classical Statistical Analysis of Small Signals", Phys. Rev. **D57**(1998)3873-3889. 139

[60] U. Baur, T. Han, and J. Ohnemus, "QCD corrections and nonstandard three vector boson couplings in W+W- production at hadron colliders", Phys. Rev. **D53**, 1098 (1996). 141

[61] John Conway, "Calculation of Cross Section Upper Limits Combining Channels Incorporating Correlated and Uncorrelated Systematic Uncertainties", CDF-6428. 148

[62] S. Eidelman *et al.*, Phys. Lett. B **592**, 1 (2004) 148

[63] D. Acosta *et al.* CDF Collaboration, "Measurement of the W^+W^- production cross section in $p\bar{p}$ collisions at $\sqrt{s} = 1.96$ TeV using dilepton events". arXiv:hep-ex/0501050. 150